Tree root anchorage : modelling and numerical analyses of key contributing factors of wind firmness of Pinus pinaster

Ming Yang

THÈSE PRÉSENTÉE

POUR OBTENIR LE GRADE DE

DOCTEUR DE

L'UNIVERSITÉ DE BORDEAUX

École doctorale n° 304 : Sciences et Environnements

Spécialité : Physique de l'environnement

Par YANG Ming

Ancrage racinaire des arbres : modélisation et analyses numériques des facteurs clés de la résistance au vent du Pinus pinaster

Sous la direction de Mme DÉFOSSEZ Pauline (UMR ISPA INRA)
co-directeur : M. FOURCAUD Thierry (UMR AMAP CIRAD)

Soutenue le 16 décembre 2014

Membres du jury :

M. MOREL Stéphane	Professeur, Université de Bordeaux	Président
M. ACHIM Alexis	Professeur, Université Laval	Rapporteur
M. DELENNE Jean-Yves	Directeur de recherche, UMR IATE INRA	Rapporteur
M. BOURRIER Franck	Chargé de recherche, UR EMGR IRSTEA	Examinateur
Mme KOLB Évelyne	Maître de conférences, ESPCI	Examinatrice

UMR 1391 ISPA
INRA - Centre Bordeaux Aquitaine, France

Remerciements

Ce mémoire présente le travail réalisé pendant mes trois années de doctorat au sein du laboratoire UMR ISPA INRA (ancienne UR ÉPHYSE INRA) sous la direction de Pauline Défossez et Thierry Fourcaud. Je tiens tout d'abord à remercier sincèrement mes directeurs de thèse pour m'avoir offert ce sujet de thèse intéressant et m'avoir bien initiée et guidée dans un domaine qui me paraissait tout nouveau au début.

Je remercie les membres du jury : Alexis Achim et Jean-Yves Delenne pour avoir accepté de juger ce travail en tant que rapporteurs, Stéphane Morel pour avoir présidé le jury et pour ses suggestions enrichissantes, et Franck Bourrier et Évelyne Kolb pour leurs questions et discussions intéressantes.

Un travail de thèse ne se réalise jamais tout seul. Je souhaite exprimer toute ma gratitude à l'ensemble des personnes qui ont participé au bon déroulement de ma thèse :

— Je tiens à remercier Frédéric Danjon, avec lequel j'ai travaillé notamment sur l'aspect de l'architecture des systèmes racinaires du Pin maritime. Merci de m'avoir guidée avec patience dans le monde des racines et pour les données détaillées des systèmes racinaires qui ont tellement enrichi mon modèle.

— Je suis très reconnaissante à Jean-Marc Bonnefond de m'avoir fait comprendre ce qui s'est passé pendant les essais de treuillage sur le terrain en lien direct avec mon travail de modélisation ; à Didier Garrigou de m'avoir donné l'idée sur d'autres outils intéressants pour visualiser un arbre ; et à Pierre Trichet et toutes les autres équipes à Pierroton pour leur participation aux mesures des systèmes racinaires et des sols.

— Je remercie également Sébastien Griffon et Hervé Rey du laboratoire UMR AMAP CIRAD pour m'avoir formée à utiliser l'Xplo et le DigR.

— J'adresse mes vifs remerciements à Sylvain Dupont, Barry Gardiner, Frédéric Danjon et Yves Brunet pour leurs discussions et remarques précieuses apportées à mes présentations orales, à mes simulations et à ma rédaction.

— Merci également aux membres de mon comité de thèse, Stéphane Morel, Franck Bourrier et Alain Denis pour leurs suivi et conseils pendant toutes les étapes de ma thèse.

— Un grand merci à l'équipe informatique du labo, Mark Irvine pour la bonne gestion de l'Abaqus sur le serveur ainsi que ses réponses rapides aux problèmes concernant les calculs en parallèle ; Guy Pracros, Tovo Rabemanantsoa et Éric Pastor pour leurs appuis permanents de mon poste de travail.
— Je voudrais remercier Anne-Marie Bouchon, documentaliste du labo, et Barry Gardiner pour leur lecture attentive du manuscrit et les références utiles qu'ils m'ont trouvées.
— Je remercie le secrétariat du labo, Françoise Prud'homme, Valérie Savornin et Patricia Braconnier pour m'avoir aidée dans les démarches administratives et pour leur bonne humeur. Un merci particulier à Françoise Prud'homme pour la bonne gestion de mon dossier et son organisation efficace de mes voyages de conférences.
— Je remercie tous ceux que j'ai côtoyés et qui ont partagé ensemble la vie au labo (y compris certains déjà cités ci-dessus bien sûr), au bureau, dans la cafète, à la cantine, pour la bonne ambiance qu'ils ont créée et éventuellement de l'aide qu'il m'ont apportée : David, Jiangxin, Virginie, Shu, Kana, Cécile, Sébastien, Julien, Christopher, Amen, Clément, Delphine, Ferenc, Laurence, Louis-Étienne, Sandra, Alain, Sylvia, Christophe, ... la liste est tellement longue que je n'arrive pas à tous les citer...
— Je remercie l'INRA et la région d'Aquitaine pour avoir financé ce projet de thèse, et je remercie les directeurs successifs du laboratoire ISPA (ex ÉPHYSE) au cours de ces trois ans, Denis Loustau, Sylvain Dupont et Laurence Denaix, pour leur accueil convivial.

Pour finir, je remercie particulièrement ma famille pour leur soutien et leur écoute. Merci de toujours être là.

Résumé

Les tempêtes hivernales causent des pertes en bois qui s'élèvent à 50% du volume des dégâts dans les forêts européennes. Les phénomènes de déracinement des arbres (chablis) sont les plus fréquents or ils sont encore mal compris. Cette thèse vise à mieux comprendre le processus de déracinement de l'arbre et à identifier les traits structuraux et matériels (racines, sol) ayant un effet du premier ordre sur l'ancrage racinaire dans le cas du *Pinus pinaster*. Un modèle d'éléments finis a été développé et permis de simuler et suivre la chronologie des ruptures successives au cours du déracinement. Un seuil de rupture globale de l'ancrage est ainsi défini comme une résultante de l'architecture et de la résistance des matériaux en jeu (racines, sol). Cela devrait permettre à terme d'améliorer les modèles de risque au vent qui actuellement n'incluent pas de relation mécaniste pour le chablis. Dans la même logique, nous nous sommes appuyés sur les données expérimentales pour construire une architecture simplifiée du système racinaire du *P. pinaster*. L'importance des différentes composantes sur le mécanisme d'ancrage a été étudiée et le rôle essentiel joué par le pivot et les racines traçantes montré. Ce résultat confirme de nombreuses études expérimentales et théoriques et pour la première fois permet de quantifier ces effets. Le nombre de paramètres pertinents pourra ainsi être réduit pour exprimer l'ancrage. Cela ouvre des perspectives intéressantes pour simplifier l'utilisation du modèle pour l'appliquer à d'autres espèces, d'autres conditions de sol et différentes pratiques sylvicoles.

Mots clés : Stabilité de l'arbre, endommagement des racines, méthode des éléments finis, architecture racinaire, composantes de l'ancrage racinaire, *Pinus pinaster*

Abstract

Winter storms cause 50% of wood damage by volume to European forests. Tree uprooting is the most frequent phenomenon during storms ; however the mechanism is not well understood. This thesis aims to better understand the tree uprooting process and to identify both root structural features and material properties which have first-order effects on tree anchorage strength for the case of *Pinus pinaster*. A Finite Element Model has been developed and allowed simulating and tracking the sequential root breakage during the course of tree overturning. An overall tree anchorage strength is thus defined as the resultant of contribution of root system architecture and material strength (roots, soil). This would allow improving the risk models which currently don't include any mechanistic relationships to describe tree uprooting. In the same spirit, we have relied on root architectural data to build a simplified root system pattern with features of *P. pinaster*. Importance of different root components has been studied and the essential role of the taproot and shallow roots demonstrated. This result has confirmed numerous experimental and theoretical studies and for the first time quantified these impacts. Therefore the number of relevant parameters can be reduced to express overall root anchorage. This opens new prospects to simplify the model in order to apply to other species under other soil conditions and considering different silvicultural practices.

Keywords : Tree stability, sequential root breakage, finite element method, root system architecture, root anchorage components, *Pinus pinaster*

Title : tree root anchorage: modelling and numerical analyses of key contributing factors of wind firmness of *Pinus pinaster*

Table des matières

Introduction

0.1 Contexte et Problématique de la thèse

Les dégâts occasionnés par les tempêtes hivernales dans les forêts européennes sont considérables. A titre d'exemple, les tempêtes Martin et Lothar de décembre 1999 ont dévasté l'Europe de l'Ouest, la France étant la plus touchée en termes de dégâts forestiers. En tant que région côtière sud-ouest du pays, l'Aquitaine a connu des dégâts majeurs estimés à 27,7 millions de m^3 de volume de chablis (source : Ministère de l'agriculture et de la forêt). De plus, 10 ans après, la tempête Klaus a causé une perte totale de 40,7 millions de m^3 de bois en Aquitaine, volume bien supérieur à celui des tempêtes précédentes, soit 23% du volume total sur pied (source : IFN). Le Pin maritime (*Pinus pinaster*), l'essence principale dans la forêt de production de la région Aquitaine, a été essentiellement affecté avec un volume de dégâts de 37,9 millions de m^3 (source : IFN), soit 32% du volume sur pied (source : IFN). En outre, des bases de données sur des perturbations forestières en Europe (« The Database on Forest Disturbances in Europe » ; Schelhaas et al. (2003)) montrent que les dégâts liés aux tempêtes dans les forêts européennes ont tendance à augmenter depuis 1950 (Gardiner et al., 2010; Schelhaas et al., 2007).

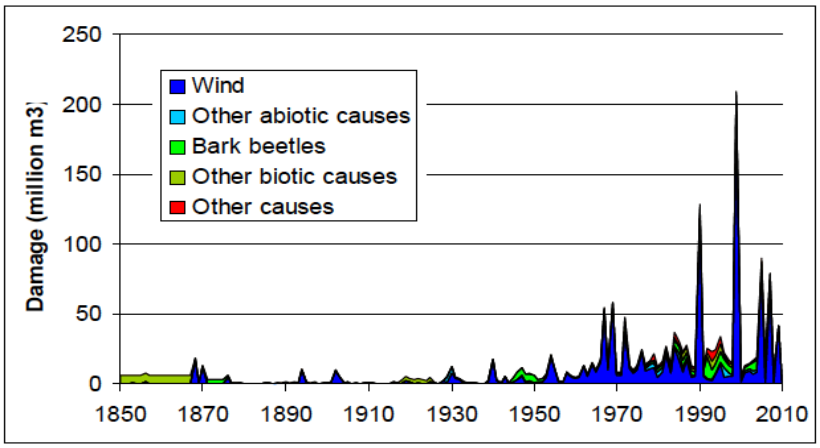

FIGURE 1 Dégâts dans les forêts européennes en fonction des causes depuis 1850 (Gardiner et al., 2010)

Parmi tous les dommages en forêt, celui lié aux tempêtes est bien supérieur aux autres causes biotiques ou abiotiques (Figure 1). Les phénomènes de déracinement des arbres, chablis, sont en général plus fréquents que les ruptures au niveau du tronc, volis (Gardiner et al., 2010). Par exemple, en Région Aquitaine le chablis représentait 69% de la totalité du volume perdu lors de la tempête Klaus (source : IFN). Ce type de dégât est d'autant plus fréquent que l'arbre est de grande dimension et le sol saturé. La sensibilité des arbres au volis ou au chablis en fonction de leur stade de développement a été étudiée de façon théorique par Ancelin et al. (2004). Les arbres de faible dimension (< 20 *cm* de diamètre à hauteur de poitrine pour *P. pinaster*) ne sont pas endommagés par chablis mais par une inclinaison du tronc qui peut être qualifiée de "verse" (toppling en anglais) si l'angle d'inclinaison dépasse 15° (Mason, 1985).

L'importance et la localisation des dégâts, ainsi que la vulnérabilité des forêts au vent, sont le résultat d'interactions complexes entre les conditions météorologiques, la composition des massifs forestiers, la gestion sylvicole du peuplement forestier, le type de sol et son état physique lors du passage de la tempête. Or, jusqu'à présent, la compréhension de ces mécanismes reste partielle (Figure 2). La plupart des études sur la stabilité des arbres au vent ont porté depuis plusieurs décennies (Telewski and Jaffe, 1986) sur l'interaction entre les parties aériennes des arbres et le vent, et aux échelles de l'individu et du peuplement (Blennow and Sallnäs, 2004; Cucchi et al., 2004; Dupont and Brunet, 2008; Fournier, 1993; Gardiner et al., 2000; James et al., 2006; Moore, 2000; Moore and Maguire, 2004; Peltola et al., 1999; Pivato et al., 2014; Rodriguez et al., 2008; Sellier et al., 2006).

Parmi ces travaux, on trouve des modèles de prévision des dommages en forêt en fonction des caractéristiques du vent et du peuplement forestier : HWIND, GALES et FOREOLE (Ancelin et al., 2004; Gardiner et al., 2000, 2008; Peltola et al., 1999). Ces modèles distinguent des dégâts par rupture du tronc ou déracinement. Ils reposent sur des concepts de mécanique classique : mécanique des solides et des structures pour décrire les déformations de l'arbre et mécanique des fluides pour décrire les contraintes exercées par le vent. Ces modèles permettent de calculer le moment de flexion à la base du tronc dû à l'action du vent et au poids propre de la partie aérienne. Ce moment de flexion est alors comparé à la résistance maximum d'ancrage de l'arbre dans le sol pour estimer le risque de dommage pour chaque arbre. Une des limites de ces modèles est l'estimation empirique de l'ancrage racinaire des arbres (voir Chapitre 1). Parmi les modèles d'interaction vent-plantes, certains font appel à des techniques de calcul numérique, par exemple la méthode des éléments finis (FEM), qui permet d'aborder le problème dans toute sa complexité, en décrivant plus finement l'architecture des parties aériennes pour simuler leur dynamique en fonction du vent à l'échelle d'un individu (Fournier, 1993; Moore and Maguire, 2008; Sellier et al., 2006). Certains modèles prennent en compte de façon plus fine l'écoulement turbulent du vent et ses effets à l'échelle du couvert. C'est le cas des travaux de

Pivato et al. (2014). Cependant dans tous ces modèles, le comportement de la partie souterraine, le facteur déterminant de l'ancrage de l'arbre, est décrit soit par un encastrement parfait (Pivato et al., 2014; Sellier et al., 2006), soit par le biais de relations empiriques (Ancelin et al., 2004; Cucchi et al., 2004; Gardiner et al., 2000; Peltola et al., 1999). L'ancrage des arbres dans le sol reste encore mal décrit dans ces modèles d'interaction vent-plantes. Or pour améliorer cette description, la modélisation mécanique est indispensable. Elle permet d'intégrer les connaissances actuelles concernant l'architecture racinaire, la mécanique des structures et la résistance mécanique du bois de racine et du sol comme nous le verrons dans le Chapitre 1. Cette thèse reprend les premiers travaux en modélisation numérique de l'ancrage menés par T. Fourcaud et ses collaborateurs (Dupuy et al., 2005a,b, 2007; Fourcaud et al., 2008). L'accent a été mis sur l'articulation du modèle avec des données expérimentales, données déjà disponibles dans la littérature ou acquises par ailleurs au cours de la thèse. Le *P. pinaster* a été choisi comme espèce modèle car c'est une espèce pour laquelle de nombreuses données sur l'architecture racinaire sur podzol et les propriétés du bois sont disponibles (Bert and Danjon, 2006; Danjon et al., 1999a,b, 2005, 2013a,b; Khuder et al., 2007; Stokes et al., 1997a). C'est la première espèce sur laquelle une analyse architecturale quantitative du système racinaire a été effectuée. De plus, elle est particulièrement exposée au risque de chablis.

Les objectifs de cette thèse sont (i) d'améliorer le modèle initial de Dupuy et al. (2005b) en modélisant la rupture mécanique des racines ; (ii) de mieux comprendre les rôles de la structure du système racinaire (la structure est définie à un stade de développement donné par la topologie, i.e. le graphe des liens entre les différents axes racinaires, et la géométrie, i.e. les angles de ramification, les trajectoires des segments, les diamètres en section et les longueurs des racines) et des propriétés des matériaux du bois de racine et du sol via des expériences numériques. L'un des enjeux de la thèse est d'identifier les facteurs clés de l'ancrage des arbres dans le sol. Ces facteurs clés doivent à terme servir à évaluer l'ancrage d'un arbre en fonction de ses propriétés intrinsèques (morphologiques, mécaniques, biologiques, etc.) et des conditions environnementales (mécanique du sol, l'humidité du sol, l'hétérogénéité du sol, etc.).

Le mémoire se présente sous la forme de cinq chapitres. Il débute par une synthèse des connaissances actuelles sur la modélisation de l'ancrage des arbres dans le sol (Chapitre 1). Le chapitre suivant porte sur la modélisation du comportement mécanique des racines lors du déracinement de l'arbre et son impact sur l'ancrage racinaire (Chapitre 2). Les chapitres suivants analysent le rôle des trois composantes majeures de l'ancrage : la morphologie du système racinaire (Chapitre 3), la géométrie des racines (diamètre, longueur, défilement) et les propriétés des matériaux des racines et du sol (Chapitre 4). Enfin nous concluons en rappelant les résultats majeurs de cette thèse et les perspectives qu'ils ouvrent.

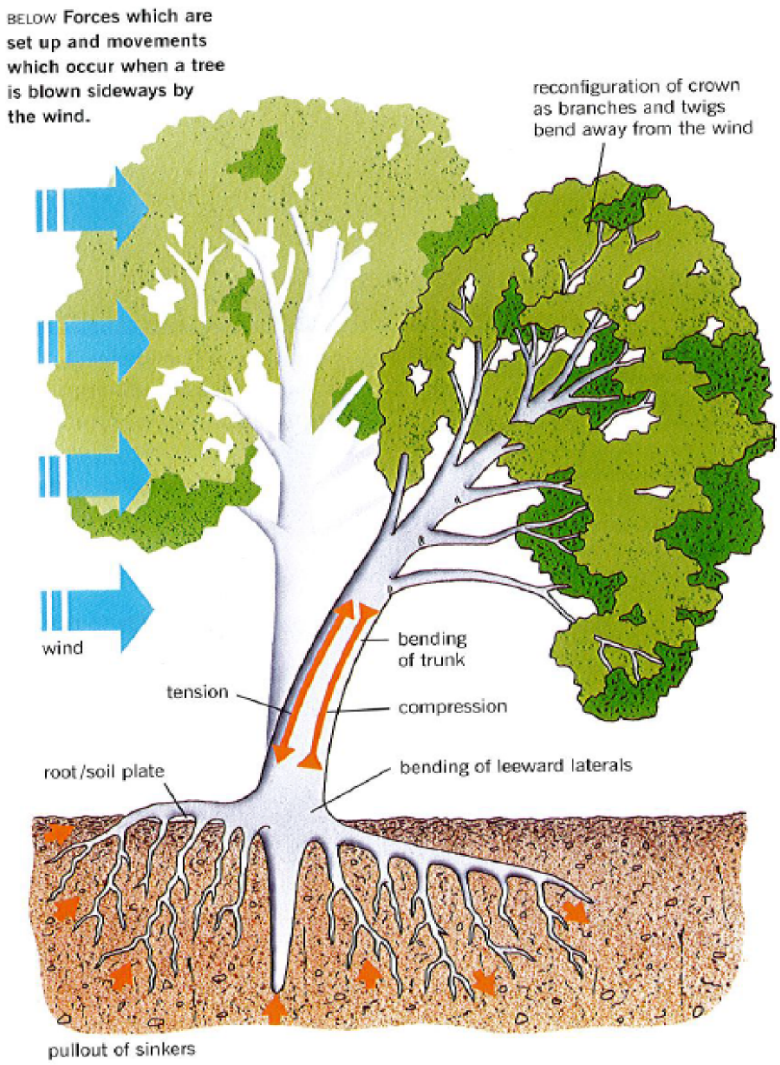

FIGURE 2 Schéma de synthèse décrivant les composantes à prendre en compte pour étudier la résistance d'un arbre au vent (Ennos, 2001). Le vent agit principalement au niveau du houppier de l'arbre dont la surface est très importante par rapport à celle du tronc. La partie aérienne de l'arbre est alors soumise à une flexion. Le moment dû à la force de traînée et celui dû au poids de la partie aérienne sont les deux moteurs du renversement. Hormis certains processus dissipatifs (frottement dans des branches et des feuilles, etc.), une grande partie des forces du vent est transmise à la partie souterraine via le tronc et la souche. Le tronc sert de bras de levier. Les racines sont alors mobilisées en tension, en flexion, en compression et en torsion tandis que le sol résiste en cisaillement.

Chapitre 1

Introduction à la modélisation de l'ancrage des arbres dans le sol

La stabilité mécanique d'un arbre résulte de la mise sous contrainte de structures complexes. La géométrie et l'agencement des branches (topologie) des parties aériennes et racinaires permettent à l'arbre d'optimiser la captation de la lumière et des ressources. Les axes ligneux assurent par ailleurs une fonction vitale de support mécanique. Ils assurent la résistance de l'arbre à son propre poids et aux sollicitations aérodynamiques liées aux vents (Fournier et al., 2013). L'ancrage des racines dans le sol est une des composantes de la stabilité mécanique de l'arbre avec la résistance du tronc au flambement ou à la flexion.

Nous allons voir dans ce chapitre que l'ancrage d'un arbre résulte de différentes composantes telles que l'architecture du système racinaire, la géométrie des racines, les propriétés du matériau bois qui constitue les racines structurales, et la résistance mécanique du sol environnant. Ce chapitre présente une synthèse des connaissances sur chacune de ces composantes et décrit les modèles existants pour comprendre et prévoir l'ancrage d'un arbre dans le sol. Nous nous focalisons ici sur la résistance à l'arrachement par le vent pour des arbres sensibles au chablis tels que *P. pinaster*.

1.1 Architecture du système racinaire, diversité et évolution

Les développements en biomécanique et architecture des plantes ont montré l'importance de l'influence de la géométrie de la plante sur sa résistance mécanique. Certains modèles d'interaction vent-plantes sont basés sur une description explicite de la structure de la partie aérienne (i.e. la typologie des axes, leurs liens topologiques, leurs dimensions, etc.) et ont montré que les effets liés à l'architecture sont prépondérants sur les effets liés à la résistance des

matériaux bois (Sellier and Fourcaud, 2009; Sellier et al., 2008). Il paraît donc indispensable de considérer l'architecture du système racinaire si l'on veut comprendre l'ancrage mécanique d'un arbre.

On distingue deux types de racines selon leurs rôles vis-à-vis de l'arbre : les racines structurales sont les grosses racines ligneuses dont le diamètre est supérieur à 1 cm chez les grands arbres et qui assurent le support mécanique. Les racines fines dont le diamètre est inférieur à quelques mm sont, elles, essentiellement responsables de l'acquisition de l'eau et des nutriments (Cairns et al., 1997; Hendrick and Pregitzer, 1993; Reubens et al., 2007; Smith et al., 2006). L'ensemble des racines structurales de l'arbre forme un système racinaire qui joue un rôle important dans l'ancrage de l'arbre. Les traits morphologiques de ce dernier sont gouvernés par des caractéristiques génétiques, mais sont aussi très fortement liés au milieu, ce qui donne une grande variation de l'architecture des systèmes racinaires entre espèces et au sein d'une même espèce (Fitter, 1994). Certains auteurs classent les morphologies des systèmes racinaires d'arbre principalement selon trois catégories (Figure 1.1) : le système racinaire en cœur, le système racinaire traçant, et le système racinaire pivotant (Busgen et al., 1929). La figure 1.1 (a) représente le système racinaire en cœur caractérisé par ses racines structurales émises par la souche dans toutes les directions. Les racines s'orientent donc de manière très homogène. La figure 1.1 (b) représente le système racinaire traçant caractérisé par de très grosses racines traçantes surfaciques portant des racines plongeantes peu profondes. La figure 1.1 (c) représente le système racinaire pivotant caractérisé par une longue racine épaisse verticale appelé le pivot primaire. Ce dernier est haubané par des racines traçantes surfaciques portant des pivots secondaires verticaux.

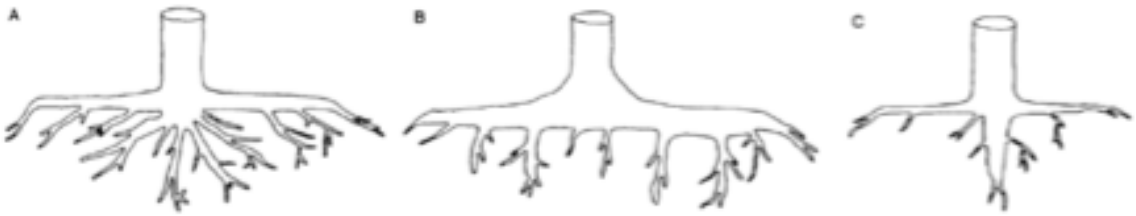

FIGURE 1.1 Trois principales catégories de systèmes racinaires (Kostler et al., 1968) : (a) système racinaire en cœur ; (b) système racinaire traçant ; (c) système racinaire pivotant.

Outre une diversité entre espèces, l'architecture d'un système racinaire évolue au cours de la croissance de l'arbre. C'est le cas du *P. pinaster* qui est de type pivotant. Des analyses quantitatives de l'architecture racinaire permettent de suivre son évolution suivant les différents stades de développement (Figure 1.2). Le système racinaire d'un jeune *P. pinaster* peut être assimilé à un pivot primaire haubané par un certain nombre de racines traçantes qui se développent dans les horizons de surface, celles situées sur les premiers 15 cm du pivot forment

alors de longues traçantes au stade mature (Burbidge, 1936). On peut aussi identifier une zone autour du pivot dans laquelle le défilement des racines traçantes est plus important, cette zone est appelée ZRT ("Zone of Rapid Taper" ; L5 dans la Figure 1.2). Dans les Landes de Gascogne, en landes mésophiles ou humides, la progression verticale du pivot principal du *P. pinaster* est stoppée en profondeur (nappe phréatique, couche d'alios). Les pivots secondaires émis dès l'âge de deux ans par les traçantes près de la souche s'épaississent alors et la part du pivot dans le système racinaire diminue. De plus, un renforcement en biomasse plus prononcé se concentre proche de la base des traçantes caractérisé par une forte croissance secondaire. Des racines profondes se développent du pivot primaire et des pivots secondaires à partir d'environ 75% de leur profondeur. A ce stade-là, la partie centrale du système racinaire située sous la ZRT est capable d'emprisonner une grande quantité de sol très compacté, et toutes ces racines avec le sol emprisonné forment une « cage rigide » (L19 dans la Figure 1.2). Ces caractérisques architecturales quantitatives peuvent être synthétisées par un schéma représentatif pour le *P. pinaster* (Figure 1.2).

La diversité et l'évolution des systèmes racinaires sont également liées à la plasticité génétique d'une espèce. La morphologie des systèmes racinaires est en effet très variable en raison de l'aptitude des arbres à s'adapter aux contraintes du milieu. Cette plasticité est particulièrement forte dans le cas des racines qui se développent dans un milieu très hétérogène dont les propriétés fluctuent au cours du temps. Les propriétés physiques, chimiques et la structure du sol évoluent sous l'effet des conditions climatiques (e.g. état hydrique du sol), de facteurs biologiques (e.g croissance des racines, activités des champignons, de la microfaune, des microorganismes, de la décomposition des matières organiques...) (Czarnes et al., 2000; Danjon et al., 2009; Read et al., 2003). Elles évoluent également sous l'action anthropique : par exemple, le tassement du sol par le passage des engins agricoles modifie la structure du sol et le développent des racines (Bengough et al., 2006; Bengough and Mullins, 1990; Passioura, 2002; Saffih-Hdadi et al., 2009). Ces variations de structure des sols (horizons indurés, nappe phréatique) ont un impact direct sur le développement des racines (Danjon et al., 2005; Fraser, 1962).

La croissance des racines dans ce milieu complexe est dynamique, fortement capable de s'adapter aux propriétés locales du sol et aux stimuli mécaniques externes, e.g. vent ou pente (Di Iorio et al., 2008; Stokes et al., 1997a, 1995; Tamasi et al., 2005). Ainsi, la profondeur d'enracinement, un élément très important de l'ancrage de l'arbre, est sensible aux états physique et hydrique du sol : le drainage du sol facilite le développement du pivot primaire en profondeur (Fraser, 1962). Le pivot primaire peut cesser de se développer en raison d'un horizon induré ou de la nappe phréatique et induire le développement d'une grande quantité de pivots secondaires proche du pivot primaire (Cucchi et al., 2004; Danjon et al., 2005).

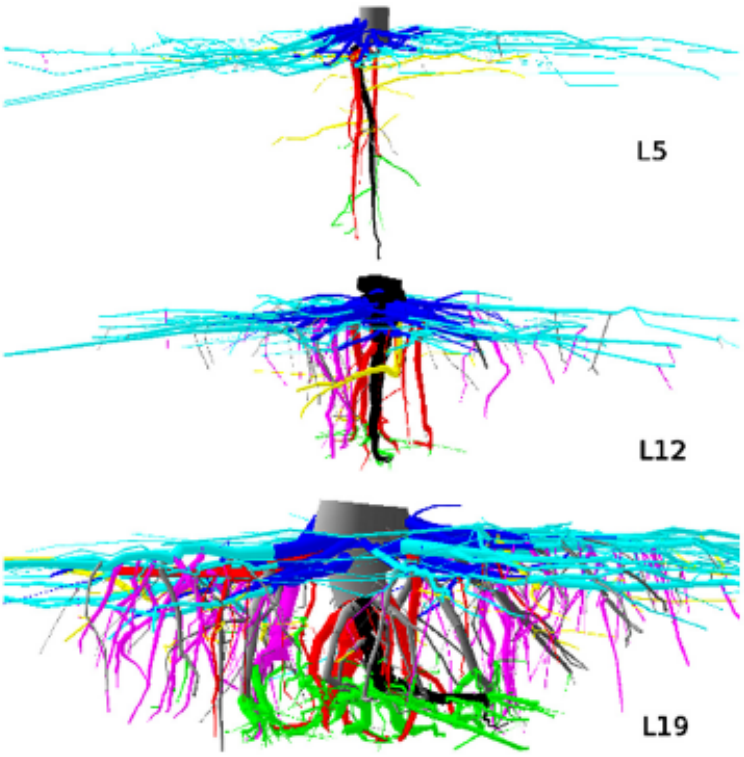

FIGURE 1.2 Systèmes racinaires de *P. pinaster* d'une même parcelle à 5, 12 et 19 ans ; correspondant respectivement à L5, L12 et L19. Les racines sont colorées en fonction de leur type : la souche en gris, le pivot en noir, la ZRT en bleu, les traçantes au delà de la ZRT en bleu ciel, les pivots secondaires sous la ZRT en rouge, les pivots au delà de la ZRT en magenta, les obliques en gris, les horizontales à profondeur intermédiaire en jaune et les racines profondes en vert (Danjon et al., 2013a)

L'acclimatation des racines se manifeste aussi par un renforcement en biomasse. Ainsi les arbres de lisière présentent dans le secteur au vent des racines de taille plus importante que ceux de l'intérieur de la parcelle, cela a été observé pour le *P. pinaster* par Cucchi et al. (2004). Ces modifications morphologiques induites par la plasticité et l'acclimatation des racines peuvent dans certains cas dominer les caractéristiques propres à l'espèce. A titre d'exemple, les racines traçantes du *P. pinaster* fourchent très peu spontanément. Or si elles ont été sectionnées lors d'une opération de travail du sol ou endommagées localement par une maladie, des fourches portant de nombreuses racines apparaissent (Danjon et al., 2009).

Dans ce paragraphe, nous avons montré la diversité et l'évolution de l'architecture des systèmes racinaires des arbres au cours de leur vie. Les connaissances que nous en avons sont encore limitées car les techniques de mesures sont relativement lourdes et coûteuses. Elles reposent en général sur des mesures manuelles avec boussole, inclinomètre, pied à coulisse ou

des mesures semi-automatiques avec numériseur 3D à champ magnétique basse fréquence, et les données résultantes peuvent être intégrées dans des logiciels de saisie et de représentation 3D d'architectures de plantes (de Coligny et al., 2004; Griffon and de Coligny, 2014; Sinoquet and Rivet, 1997; Sinoquet et al., 1997) (http://amapstudio.cirad.fr/). Les techniques semi-automatiques ont été développées pour étudier l'architecture des plantes et permettent des analyses architecturales quantitatives en trois dimensions des systèmes racinaires (Danjon et al., 2013a,b). Mais elles sont destructives et nécessitent une excavation et une numérisation du système racinaire. Ce sont cependant les seules utilisables actuellement. Les techniques géophysiques non destructives de type radar sol ont récemment progressé (Wu et al., 2014), mais elles seraient cantonnées dans des types de sol particuliers à fort contraste et aux grosses racines, car dans des peuplements forestiers il est difficile de distinguer les racines d'un arbre des racines des autres. Les mesures de type électrique sont encore au stade de développement, et elles ne donnent pas d'informations sur le système racinaire mais sur la surface en section du collet de la plante (Dietrich et al., 2013). Il n'y a que les mesures aux rayons X qui peuvent s'effectuer dans des pots (Mooney et al., 2012), ce qui pourrait dans notre cas être utilisé pour constater les déplacements et ruptures de racines durant un essai de treuillage. Les données d'architecture dont on dispose sont principalement pour le *P. pinaster*. La base de données du *P. pinaster* sur podzol landais est la seule base de données d'architecture 3D complète de systèmes racinaires du semis à l'arbre adulte et codée en axes et segments existante à ce jour. Les moyens expérimentaux permettent de déterminer les éléments clés de la résistance mécanique de l'ancrage, mais ne permettent pas d'identifier les types de contrainte ou d'endommagement qui s'exercent sur chaque élément de la structure au cours du temps. De plus, comme le système racinaire est caché et que la variabilité de sa structure est forte, l'échantillonnage doit être fait au hasard et la taille de l'échantillon est faible. Il n'est par exemple pas possible d'échantillonner a priori 10 systèmes racinaires avec un gros pivot ou 10 systèmes racinaires sans pivot. Face à ces limites expérimentales, nous verrons au cours de ce mémoire que la modélisation est une approche complémentaire permettant de faire des expériences sur des architectures virtuelles.

1.2 Mécanique des racines

La résistance mécanique d'une racine est déterminée par sa géométrie et la résistance du matériau bois qui la constitue. Sous l'effet du vent, les racines sont soumises à quatre sollicitations principales : la flexion, la tension, la compression et la torsion.

Dans les travaux sur l'ancrage racinaire, le comportement mécanique des racines, du fait de leur géométrie filiforme, est souvent décrit à l'aide de la théorie des poutres qui suppose

que la longueur est très grande par rapport aux dimensions transverses (Hibbitt et al., 2013; Timoshenko, 1940).

Dans ce mémoire, on a utilisé la poutre de type Timoshenko qui permet de prendre en compte le cisaillement des sections dans le cas d'une poutre en flexion (Hibbitt et al., 2013; Timoshenko, 1940).

Pour une poutre homogène parfaitement élastique et soumise à une force axiale (de traction ou de compression) P, la déformation axiale ε et la contrainte axiale σ sont gouvernées par la géométrie (l'aire) de la section droite de la poutre A et le module d'élasticité E. En tension et compression, la déformation longitudinale ε d'une poutre est donnée par la loi de Hooke :

$$\varepsilon = \frac{\sigma}{E} \tag{1.1}$$

Cette contrainte σ est donc constante en tout point de cette section. En particulier, dans un cas de section circulaire elle diminue proportionnellement à l'inverse du diamètre au carré $\frac{1}{d^2}$:

$$\sigma = \frac{P}{A} \tag{1.2}$$

Si la rupture du matériau peut être décrite par un comportement parfaitement fragile en introduisant les résistance en tension σ^t et en compression σ^c, la rupture en tension ou en compression survient alors lorsque la contrainte appliquée dans la section σ excède la limite en tension ou en compression.

Pour la sollicitation en flexion, les déformations et les contraintes dépendent des conditions d'encastrement de la poutre et d'application de la force. On considère ici le cas d'une poutre encastrée soumise à son extrémité libre à une force ponctuelle P perpendiculaire à la direction longitudinale initiale de la poutre x (Figure 1.3). Dans ce cas, la déformation de flexion de la poutre à l'extrémité libre δ est maximum et elle est donnée par la solution analytique :

$$\delta = \frac{Pl^3}{3EI_z} \tag{1.3}$$

où l est la longueur de la poutre et I_z le moment d'inertie de la section droite calculé par rapport à l'axe neutre. Toujours dans le cas d'une section droite circulaire, le moment d'inertie I_z est proportionnel au diamètre de la section d à la puissance 4, ce qui implique qu'à charge constante la déformation de flexion à l'extémité libre varie proportionnellement à l'inverse du diamètre à la puissance 4.

Dans une poutre en flexion pure, les contraintes ne sont pas homogènes et se répartissent de part et d'autre de l'axe neutre de la section : les contraintes de tension et de compression sont nulles sur l'axe neutre et maximales sur les bords de la poutre (Figure 1.4), et inversement

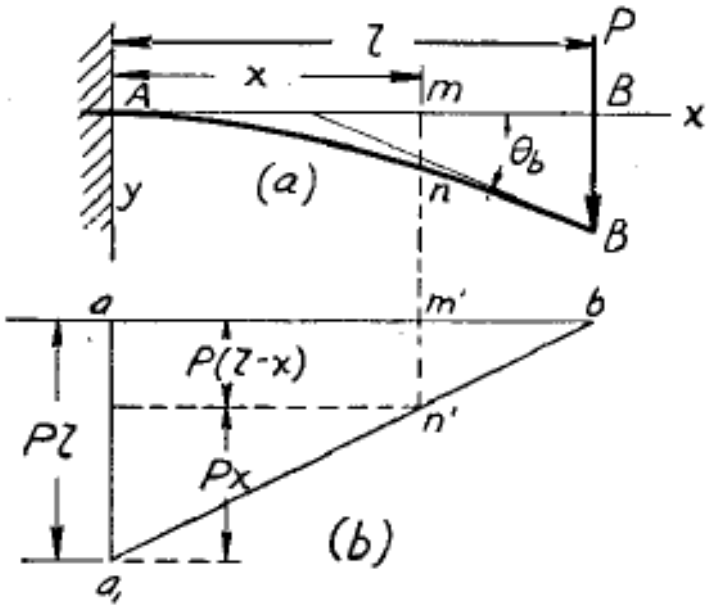

FIGURE 1.3 Poutre encastrée soumise à son extrémité libre à une force ponctuelle perpendiculaire à la direction axiale initiale : (a) vue dans le plan $X-Y$; (b) diagramme du moment de flexion suivant la direction X qui est la direction axiale initiale de la poutre (Timoshenko, 1940).

pour les contraintes de cisaillement. Dans le cas d'une poutre soumise à un moment de flexion pure M avec l'hypothèse de la section droite toujours plane et normale à la direction axiale (X), la contrainte sur un point à distance y de l'axe neutre de la section à la position axiale x est donnée par :

$$\sigma_x(y) = \frac{My}{I_z} \tag{1.4}$$

Ainsi la rupture en flexion d'un point dans une section survient lorsque localement la contrainte excède la limite en tension ou en compression et celle-ci dépend de la géométrie de la section via son moment d'inertie. Comme le moment est une puissance 4 de la longueur caractéristique de la section (le diamètre d pour une section circulaire), ces contraintes extrêmes diminuent fortement avec la section de la poutre. Dans les constructions, les sections des poutres sont ainsi optimisées pour réduire les contraintes qui s'exercent pour une même charge sur les éléments. Cette optimisation a été aussi observée pour les racines des arbres qui ont des capacités d'adaptation remarquables comme on l'a vu dans la section précédente. Ainsi les racines structurales situées dans la direction du vent peuvent présenter des sections droites proches de la souche en formes de « I » ou « T » (Figure 1.5) qui leur permettent de maximiser la résistance pour une même quantité de biomasse (Coutts et al., 1999; Nicoll and Ray, 1996).

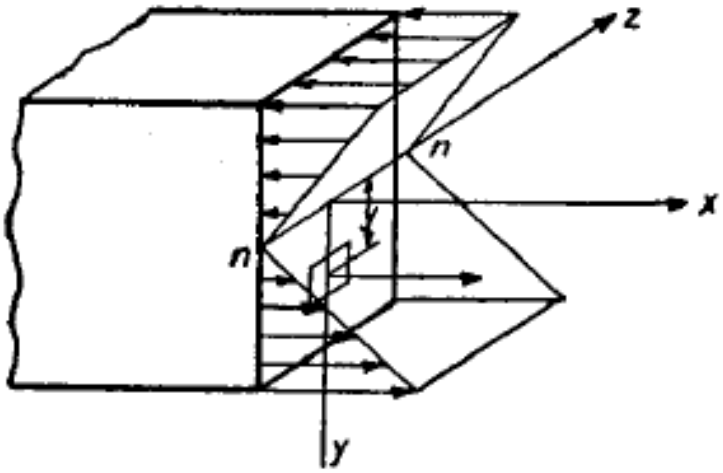

FIGURE 1.4 Répartition de contraintes axiales sur une section rectangulaire (Timoshenko, 1940)

La rupture successive des racines structurales du chablis est un événement important qui a un impact direct sur la rupture globale du système racines-sol (Coutts, 1983; Cucchi, 2004). Dans cette thèse, ce processus est modélisé par la rupture des racines individuelles en tension, en compression et en flexion gouvernée par une loi d'endommagement. Le lecteur est invité à lire l'Annexe B pour une description détaillée des éléments théoriques concernant la formulation d'une loi d'endommagement et de son développement numérique pour les racines dans un modèle d'ancrage FEM.

La résistance des racines de structure est également liée au matériau bois qui les composent. Or on dispose de peu de connaissance sur le bois de racines et le bois vert mesuré *in situ*. L'essentiel des travaux sur la mécanique du bois concerne le bois après récolte. Le bois est un matériau composite biologique dont la structure est principalement déterminée par ses propriétés de transports qui lui confèrent un caractère orthotrope (Kretschmann, 2010). La plupart des connaissances sur la mécanique des racines portent sur les racines fines responsables de l'acquisition de l'eau et des nutriments, et peu sur les racines ligneuses structurales responsables du support mécanique de l'arbre. Les propriétés des racines fines des plantes ont été largement étudiées dans le contexte de la stabilisation des sols en pente, de la prévention de l'érosion des sols et de la stabilisation des berges. Les racines agissent alors comme un élément de renfort à la résistance au cisaillement du sol (Ji et al., 2012; Mao et al., 2012a; Pollen and Simon, 2005; Schwarz et al., 2010; Waldron, 1977; Wu and Sidle, 1995). Les racines fines ont un comportement mécanique fragile en tension à la rupture, caractérisé par la courbe de réponse de la force de traction en fonction du déplacement axial (Figure 1.6 ; Abernethy and Rutherfurd (2001)). En revanche, la résistance en flexion et en compression des racines fines est faible et

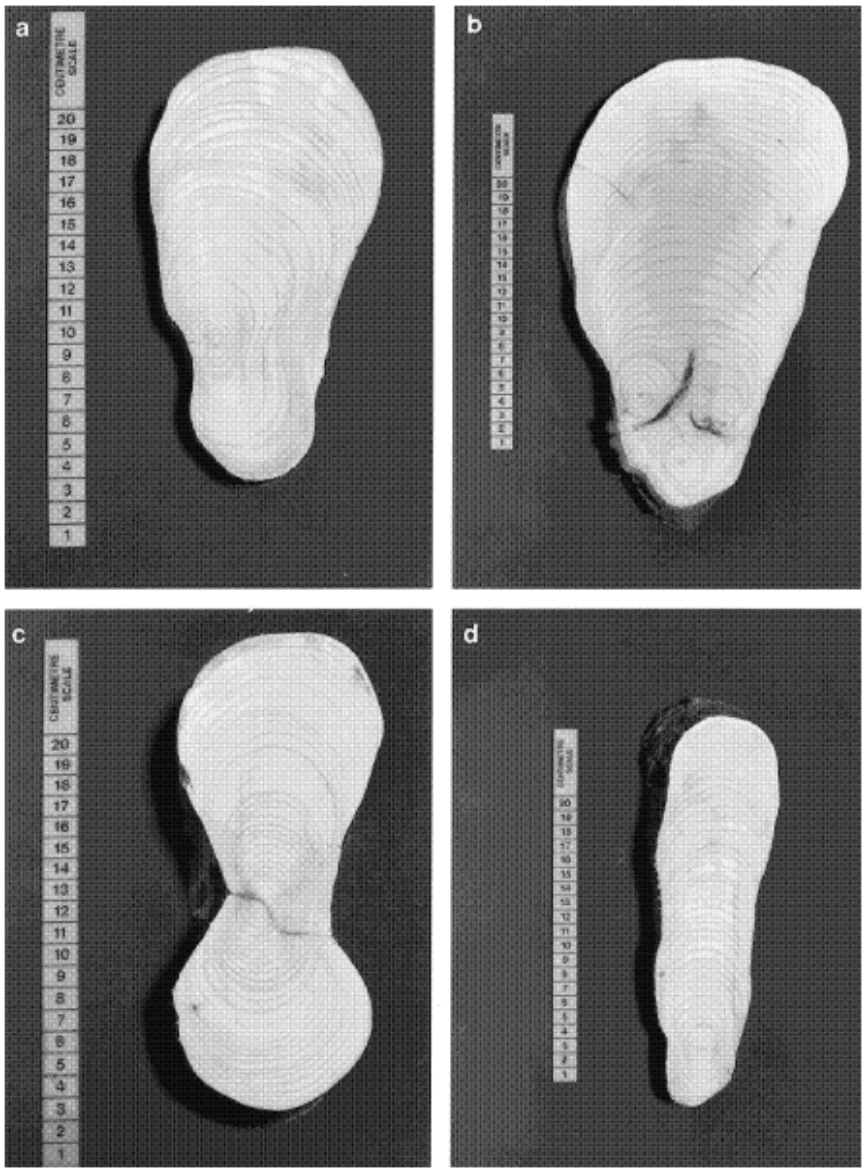

FIGURE 1.5 Ovalisation en formes de "I" (Figure (c)) ou "T" (Figure (a) et (b)) de la section droite des racines structurales localisées dans les secteurs orientés à la direction du vent dominant (Nicoll and Ray, 1996)

négligeable pour le renfort du sol. Pour les grosses racines ligneuses, la composition chimique (teneur en carbone) est proche de celle du bois du tronc (Bert and Danjon, 2006; Gifford, 2000), mais nous disposons de peu de mesures. Coutts (1983), Stokes et Mattheck (1996) et Niklas (1999) ont publié des mesures sur la résistance des racines en tension, en flexion ou en compression dont la plupart des valeurs publiées sont comparables à celles déterminées pour le bois du tronc. Certains résultats ont également relevé une augmentation de la résistance du bois de racines de structure pour des racines localisées dans des zones fortement sous contraintes

lors des mouvements de l'arbre sous le vent, ce qui laisse penser à une modification des tissus dans ces zones (Stokes and Mattheck, 1996; Stokes et al., 1997b).

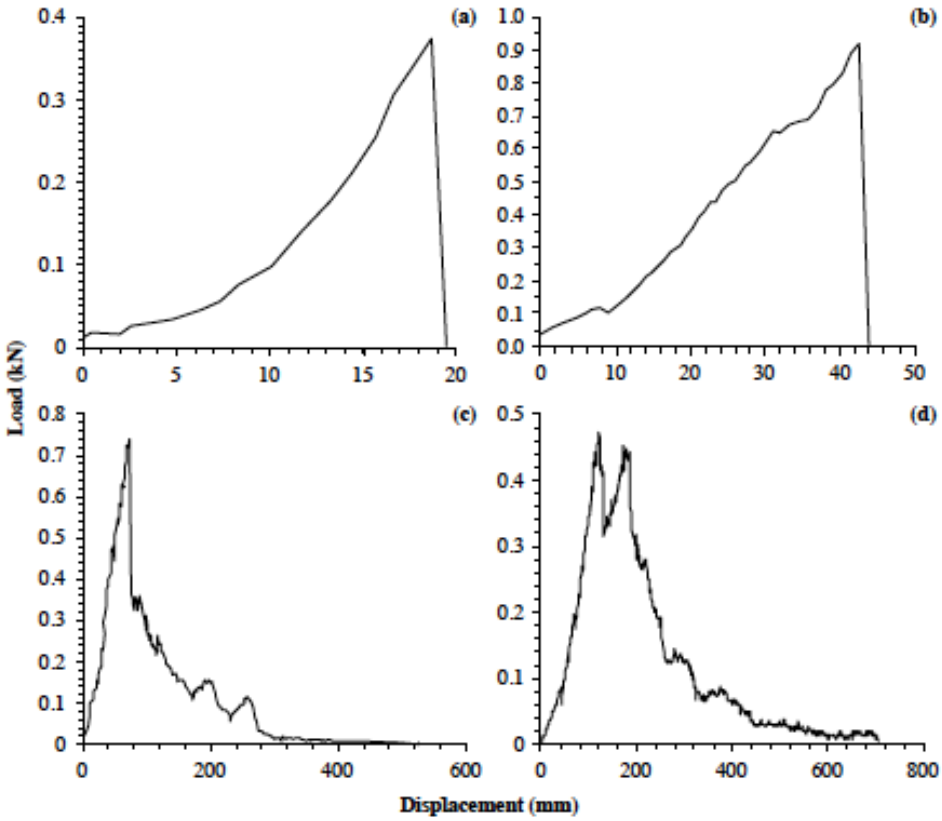

FIGURE 1.6 Essai de traction de racines (*Eucalyptus camaldulensis*). (a) racine dont le diamètre à la rupture est de 5.0 mm, mesurée en laboratoire ; (b) racine dont le diamètre à la rupture est de 6.9 mm, mesurée *in situ* en conditions sèches ; (c) racine dont le diamètre à la rupture est de 7.9 mm, mesurée *in situ* en conditions humides ; (d) racines ramifiées dont le diamètre à la rupture plus importante est de 4.3 mm, mesurées *in situ* en conditions humides (Abernethy and Rutherfurd, 2001).

Les propriétés mécaniques du bois de construction et d'industrie sont très bien connues. Elles sont en général mesurées en laboratoire en conditions de température et d'humidité contrôlées selon différents normes (Kretschmann, 2010). Ces études ont montré que ces propriétés sont sensibles à l'humidité de l'échantillon et aux procédures de stockages et de séchages préalables aux essais mécaniques (Dlouha, 2009; Follrich et al., 2006; Kretschmann, 2010). On s'attend à ce que les propriétés du bois vert diffèrent de celles du bois d'oeuvre principalement par son humidité. Une des façons d'estimer les propriétés du bois sur pied est ainsi actuellement d'utiliser des valeurs mesurées pour un bois saturé à 50% (Niklas and Spatz, 2010). Il est cependant possible d'estimer les propriétés du bois vert (c'est-à-dire contenant

plus de 30% d'eau, qui est le point de saturation des fibres), telles que la masse volumique, le module d'Young et le module de rupture, à partir des valeurs mesurées pour un taux d'humidité de référence (12% pour le bois sec à l'air) en se basant sur des lois de régression (Kretschmann, 2010).

1.3 Résistance mécanique du sol et interface racines-sol

Le processus d'arrachement fait intervenir différents modes de rupture : frottement à l'interface racines-sol, rupture des racines et rupture du sol. Face à cette complexité, une première approche consiste à décrire l'interaction mécanique entre les racines et le sol environnant en introduisant, pour les grands arbres, la notion de la plaque racines-sol. Cette plaque racines-sol ou plaque racinaire désigne la partie centrale souterraine de l'arbre qui agit principalement comme contrepoids aux moments de renversement (lié au poids de l'arbre, à l'action du vent). Elle peut être observée et mesurée après le chablis d'un arbre où une grande partie du système racinaire est soulevée et entourée par une motte de sol très compact (Figure 1.7) (Achim and Nicoll, 2009; Blackwell et al., 1990; Coutts, 1983, 1986; Peltola et al., 1999). La notion de la plaque racines-sol a été utilisée dans des relations empiriques reliant la capacité de l'ancrage racinaire d'un arbre aux dimensions de la plaque : la profondeur moyenne, le poids, la taille et la forme (Achim and Nicoll, 2009; Blackwell et al., 1990; Peltola et al., 1999). Cependant de telles relations sont difficilement utilisables en pratique car les dimensions de la plaque racinaire ne peuvent être connues qu'a posteriori. De plus, une telle approche est insuffisante pour analyser le rôle du sol et des propriétés d'interface sol-racines.

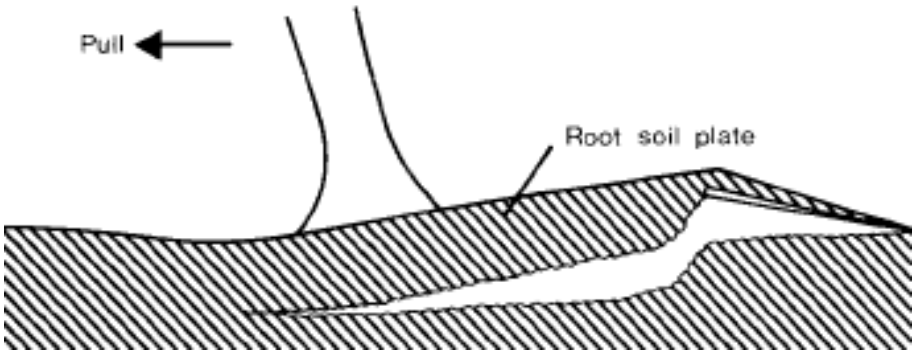

FIGURE 1.7 Plaque racines-sol d'un arbre à système racinaire traçant soulevé par la force de traction sur le tronc (Coutts, 1983)

Les modèles numériques développés plus récemment basés sur la méthode des éléments finis ouvrent la possibilité d'intégrer des connaissances sur la résistance mécanique du sol et sur les interactions sol-racines. Dans les modèles d'ancrage racinaire actuels, la résistance

mécanique du sol est modélisée à l'aide de modèles établis en mécanique des sols. Ces modèles sont un ensemble de lois phénoménologiques qui reproduisent le comportement d'un sol tel qu'il est observé lors d'essais de laboratoire : oedomètre, machine à cisailler, triaxial avec lesquels on reproduit différents types de sollicitation (compression, cisaillement, chargements cycliques...) (Fredlund et al., 1978; Gan et al., 1988). Les lois dépendent en général de la granulométrie du sol : on distingue le comportement des sols fins argileux de celui des sols sableux. Dans cette thèse, nous avons utilisé un modèle de type Mohr-Coulomb développé pour les sols sableux. La résistance au cisaillement τ du sol est décrit par :

$$\tau = \sigma_n \tan\phi + c \tag{1.5}$$

où σ_n est la pression normale exercée au plan de rupture, ϕ l'angle de frottement interne et c la cohésion du sol. L'estimation des paramètres c et ϕ s'effectue à l'aide de l'essai de cisaillement direct au laboratoire (Figure 1.8).

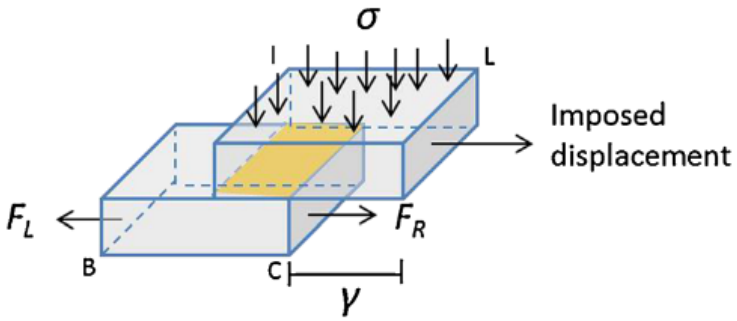

FIGURE 1.8 Essai de cisaillement direct du sol avec une machine à cisailler (Mao et al., 2014)

Dans les modèles d'ancrage par FEM qui intègrent la résistance du sol, le sol est considéré comme homogène et ses propriétés sont celles de sols utilisées en géotechnique (Dupuy et al., 2007; Rahardjo et al., 2009). Or, la résistance d'un sol de surface forestier dépend de sa porosité et de son état hydrique qui fluctuent dans l'espace et dans le temps. En effet, les pratiques sylvicoles (passage d'engin, travail du sol, débardage, etc.), les conditions climatiques et les processus biologiques (décomposition des matières organiques, présence de racines, poids de l'arbre et croissance de l'encombrement spatial des racines, etc.) ont des effets importants sur la résistance mécanique des sols (Keller and Hakansson, 2010; Saffih-Hdadi et al., 2009). Les forêts européennes sont souvent établies sur des parcelles à sol peu profonds, ils y développent donc des systèmes racinaires superficiels. La nappe phréatique fluctue selon les saisons, les précipitations hivernales sont relativement élevées, et les tempêtes sont en général accompagnées de pluies abondantes saturant les sols. En raison de cette hétérogénéité

du milieu, il semble donc important de mieux décrire les propriétés du sol dans les modèles d'ancrage.

Modéliser l'ancrage mécanique d'un arbre implique également de décrire les interactions mécaniques racines-sol. Les connaissances dont on dispose sur cet aspect proviennent des recherches sur l'augmentation de la cohésion du sol fournie par les racines fines, qui stabilisent les sols en pente, et sur la croissance racinaire. Comme nous l'avons vu dans la section précédente, la présence des racines fines dans le sol permet de renforcer le sol contre des glissements de terrain et l'érosion (Wu et al., 1979). Les processus de renforcements par les racines sont étudiés par des essais de cisaillement direct du sol dans lequel sont inclus des éléments de renfort analogues aux racines ou des racines réelles (Pollen, 2007; Schwarz et al., 2011). Lorsque le sol est sollicité en cisaillement, les efforts se transmettent aux racines situées dans la zone de cisaillement et elles se mettent en tension (Waldron, 1977). Une première approche consiste à décrire le sol par un modèle de Mohr-Coulomb et assimiler ce renforcement à une cohésion additionnelle au sol donnée par la relation suivante :

$$\tau = \sigma_n \tan\phi + c + \Delta S \tag{1.6}$$

où ΔS est la cohésion additionnelle due à la présence des racines fines. En particulier, cette cohésion peut être modélisée par :

$$\Delta S = \frac{A_r}{A} k \frac{\sin\beta + \cos\beta \tan\phi}{\sqrt{\sec\beta - 1}} \tag{1.7}$$

où l'on identifie d'abord la résistance en tension des racines caractérisée par le coefficient k, l'orientation des racines dans la zone de cisaillement par rapport à la normale du plan de cisaillement β et la proportion de l'aire occupée par les racines en rapport avec l'aire totale du plan de cisaillement dans le sol $\frac{A_r}{A}$ qui peut être interprétée par la quantité de racines fines dans la zone du sol (Waldron, 1977). Une seconde approche modélise le rôle des racines dans le processus de rupture de pente en décrivant la rupture des racines, leur géométrie et les frottements à l'interface racines-sol. Plusieurs méthodes permettent de modéliser ces interactions racines-sol : des modèles par FEM tels que développés dan mon Master 2 (Mao et al., 2014), des modèles par Discrete Element Method (DEM) ou des Fiber-Bundle Models (FBM) (Bourrier et al., 2013; Mao et al., 2014; Pollen and Simon, 2005; Schwarz et al., 2010). Ces travaux ont montré l'effet des propriétés géométriques (longueur, diamètre, ramification, tortuosité) et mécaniques (module d'Young, résistance en tension) des racines sur les forces de frottement racines-sol (Commandeur and Pyles, 1991; Pollen and Simon, 2005; Schwarz et al., 2010). Par ailleurs, les interactions mécaniques entre les racines et le sol ont aussi été examinées

pour étudier l'expansion (ou la croissance) des racines en fonction de l'impédance mécanique du sol. L'impédance mécanique et le stress hydrique sont les deux facteurs principaux qui limitent l'élongation des racines dans un sol sec (Bengough et al., 2006).

Nous allons voir dans la section suivante qu'une meilleure compréhension de l'ancrage implique d'améliorer la représentation de la résistance du sol et des interactions mécaniques sol-racines.

1.4 Modélisation de l'ancrage racinaire

1.4.1 Relations empiriques des modèles de risque au vent

Une première approche pour modéliser l'ancrage racinaire est celle utilisée dans les modèles de risque au vent qui nécessite de comparer le moment exercé par le vent à la résistance de l'arbre à l'arrachement. La résistance de l'arbre au renversement est alors définie comme étant le moment de flexion critique au-delà duquel l'arbre est renversé en se basant sur la réponse de l'arbre à un essai de treuillage statique (Figure 1.10). Le modèle de risque HWIND utilise la relation suivante :

$$TM_c = \frac{gMass\bar{D}}{A_{rsw}} \tag{1.8}$$

où TM_c est le moment critique de déracinement à la contribution mécanique de la plaque racines-sol, i.e. $gMass$ le poids de la plaque racinaire, $\bar{D}$ la profondeur moyenne de la plaque et A_{rsw} un coefficient représentant la proportion de la contribution de la plaque (Peltola et al., 1999). Tandis que dans les modèles GALES et FOREOLE, la méthode pour calculer le moment d'ancrage est basée sur l'analyse des résultats issus d'une campagne d'essais de treuillage, donnée par la relation suivante :

$$TM_c = C_{reg}SW \tag{1.9}$$

où C_{reg} est une constante de régression linéaire et SW le poids du tronc.

1.4.2 Modèles analytiques

Les travaux expérimentaux de Coutts (1983; 1986) ont permis de formaliser les différents mécanismes de résistance mis en jeu lors du renversement d'un arbre à partir d'essais sur Sitka spruce, essence caractéristique des morphologies racinaires de type traçant. Coutts (1983; 1986) a alors proposé une décomposition du système selon quatre composantes d'importance décroissante :

1. la résistance en tension et au cisaillement des racines au vent ;

2. le poids de la plaque racines-sol ;
3. la résistance en flexion et en compression des racines sous le vent ;
4. la résistance du sol autour de la plaque racines-sol.

Blackwell et al. (1990) ont proposé un modèle analytique en se basant sur la décomposition de Coutts (1986). Leur modèle est composé de :

1. une description mathématique de deux moteurs aériens qui entraînent le renversement de l'arbre : le moment dû à la force appliquée à la tige et le moment dû à la masse du houppier ;
2. une description mathématique des composantes souterraines : le moment dû au poids de la plaque racines-sol, et le moment dû aux interactions mécaniques racines-sol.

Ces dernières sont modélisées par des efforts de ressorts qui relient la plaque racines-sol et le sol environnant. Une version semi-analytique du modèle a été proposée en intégrant des relations empiriques et adaptant la forme de la plaque racines-sol de façon plus réaliste (Achim and Nicoll, 2009). Ces modèles n'ont pas été retenus pour la thèse car elle vise à mieux comprendre le rôle respectif de l'architecture du système racinaire et de la résistance des matériaux (sol, racines) et ces modèles analytiques ne représentent pas ces deux composantes explicitement.

1.4.3 Modélisation numérique

La modélisation numérique basée sur la méthode des éléments finis s'est avérée très utile pour traiter des interactions vent-plante (Dupuy et al., 2007; Fourcaud et al., 2003; Moore and Maguire, 2008; Sellier et al., 2006). Dans la même veine que ces travaux, l'ancrage des arbres dans le sol a été simulé par quatre modèles FEM différents jusqu'à présent. Ce type de modélisation est très intéressant car il permet de traiter ensemble la structure du système, les propriétés des matériaux et les conditions de chargement et d'intégrer ainsi des connaissances en architecture des systèmes racinaires et en biomécanique (Figure 1.9, Dupuy et al. (2007)).

Méthode des éléments finis

La méthode des éléments finis (Finite Element Method) consiste à résoudre numériquement des équations différentielles ou aux dérivées partielles. De manière générale, la FEM repose sur la discrétisation des domaines (temps, champ de variables) dans la formulation mathématique du problème bien posé à étudier (mécanique, hydraulique, thermique, etc. souvent des problèmes d'ingénierie) pour donner une solution approchée. Ces problèmes sont souvent caractérisés par des non linéarités.

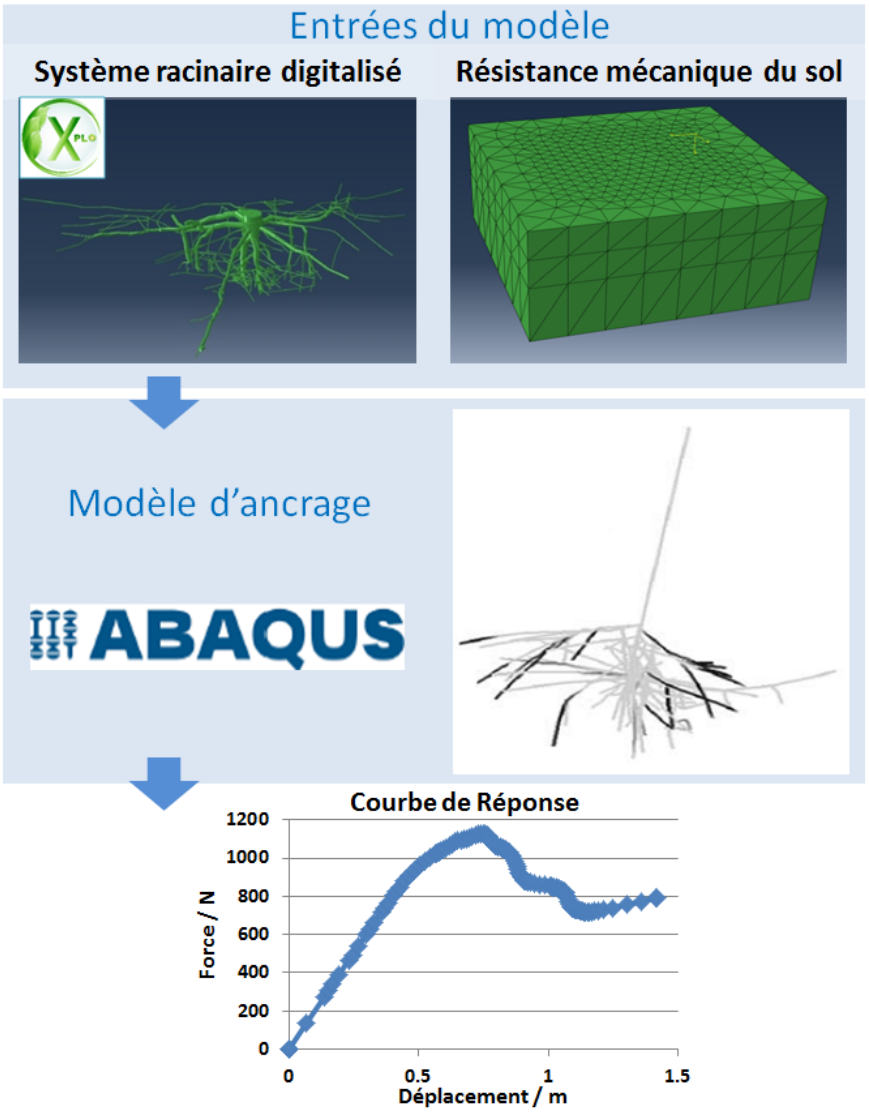

FIGURE 1.9 Démarche de la modélisation numérique de l'ancrage racinaire, d'après Défossez et al. (2014)

Le problème de déracinement, comme beaucoup d'autres problèmes d'ingénierie, peut être décrit par un essai de flexion statique comme l'essai de treuillage, ou en prenant en compte des chargements dynamiques comme ceux générés par le vent. Les non-linéarités du problème d'ancrage sont nombreuses. Elles concernent les propriétés des matériaux : les comportements des racines et du sol sont non linéaires (élastique et quasi-fragile pour les racines ; élastique et plastique pour le sol) ; elles peuvent également être liées à des transformations géométriques dans le cas des grands déplacements ou des grandes déformations. Le processus de déracinement peut être mathématiquement formulé par un ensemble d'équations aux dérivées partielles : (i) les équations de conservation de la masse, (ii) les équations de mouvements, (iii) les lois de

comportement des matériaux et de contacts, (iv) les conditions initiales et les conditions aux limites.

Les variables de ces équations peuvent éventuellement varier dans le temps s'il s'agit d'un problème dynamique. Dans les modèles d'ancrage, on a jusqu'à présent considéré un chargement statique. Comme la plupart des équations différentielles ou des équations aux dérivées partielles non-linéaires ne peuvent pas être résolues analytiquement, des méthodes numériques telles que la FEM sont nécessaires pour calculer des solutions numériques approchées.

Des modèles numériques d'interaction racines-sol ont été implémentés dans différents codes de calcul : ABAQUS (Dupuy et al., 2005a,b, 2007; Fourcaud et al., 2008), PLAXIS (Mickovski et al., 2011), SIGMA/W (Rahardjo et al., 2009). Ces codes FEM présentent des caractéristiques similaires. Dans cette thèse, on a utilisé le logiciel Abaqus (Dassault systèmes ; http://www.3ds.com/products/simulia/overview/), connu pour sa capacité à résoudre des problèmes d'ingénierie non linéaires tels que le nôtre. Le formatage des fichiers décrivant le problème à résoudre et les nombreuses interfaces entre Abaqus et d'autres logiciels facilitent son utilisation. On peut ainsi modéliser des géométries complexes construites par ailleurs et implémentées sous Abaqus. De plus, Abaqus permet d'utiliser une multitude de lois de comportement des matériaux et de contacts. Celles-ci sont soit disponibles dans la bibliothèque Abaqus soit nécessitent d'être programmées par l'utilisateur.

Modélisation de l'architecture

Différentes méthodes ont été utilisées jusqu'à présent pour représenter des structures racinaires dans les modèles d'ancrage par FEM. Fourcaud et al. (2008) et Rahardjo et al. (2009) ont utilisé des représentations 2D très simplifiées (forme en croix plus ou moins ramifiée). Dupuy et al. (2005b) ont développé un logiciel SIMUL3R pour générer des systèmes racinaires virtuels permettant de reproduire les quatre catégories d'architectures : système racinaire en cœur, traçant, pivotant et herringbone. Plus récemment l'UMR AMAP a développé un logiciel appelé Xplo (http://amapstudio.cirad.fr/soft/xplo/start), intégré dans la plateforme Amapstudio (http://amapstudio.cirad.fr/ ; Griffon and de Coligny (2014)), destiné à coder, visualiser et analyser des données d'architecture 3D de plantes (Figure 1.11). Il peut être utilisé pour créer, importer ou exporter des architectures. Ce logiciel permet aujourd'hui d'intégrer des systèmes racinaires complexes sous Abaqus afin de réaliser des simulations numériques d'ancrage racinaire (http://amapstudio.cirad.fr/soft/xplo/screenshots). Dans le cadre de cette thèse, on utilise l'application Xplo pour importer les données complètes de l'architecture d'un système racinaire mesuré et enregistré dans un fichier au format MTG (Godin et al., 1999), et les exporter en les écrivant dans un fichier "INPUT" qui peut être lu par le logiciel Abaqus.

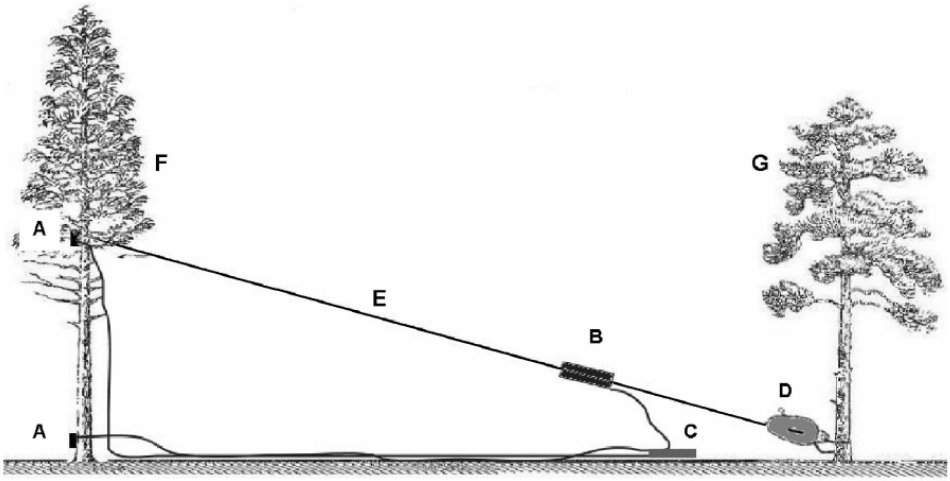

FIGURE 1.10 Essai de treuillage statique (Nicoll et al., 2006) : l'essai de treuillage est conçu pour étudier le processus statique de renversement de l'arbre. Un treuil (D) fixé à un arbre voisin (G) applique un déplacement constant à une certaine hauteur du tronc via une sangle qui relie le treuil et l'arbre en question (F). Un capteur de force (B) est installé au niveau de la sangle (E) pour mesurer la force de traction appliquée au tronc au cours de l'essai. Des inclinomètres (A) sont installés à différentes hauteurs du tronc, en particulier à la base du tronc et à la hauteur de traction, pour mesurer l'angle de rotation du tronc par rapport au vertical au cours de l'essai. Pendant l'essai, une centrale d'acquisition de données (C) est utilisée pour enregistrer et coordonner ces variables mesurées (Figure 1.10). A la sortie, le moment est calculé par la force de traction et la position du point de traction par rapport à la base du tronc. La courbe de réponse est formée par le couple de moment et angle de rotation à la base du tronc. On identifie sur la courbe le maximum du moment en tant que moment critique, la principale caractéristique de la résistance de l'arbre au vent. L'idée de l'essai de treuillage est reprise par les modèles d'ancrage racinaire pour modéliser le renversement statique.

Application et limites de la FEM

Les modèles d'ancrage racinaire par FEM développés jusqu'à présent simulent l'action du vent sur le houppier par l'application d'un déplacement horizontal au sommet du tronc de l'arbre. Ce tronc, représenté par une tige, est directement collée au sommet de la souche, et le système racinaire est plongé dans une matrice de sol. Les trois principales composantes en interaction sont : l'architecture d'un système racinaire, le milieu de sol et une tige rigide (pour négliger la déformation du tronc). Les propriétés des matériaux (essentiellement mécaniques) sont renseignées pour le sol et les racines. Les interactions mécaniques racines-sol sont modélisées par les contraintes cinématiques linéaires imposées au niveau des nœuds des racines au voisinage des nœuds de sol. Les sorties étudiées des modèles sont la distribution des contraintes dans les racines et le sol, et la courbe de réponse moment - rotation calculée à la base de la tige au cours de treuillage. Ces modèles FEM permettent de simuler des courbes de réponse qui sont

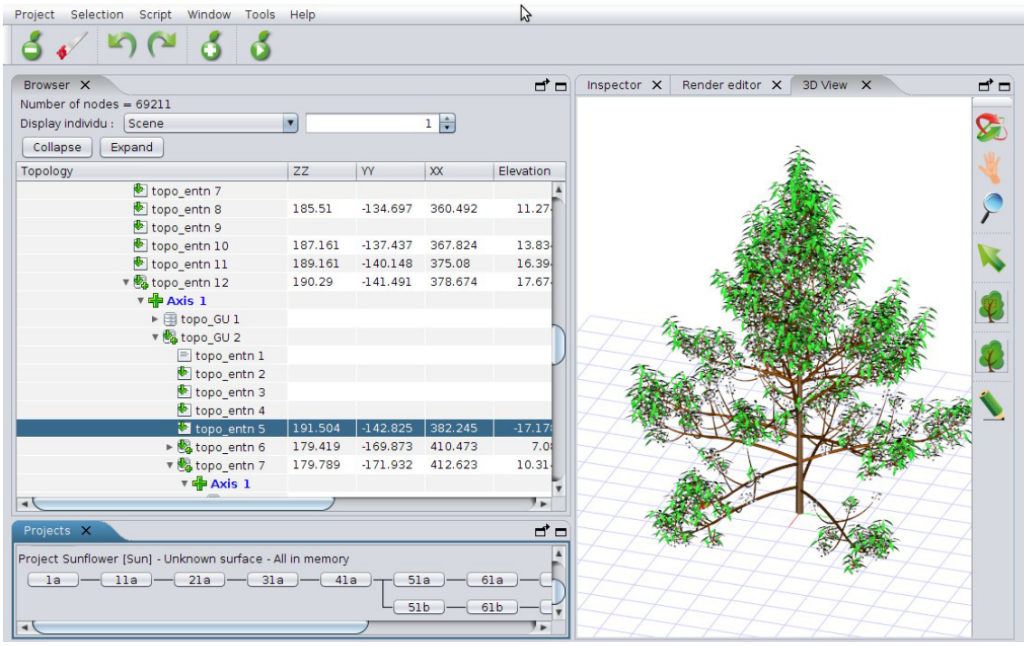

FIGURE 1.11 Généralités du logiciel Xplo (de Coligny and Griffon, 2011)

du même ordre de grandeurs que les valeurs mesurées lors d'essais de treuillage (Dupuy et al., 2007). Ils ont permis de simuler les effets de l'architecture du système racinaire et les effets des propriétés du sol. Mais ils présentent certaines limites, quant aux traitements de l'architecture racinaire et à la résistance des matériaux, que nous avons cherchées à dépasser dans la thèse. Premièrement, trois de ces modèles utilisent une architecture du système racinaire théorique et simplifiée. Or des maquettes en 2 dimensions ou des morphologies théoriques générales sont probablement insuffisantes pour espérer capter des effets architecturaux. Seuls Dupuy et al. (2007) ont utilisé des architectures 3D complexes réelles mais les simulations sont trop peu nombreuses pour pouvoir généraliser. Deuxièmement, la description des propriétés mécaniques des racines est basée sur des paramètres théoriques. La fragilité et la rupture des racines suivant différents types de sollicitation (tension, compression et flexion) sont des éléments essentiels qui ne sont pas pris en compte par ces modèles. De même, les propriétés mécaniques des sols (sableux et argileux) sont renseignées par des valeurs théoriques pour des sols utilisés en géotechnique en considérant le milieu comme homogène. Et enfin les interactions mécaniques à l'interface racines-sol sont simplifiées sans que l'on connaisse bien l'effet de ces simplifications sur le calcul.

Pour conclure, nous avons donc opté pour un modèle FEM utilisant le code Abaqus en l'appliquant à l'ancrage du *P. pinaster*. Le modèle développé dans la thèse vise à améliorer la compréhension du processus de déracinement de l'arbre, ce qui implique :

1. d'incorporer des architectures de systèmes racinaires réalistes et représentatives d'une essence donnée ;
2. de modéliser les propriétés des matériaux pour les systèmes racinaires et le sol en utilisant les connaissances actuelles sur ces matériaux (bois de racines, sol forestier) ;
3. d'établir les relations entre la capacité de l'ancrage racinaire d'une part et de différents facteurs morphologiques et des matériaux (traits architecturaux ; les dimensions des racines ; propriétés des racines et du sol) et d'autre part de hiérarchiser ces facteurs.

Chapter 2

Tree stability under wind: simulating uprooting with root breakage using a finite element method

Oral presentation

Ming Yang, Pauline Défossez, Thierry Fourcaud. Improving finite element models of roots-soil mechanical interactions. In *Proceedings of the 7th International Conference on Functional-Structural Plant Models*, page 204-206, 2013

Publication

Ming Yang, Pauline Défossez, Frédéric Danjon, Thierry Fourcaud. Tree stability under wind: simulating uprooting with root breakage using a finite element method. *Annals of botany*, page mcu122, 2014a

Abstract

Background and Aims

Windstorms are the major natural hazard affecting European forests, causing tree damage and timber losses. Modelling tree anchorage mechanisms has progressed with advances in plant architectural modelling, but it is still limited in terms of estimation of anchorage strength. This paper aims to provide a new model for root anchorage, including the successive breakage of roots during uprooting.

Methods

The model was based on the finite element method. The breakage of individual roots was taken into account using a failure law derived from previous work carried out on fibre metal laminates. Soil mechanical plasticity was considered using the Mohr–Coulomb failure criterion. The mechanical model for roots was implemented in the numerical code ABAQUS using beam elements embedded in a soil block meshed with 3-D solid elements. The model was tested by simulating tree-pulling experiments previously carried out on a tree of *Pinus pinaster* (Maritime pine). Soil mechanical parameters were obtained from laboratory tests. Root system architecture was digitized and imported into ABAQUS while root material properties were estimated from the literature.

Key Results

Numerical simulations of tree-pulling tests exhibited realistic successive root breakages during uprooting, which could be seen in the resulting response curves. Broken roots could be visually located within the root system at any stage of the simulations. The model allowed estimation of anchorage strength in terms of the critical turning moment and accumulated energy, which were in good agreement with *in situ* measurements.

Conclusions

This study provides the first model of tree anchorage strength for *P. pinaster* derived from the mechanical strength of individual roots. The generic nature of the model permits its further application to other tree species and soil conditions.

Key words

Tree anchorage, root mechanical properties, soil mechanical strength, failure modelling, functional–structural plant modelling, finite element method, ABAQUS, coarse root architecture, windthrow, *Pinus pinaster*, Maritime pine.

2.1 Introduction

Windstorms are among the primary causes of destruction in forests (Gandhi et al., 2008; McCarthy et al., 2010). In particular, they are the major hazard affecting European forests, causing tree and timber losses. Moreover, reported wind-induced damage in Europe has increased since the last century due to forest expansion (Gardiner et al., 2010). The increasing stock and average age of European forests and the observed ongoing climate changes, with the prediction of stronger windstorms (Della-Marta and Pinto, 2009), may also lead to a growing wind risk. For instance, storm Klaus, which hit southern Europe in January 2009, resulted in an estimated 43 000 000 m^3 of timber being blown down in southwest France, including a volume of 37 000 000 m^3 for *P. pinaster* (source from GPMF, 2011).

Numerous efforts have been made to model forest damage caused by wind (Gardiner et al., 2008). They have led to several predictivemodels for forest damage (overturning, stem breakage), i.e. HWIND, GALES and FOREOLE (Ancelin et al., 2004; Gardiner et al., 2000; Peltola et al., 1999). These models included empirical relationships to determine the tree's resistance to overturning based on tree-pulling tests. They are therefore limited to the site conditions for which they were built (GALES and FOREOLE). Moreover, the resistance to overturning predicted by these empirical relationships used rough and simplified parameterization (HWIND).

Tree anchorage capacities vary with time and result from complex interactions between growing roots and their physical and biological environment. Previous observations and experimental studies have reported that part of root architecture plasticity is due to biomechanical acclimation when trees are subjected to wind loads (Coutts et al., 1999; Danjon et al., 2013a; Lundström et al., 2007; Nicoll and Ray, 1996; Nicoll et al., 2008; Stokes et al., 1995; Tamasi et al., 2005). In particular, biomechanical acclimation of trees has been proved in the case of adult *P. pinaster* trees, for which asymmetrical patterns can play an important mechanical role in tree anchorage (Danjon et al., 2005). In the context of global change it is very important for wind risk prediction models to take into account the ability of trees to develop stronger anchorage with specific root traits as a biomechanical response to the wind. We therefore have to provide a tool capable of predicting tree stability by taking into account the acclimation of root systems and changes in soil strength as a function of climate conditions. This requires progress in understanding the uprooting process as a function of tree characteristics and soil material properties. The first studies on tree uprooting mechanisms were based on the experimental work of Coutts (1983; 1986), who also developed the first systematic method of analysing tree anchorage (Coutts, 1986). This author quantified the relative impacts of different anchorage components on Sitka spruce, i.e. root–soil weight, root material strength under tension and soil strength, on the overturning resistance of spruce. This method led to the first mechanistic

model of tree anchorage (Blackwell et al., 1990) that described the root anchorage strength in terms of these components. Understanding of the anchorage mechanism progressed with the use of numerical analysis and advances in plant architecture digitizing (Dupuy et al., 2005b, 2007; Fourcaud et al., 2008). This approach used the finite element method (FEM) to calculate the deformation of root–soil systems in three dimensions. Real and simulated root systems with their specific architectural properties were considered in the simulations. These analyses allowed comparison of the theoretical anchorage performances of different root types, i.e. tap-, herringbone-, heart- and plate-like root systems, in clay and sandy soils. In addition, Fourcaud et al. (2008) attempted to quantify the relative roles of root components, e.g. superficial laterals, deep roots and tap roots, in anchorage strength in different soil types using a simple 2-D FEM model. Rahardjo et al. (2009) developed a finite element model of root anchorage and used a parametric study to examine the influence of soil properties. Thus, numerical models have been used essentially to investigate the influence of root architecture on tree anchorage using theoretical parameters for soil and roots. Less is known about the failure mechanism, which is crucial for predicting the occurrence of uprooting. This implies to better understand the effect of soil–root friction, root strength and soil strength on the whole response of the root system involved in the overturning process.

Our paper has two objectives. Firstly it presents a new model of tree anchorage that simulates the root breakage mechanism during tree uprooting, and secondly it tests this model in comparison with a field experiment in the case of young *P. pinaster*, which has simpler root architecture than adult specimens. In the first section we present the basis of the model and the tree-pulling test performed in the field. In the second section, we analyse the simulated response of the whole root system and compare it with measurements, and in the last section we discuss the model's capacity to simulate uprooting.

2.2 Materials and Methods

2.2.1 Anchorage model

The FEM model presented here is based on the initial work by Dupuy et al. (2007) and uses the ABAQUS software, version 6.13 (http://www.3ds.com/products-services/simulia/portfolio/Abaqus/). The model is composed of three parts (Figure 2.1):

1. the parallelepiped soil domain;
2. the root system;
3. a perfectly rigid stem used as a lever arm to mimic tree uprooting.

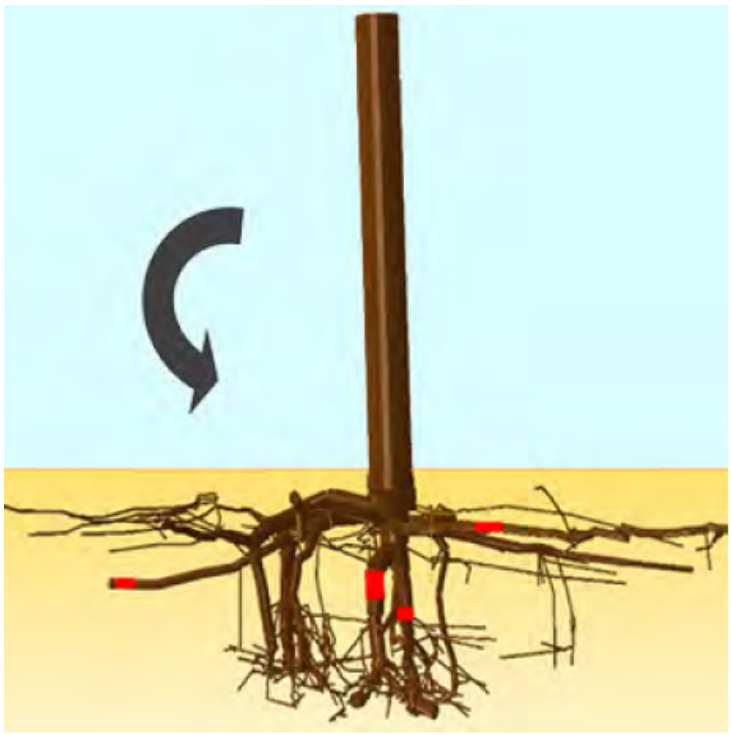

Figure 2.1 Anchorage model with root system architecture and soil properties measured for tree-pulling simulations. Model outputs are the response curve of turning moment as a function of deflection angle at the stem base and the total energy supplied by the pulling force. Deflection angle is defined as the angle between the vertical and the stem.

All relevant details not given here can be found in Dupuy et al. (2007). The vertical rigid stem was tied to the top of the stump of the root system; therefore, the stem base and the top of the stump always had the same angular displacement. The 3-D root architecture was modelled as an assemblage of discretized beams with a defined topology, branching pattern and geometry. It was imported in ABAQUS from the software Xplo (http://amapstudio.cirad.fr/soft/xplo/start; Griffon and de Coligny (2014)) dedicated to the encoding and visualization of plant architectures.

In this new model, the developments were focused on root–soil interaction, the mechanical behaviour of root material and the characteristics of the soil. Due to the complexity of meshing root architecture with 3-D solid elements, the roots were considered as embedded beam elements. We evaluated the relevance of this choice in a preliminary study carried out on a 3-D direct shear test of a soil block with root inclusions. Simulations considering roots modelled with embedded beam elements were compared with simulations using 3-D solid elements and root–soil interface friction properties (see Appendix of Annexe A). This study concluded that (1) the embedded beam elements mimicked the friction behaviour at the root–soil interface with

a friction coefficient of 0.1; and (2) for friction coefficients ranging from 0.1 to 0.9, the relative difference between the two approaches was always < 21% during the entire shear process. Embedded beam elements were then used in the anchorage model, implying that all the roots were slender structures embedded in the soil region. The roots were meshed with 3-D two-node linear Timoshenko beam elements with circular cross sections (B31 in the ABAQUS element library).

The anchorage model described above allows the tree anchorage behaviour of various tree species to be modelled under different soil conditions. In our study, we chose a specific case of *P. pinaster* planted in sandy soil. The inputs of the model were:

1. a digitized root system of *P. pinaster* excavated after an *in situ* tree-pulling experiment;
2. soil properties from soil measurements in the laboratory;
3. root material properties from data taken from the literature, as described in the following sections.

The model outputs were expressed by using response curves, i.e. 'turning moment' versus 'deflection angle at the stem base' and the energy supplied to the system during uprooting.

Formalism of individual root rupture

In the previous modelling work of Dupuy et al. (2007), the roots could only yield in the same way as metals, which exhibit plastic-like yielding, and the stresses remained stored in the roots after reaching the plasticity criterion. However, the rootswere expected to exhibit brittle behaviour in tension, with their cumulated stress released and redistributed to the remaining roots during the uprooting process. Such features have been repeatedly observed and modelled when considering soil reinforcement by fine roots with diameter generally < 1 cm (Abernethy and Rutherfurd, 2001; Pollen, 2007; Pollen and Simon, 2005). Therefore, roots were modelled as brittle material in the present root anchorage model. An elastic failure law based on continuum damage mechanics was developed for roots under tension, compression and bending, based on previous constitutive laws regarding fibre metal laminates (Linde et al., 2004). The law described by Linde et al. (2004) was adapted for wood beam elements and implemented in ABAQUS through the UMAT user subroutine. In this model, roots are elastic in their initial state. During incremental loading, the damage initiation criterion is evaluated at each material point in every beam cross-section to detect the onset of damage. If the damage initiation criterion is reached, root stiffness degradation can be derived from the damage

evolution law. The linear elastic behaviour defined in the beam cross section axis is given by:

$$\begin{pmatrix} \sigma_{11}^{el} \\ \tau_{21}^{el} \\ \tau_{31}^{el} \end{pmatrix} = \Big[\mathbf{C}\Big] \cdot \begin{pmatrix} \varepsilon_{11}^{el} \\ \gamma_{21}^{el} \\ \gamma_{31}^{el} \end{pmatrix} \tag{2.1}$$

and

$$\Big[\mathbf{C}\Big] = \begin{bmatrix} E_r & 0 & 0 \\ & G_r & 0 \\ sym & & G_r \end{bmatrix} \tag{2.2}$$

where σ_{11}^{el}, τ_{21}^{el} and τ_{31}^{el} represent the beam's elastic axial stress component and two elastic shear stress components along two perpendicular directions in the cross-section, respectively; E_r and G_r are modulus of elasticity and shear modulus, respectively; $\Big[\mathbf{C}\Big]$ is the non-degraded root stiffness tensor in its matrix form; ε_{11}^{el}, γ_{21}^{el} and γ_{31}^{el} represent the axial strain component and two shear strain components, respectively. The damage initiation criterion f is defined in terms of ultimate tensile strain ε_{11}^{t}, ultimate compressive strain ε_{11}^{c} and actual strain ε_{11}. Damage onset occurs when fulfilling the criterion:

$$f = \sqrt{\frac{\varepsilon_{11}^{t}}{\varepsilon_{11}^{c}}\varepsilon_{11}^{2} + (\varepsilon_{11}^{t} - \frac{{\varepsilon_{11}^{t}}^{2}}{\varepsilon_{11}^{c}})\varepsilon_{11}} > \varepsilon_{11}^{t} \tag{2.3}$$

where

$$\varepsilon_{11}^{t} = \frac{\sigma_{11}^{t}}{E_r} \tag{2.4a}$$

$$\varepsilon_{11}^{c} = \frac{\sigma_{11}^{c}}{E_r} \tag{2.4b}$$

σ_{11}^{t} and σ_{11}^{c} being the tensile strength and compressive strength of the root material, respectively, and f is zero for axial strain ε_{11} ranging from 0 to $\varepsilon_{11}^{t} - \varepsilon_{11}^{c}$. Beyond this small interval it increases with increasing axial strain in both tensile and compressive directions. Figure 2.2 (a) gives an example of the behaviour of $f - \varepsilon_{11}^{t}$ (using data SA5, Table 2.3). As long as the damage initiation criterion is reached, the damage variable d is defined as the damage evolution law:

$$d = 1 - \frac{\varepsilon_{11}^{t}}{f} \exp\Big(\frac{-E\varepsilon_{11}^{t}(f - \varepsilon_{11}^{t})L^{c}}{G_f}\Big) \tag{2.5}$$

where L^{c} in our case is the characteristic length of the beam element and G_f is the fracture energy of the root material. The damage variable d is valid and takes continuous values from 0 to 1 from the axial failure strains defined by f in the compressive and tensile directions. Figure

2.2 (b) gives an example of the behaviour of d in the tensile direction (data set SA5 of Table 2.3). The damage variable d increases abruptly, which means our constitutive law models root brittleness correctly. Finally, stiffness degradation in the root material is modelled by including the damage variable in the stiffness matrix as follows:

$$[\mathbf{C_d}] = \begin{bmatrix} (1-d)E & 0 & 0 \\ & (1-d)G & 0 \\ sym & & (1-d)G \end{bmatrix} \tag{2.6}$$

This shows that, after reaching the damage initiation criterion, the evolution of d causes the stiffness in the root material to decrease progressively. In our case, convergence difficulties occurred during calculations due to the complex geometry (the multi-branched root system) and large deformations. Thus, viscous regularization is applied to the damage variable d to improve convergence, and the regularized damage variable d^v is used in the program instead of d:

$$\dot{d}^v = \frac{1}{\eta}(d - d^v) \tag{2.7}$$

where η is the viscosity parameter controlling the rate at which d^v approaches the true damage variable d. The value of η is assumed to be small compared with the size of the increment to satisfy the assumption of quasi-brittle material.

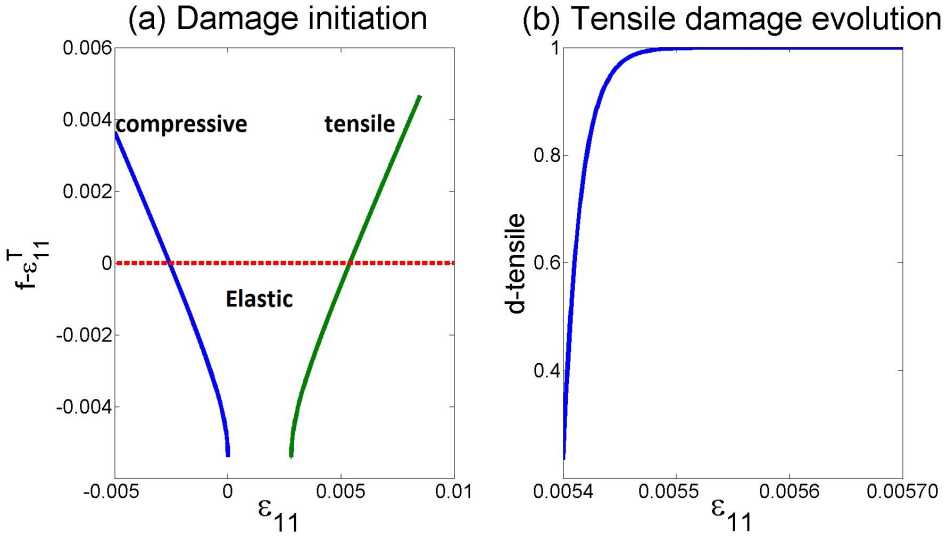

Figure 2.2 Root failure behaviour described by the constitutive law. (a) Damage initiation criterion $f - \sigma_{11}^t$ compared with 0; green curve above 0 (red horizontal line) means damage initiation in the tensile direction, blue curve above 0 means damage initiation in the compressive direction and both below 0 means an elastic state. (b) Damage (d) developed in the tensile axial direction.

Verification of the model for individual root failure

Before applying the constitutive law to the whole root system, it is necessary to test whether it reproduces the brittle rupture of the root material; rupture is expected to occur at the strength limits (σ_{11}^t or σ_{11}^c) with a sharp decrease in stress after failure. Tensile, compressive and bending tests were performed numerically in ABAQUS on a cantilever beam 1 m in length and 0.04 m in diameter, with a characteristic length ($L^c = 0.1\ m$) and the root material properties for SA5 given in Table 2.2. Displacement was separately imposed at the free end of the beam in the tensile direction, the compressive direction and perpendicular to the axial direction (Figure 2.3). Panels 1, 2 and 3 in Figure 2.3 (b) show the force-displacement curves obtained at the free tip of the beam during calculations for tensile, compressive and bending simulation tests, respectively. Figure 2.3 (b)-4 illustrates the numerical effect due to the viscous regularization parameter η. Panels 1 and 2 in Figure 2.3 (b) show that the root tensile and compressive strength predicted by tests agree well with the input σ_{11}^t and σ_{11}^c. Root compressive behaviour is as brittle as that in tension and the root fails in compression at a lower axial strain, while the degradation of bending strength and stiffness is more gradual (Figure 2.3 (b)-3). Parameter η for viscous regularization was calibrated by beam tensile tests with five different η values ranging from 0.00001 to 0.1, compared with the increment of 0.02 (Fig. 2.3 (b)-4). The three smaller η values (0.00001, 0.0001 and 0.001) predict curve behaviour similar to that without viscous regularization. However, the results from larger η values (0.01 and 0.1) predict less brittle tensile behaviour and overestimate the tensile strength of the root specimen. Thus, small η values compared with the characteristic size of increments should be used to avoid numerical discrepancies when modelling root mechanical behaviour. In the following, simulations hold for $\eta = 0.000075$.

2.2.2 Field experiment and parameter measurements

Site and tree-pulling experiment

A tree-pulling experiment was carried out on 24 April 2012 on a selected 13-year-old *P. pinaster* tree 0.18 m in diameter at breast height (Nézer forest in the southwest of France, altitude 15 m, latitude 44.6/44°36'0" N, longitude –1.03333/1°1'60" W; la Mairie du Teich). In 2012 the site had a total yearly rainfall of 846.7 mm and a mean temperature of 9.2 °C (Météo France). The pulling direction was perpendicular to the prevailing wind direction (northwest). The experimental protocol was similar to that used by Nicoll et al. (2006) and many others (Coutts, 1986; Cucchi et al., 2004; Kamimura et al., 2013; Moore, 2000). The selected tree was overturned with a motorized winch (WinchMax 7550, 5681 kg; Winchmax, UK; http://www.winchmax.co.uk/). The cable was attached to the stem of the pulled tree at the

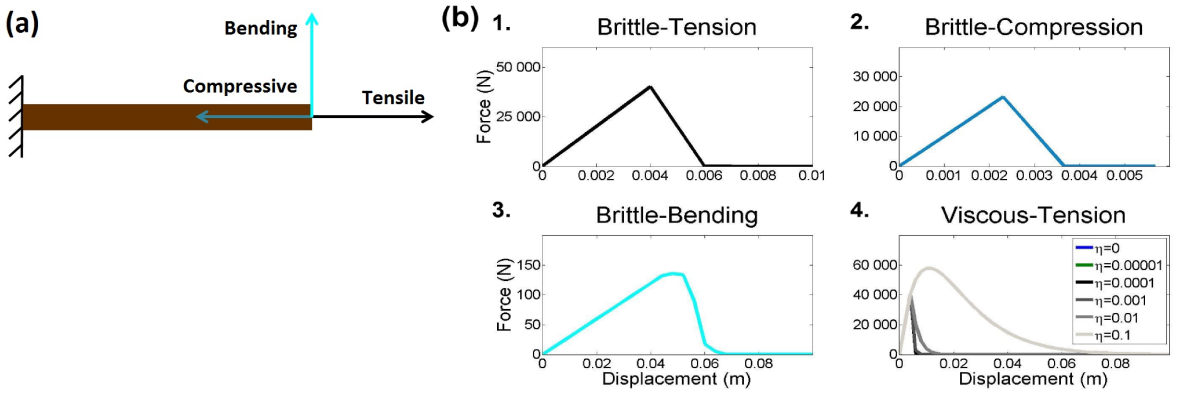

Figure 2.3 Numerical root failure behaviour tests and results. (a) A cantilever beam of wood material subjected to different displacements at the free end: tensile, compressive and bending tests. (b) Force–displacement curves predicted by simulations at the free end: 1. tensile test; 2. compressive test; 3. bending test; 4. tensile tests including viscous effect. η values are 0.0, 1.0e–5, 1.0e–4, 1.0e–3, 1.0e–2 and 1.0e–1).

height of 1.68 m. The winch was attached to the stem base of an anchor tree at a distance of 12 m from the pulled tree so that the pulling force can be considered horizontal with an error of 1%. The part of the tree above this height was cut off. The pulling force was measured by a load cell (SM 5420, 50 kN; Sensel, France) and the stem deflection angles on the top and at the base of the stem were measured by two inclinometers (SN: 25276; Sensel, France). The turning moment was calculated using the horizontal component of the pulling force.

Root architecture

Root system excavation, measurements and modelling were performed according to Danjon et al. (2005). On 15 May 2012 the soil surrounding the damaged root system was removed with a high-pressure soil pick (Soil Pick; MBW Inc., USA; http://www.mbw.com/products/Pick.aspx) and the root system was excavated with a large mechanical shovel. Roots thinner than 1 cm in basal diameter were removed before the measurements. Root breakages were marked and large root deformations corrected manually, in order to return as close as possible to the undamaged state of the root system. In the meantime, the root system was discretized by a Polhemus Fastrak low magnetic field digitizer (Polhemus, Colchester, VT, USA; http://www.polhemus.com) and encoded in a standard format (MTG) commonly used for representing branching topological relationships at different observation scales (Godin and Caraglio, 1998). The MTG file was then read by Xplo software and exported to the root anchorage model in a format readable by ABAQUS.

Item	Symbol	Value	Units
Density	ρ_s	1410	$kg.m^{-3}$
Modulus of elasticity	E_s	19.86	MPa
Poisson's ratio	ν	0.33	–
Cohesion	c	21.402	kPa
Friction angle	ϕ	14.62	°
Dilation angle	ψ	0	°

Table 2.1 Measurements of mechanical properties of soil material: elastic-plastic with the Mohr–Coulomb criterion

Soil mechanical properties

Around the pulled tree, soil was sampled at four locations in the main cardinal directions at three depths, i.e. 0–10 cm, 10–30 cm and 30–60 cm, just above water table level (at about 60 cm depth) to measure soil bulk density and water content and to collect material for the mechanical tests. Then, 12 sandy soil samples were reconstituted with an initial dry bulk density of 1410 $kg.m^{-3}$ and an initial gravimetric water content of 0.11 $g.g^{-1}$, both corresponding to the mean values measured in the field. Direct shear tests were conducted using a Wykeham Farrance shear testing machine to characterize soil mechanical properties. The soil material was assumed to be homogeneous and initially linear elastic (defined by modulus of elasticity E_s), combined with plastic behaviour modelled using the Mohr–Coulomb failure criterion available in the ABAQUS materials library (Table 2.1):

$$\tau_{max} = \sigma_n \tan\phi + c \tag{2.8}$$

where τ_{max} is soil shear strength, σ_n the normal pressure in the soil failure plane, ϕ the soil internal friction angle and c the soil cohesion (Bardet, 1997).

2.2.3 Simulation set-up

Simulations were performed to mimic the field experiment. The stem height at which the pulling force was applied was 1.68 m. The soil domain (dimensions = 8m x 8m x 4m) was meshed with 8-node linear brick elements with reduced integration (C3D8R in the ABAQUS element library), with the region containing the roots meshed into finer elements with an approximate edge size of 0.25 m. Symmetrical boundary conditions (XSYMM and YSYMM in ABAQUS Analysis User's Guide) were imposed on the four laterals of the soil domain so that these faces were blocked to constrain soil motions with respect to the planes considered (XZ and YZ). The boundary condition of fully built-in (ENCASTRE in ABAQUS Analysis User's

Guide) was defined for the bottom of the soil to block all six degrees of freedom in the plane XY. The root architecture measured was imported in ABAQUS as already explained. Loading was applied on the soil-root system in two steps: the gravity body force was applied first with the gravity constant $g = 9.81\ m.s^{-2}$, then a horizontal displacement of 1.2 m was imposed in the direction of the x axis at the top of the stem to ensure a maximum deflection angle of 45°. This displacement implies large deformations in the root-soil system which makes sure that maximum turning moment occurs largely before the end of the simulation. The reaction force and corresponding displacement at the top of the stem were recorded during the simulation. The force–displacement response curves were analysed by calculating the work done by the pulling force as the integral of pulling force F as a function of the maximum horizontal displacement, d_0, imposed on the top of the stem:

$$W(F,d_0) = \int_0^{d_0} F(x)dx \tag{2.9}$$

with x the horizontal displacement. The 3D anchorage model requires a set of root parameters, namely ρ_r (root density), E_r, σ_{11}^t, σ_{11}^t and G_f, to characterize root mechanical behaviour. The relationships among these parameters were developed using recent evidence found for stem wood of pine species and roots of *P. pinaster* reported in literature (Khuder et al., 2007; Kretschmann, 2010; Niklas and Spatz, 2010; Stokes and Mattheck, 1996; Stokes et al., 1997b). Ordinary Least Squares (OLS) and Reduced Major Axis (RMA) regression analyses showed the modulus of elasticity E_r was linearly correlated to root density ρ_r, tensile strength σ_{11}^t and compressive strength σ_{11}^c for the stem wood of more than 100 worldwide species (Niklas and Spatz, 2010). Data for green wood samples of 16 pine species (Kretschmann, 2010) were used to obtain these relationships (Table 2.2). ρ_r and E_r were found to decrease with increasing distance from the tree stem in the lateral roots of *P. pinaster* (Khuder et al., 2007); and the thick coarse root diameter was found to decrease with increasing distance from its base. Thus ρ_r and E_r were assumed to be positively linearly correlated to root diameter. E_r was fixed at 8 GPa for a root diameter of 3.5 cm in the first simulation SA1 (range taken from data source: (Khuder et al., 2007; Stokes et al., 1997b)). A linear variation in E_r from 7.2 GPa to 8.8 GPa was defined for SA1 for root diameters ranging from 1 cm to 6 cm (Figure 2.4). E_r for roots of diameter less than 1 cm and more than 6 cm was fixed at constant values equal to 7.2 GPa and 8.8 GPa, respectively (Figure 2.4). Then all the other mechanical parameters related to E_r were determined using relationships in Table 2.2. The fracture energy G_f was fixed at a value found in the literature (Dourado et al., 2008), i.e. 209.4 $J.m^{-2}$ for the stem wood of *P. pinaster* for all the simulation cases. To take into account variety in mechanical properties and variety in

Item	Correlation	Units	R^2
ρ_r	$38.942E_r + 109.91$	kgm^{-3}	0.6415
σ_{11}^t	$5.0698E_r + 2.6081$	MPa	0.5775
σ_{11}^c	$2.3692E_r + 1.6855$	MPa	0.6333

Table 2.2 Linear correlations between E_r (in GPa) and ρ_r, σ_{11}^t and σ_{11}^c for green wood of 16 pine species

relationships between mechanical and geometric properties (i.e. root diameter in our study), four other simulation cases were defined in the same way with: 1. different E_r central values for roots of 3.5 cm in diameter (9.2 GPa and 6.8 GPa in SA2 and SA3, respectively; Figure 2.4); 2. different variations in E_r for the range of root diameters [1 cm, 6 cm] ($\pm$ 20% and $\pm$ 0% with respect to the central value in SA4 and SA5, respectively; Figure 2.4). Two other

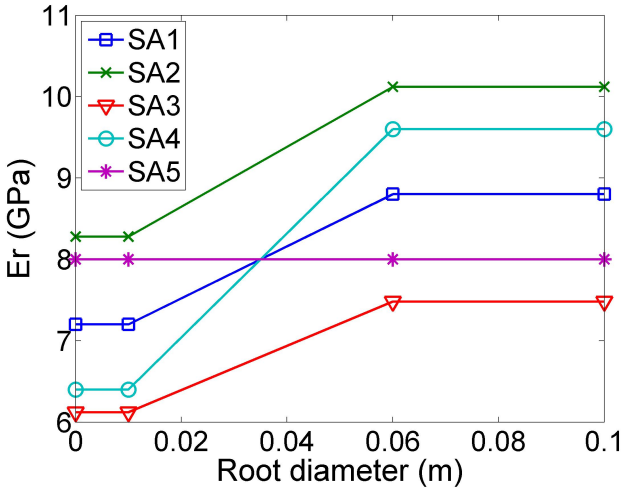

Figure 2.4 Linear relationships of modulus of elasticity of root material (E_r) versus root diameter applied to the entire root system for five simulation cases (SA1–SA5). More detailed information about parameter values in each case is presented in Table 2.3.

simulations, SA6 and SA7, without root failure behaviour were also performed in comparison with previous five simulations and the experiment. SA6 defines elastic behaviour with E_r of 8 GPa and Poisson ratio of 0.3 for all roots, and SA7 defines elastoplastic behaviour, with the same elastic behaviour as the previous and plastic threshold the same value of σ_{11}^t defined for SA5. All root mechanical parameters used in these simulations were summarized in Table 2.3.

Item	Units	Root diameter interval	SA1	SA2	SA3	SA4	SA5	SA6	SA7
		<1cm	7.2	8.3	6.1	6.4	8	8	8
E_r	GPa	1cm–6cm	7.2–8.8	8.3–10.1	6.1–7.5	6.4–9.6	8	8	8
		>6cm	8.8	10.1	7.5	9.6	8	8	8
		<1cm	379.3	421.4	337.2	337.2	421.4	421.4	421.4
ρ_r	kgm^{-3}	1cm–6cm	379.3–463.6	421.4–515.0	337.2–412.2	337.2–505.7	421.4	421.4	421.4
		>6cm	463.6	515	412.2	505.7	421.4	421.4	421.4
		<1cm	38.8	44.3	33.4	34.5	43.2		43.2
σ_{11}^{t}	MPa	1cm–6cm	38.8–47.5	44.3–54.1	33.4–40.8	34.5–51.8	43.2		43.2
		>6cm	47.5	54.1	40.8	51.8	43.2		43.2
		<1cm	18.6	21.1	16	16.5	20.6		
σ_{11}^{c}	MPa	1cm–6cm	18.6–22.7	21.1–25.8	16.0–19.6	16.5–24.8	20.6		
		>6cm	22.7	25.8	19.6	24.8	20.6		

Table 2.3 Root data sets for seven simulation cases (SA1–SA7) using the 3D anchorage model

2.3 Results

2.3.1 Moment–rotation response curves: simulations in comparison with the experiment

The response curves provided by the simulations with root breakage and the *in situ* tree–pulling test were compared, taking the deflection angle at the stem base. The simulated response curves exhibited typical behaviour for brittle material with root successive breakages (Figure 2.5). Large decreases in turning moment are due to root breakages whereas very small decreases are mainly due to numerical errors related to local algorithmic convergence difficulties. The simulations suggest that the contribution of roots to anchorage strength is strongly influenced by their mechanical properties. For example, the abrupt decrease in turning moment by 2130 N.m at 7.3° for simulation SA3, caused by the breakage of a thick counter-winchward lateral root, was delayed in cases SA1 and SA2 which had globally higher E_r, σ_{11}^t and σ_{11}^c. Both the cases with higher E_r, σ_{11}^t and σ_{11}^c in all roots (SA1 and SA2) and the case with higher E_r, σ_{11}^t and σ_{11}^c only in thicker roots (SA4) predicted greater anchorage strength (i.e. critical turning moment).

2.3.2 Moment–rotation response curves: root breakage in comparison with no root breakage

The response curves, i.e. the turning moment of the pulling force against the deflection angle at the stem base, obtained from two simulations (SA6 and SA7) without root breakage were compared with a representative simulation SA1 defining root breakage and the experiment (Figure 2.6). SA6 predicted a continuously growing turning moment within the considered interval of deflection angle. Therefore defining the critical turning moment for root anchorage strength would be inappropriate. The turning moment predicted by SA7 reached the global maximum at 27.5° in deflection angle, after which it decreased slightly and gradually. The slight decrease in turning moment is probably due to both the negative contribution of soil softening behaviour after plastic yielding and zero contribution of root after plastic yielding. Within the considered interval, SA1 predicted a response curve similar to that of the experiment in terms of magnitude of turning moment. SA6 and SA7 predicted visibly much higher values in turning moment with respect to SA1 and the experiment.

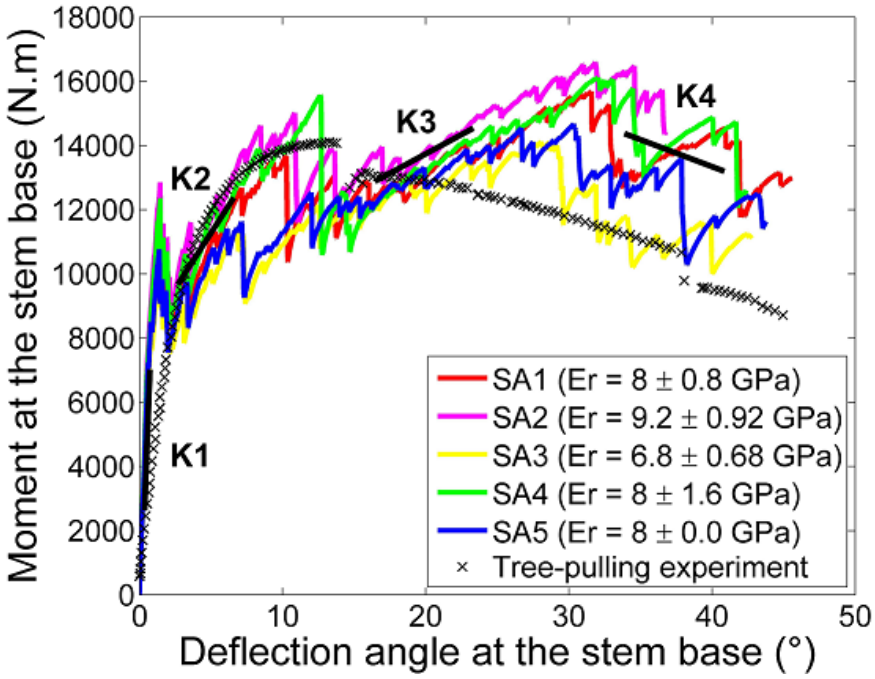

Figure 2.5 Comparison among five simulations (SA1–SA5) with different data sets of root mechanical parameters and the curve measured from the tree pulling experiment: turning moment of pulling force against deflection angle at the stem base. K1, K2, K3 and K4 are averaged system stiffnesses (slopes) at four intervals of deflection angle.

2.3.3 Moment-rotation response curves: the evolution of apparent stiffness of the root-soil system during tree-pulling process

Simulations including root breakages exhibited abrupt decreases in the moment-rotation response curves followed by increases. These local increases characterize the soil-root system strength that changes during the uprooting process. It can be quantified in terms of apparent stiffness of the root-soil system due to successive breakages and successive activation of new roots to sustain the loading. The trend of system stiffness degradation as a function of deflection angle is thus represented by progressively decreased apparent slopes (i.e. K1, K2, K3 and K4) within four intervals of deflection angle. To determine K1, K2, K3 and K4, we proceeded as follows: 1. for each of the five simulation curves, we first identified four successive intervals with an apparent slope to be determined for each of them; 2. the apparent slope within each interval of the simulation was determined by the linear regression; 3. then each Ki was calculated for the interval i as the mean value of apparent slopes from five simulation cases. For all the simulations, the first recovery of the turning moment characterised by K2 gave rise to a local maximum turning moment at about 10°. This interval matched the deflection

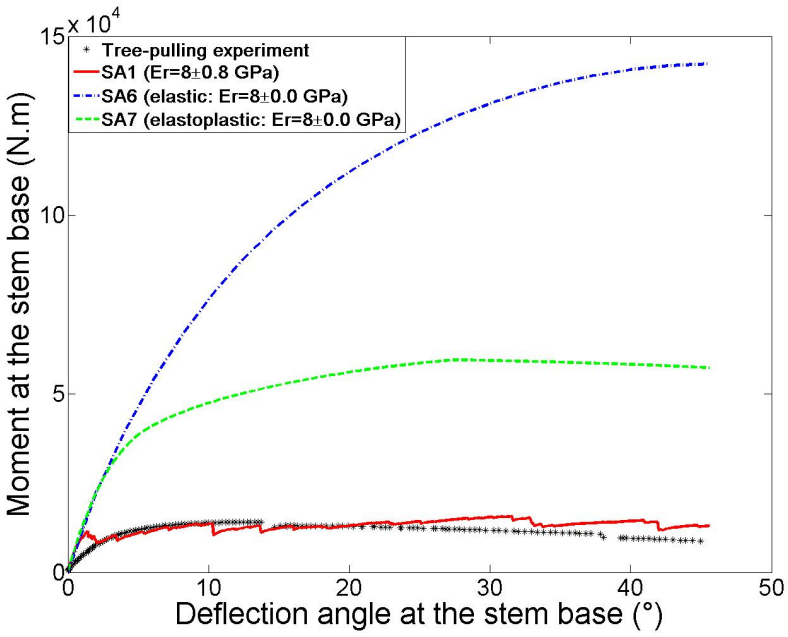

Figure 2.6 Comparison among the two simulations without root breakage (SA6 and SA7), simulation SA1, including root breakage, and the experiment: turning moment of pulling force against deflection angle at the stem base.

angle at which the critical turning moment occurred in the experiment (14°). However, the second recovery of turning moment characterised by K3 gave rise to the global maximum at about 30°, slightly higher than the previous one. Compared with the simulation curves, the curve from the experiment is much smoother, being cut into three parts marked by two abrupt decreases in turning moment, at 14° and 38° respectively. The recover after the peak value is small enough to be neglected. Taking the global peak as the critical turning moment, the simulations from SA1 to SA5 overestimated anchorage strength by up to 17.8%. Another main difference between the measured and simulated response curves is the initial stiffness behaviour. First of all, the initial stiffness estimated by all simulations was higher than the measured value. Secondly, the measured stiffness gradually decreased, as characterized by the smoothness of the curve, whereas in the simulations the decreases in initial stiffness due to root breakages were abrupt and without transition.

2.3.4 Energy induced by the pulling force: simulations in comparison with the experiment

The fundamentals of continuum damage mechanics have related numerous energy–based concepts and approaches to the failure behaviour of materials (Krajcinovic, 1996; Murakami,

2012). Simulations were analysed using the stored energy of the root–soil system induced by the pulling force. Figure 2.7 shows the evolution of energy induced by the pulling force as a function of the horizontal displacement at the pulling point during the tree–pulling process, for the simulations SA1 to SA5 and the experiment. The energy calculated by all the simulations was in good agreement with that of the experiment. As mentioned above for the response curves in Figure 2.7, at initial loading stage (horizontal displacement of pulling point ranging from 0 to 0.2 m) the root–soil system in all the simulations was stiffer than that of the experiment. Therefore the predicted energy was initially higher in all the simulations.

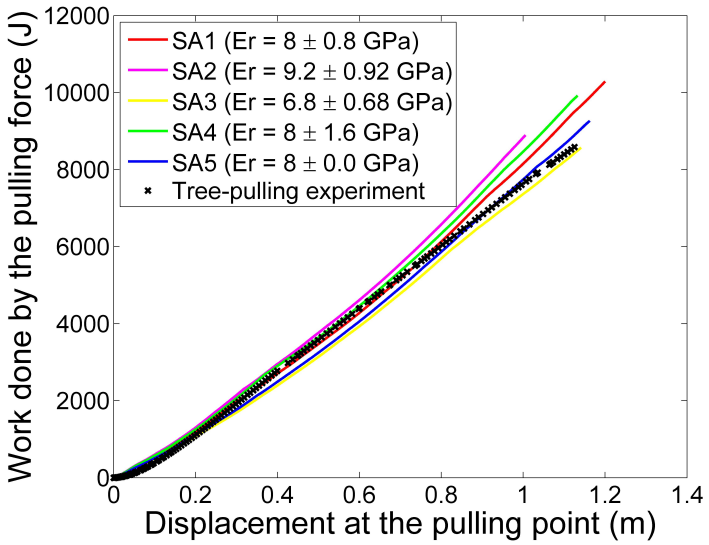

Figure 2.7 Evolution of the work done by the pulling force during the tree-pulling process predicted bysimulations(SA1–SA5) compared with that measured in the tree-pulling experiment.

2.3.5 Linking root successive breakage to tree mechanical response to overturning

Our model can now be used to examine the successive root breakage during the uprooting process. The set of five figures in Figure 2.8 illustrates how broken roots can be detected and the connection between successive root breakage and the mechanical effect on root anchorage strength. The response curve shows the turning moment calculated at the stem base versus the deflection angle at the stem base (Figure 2.8 (a)). The first square mark on the curve is linked to Figure 2.8 (b)-1 which shows the state of the intact root system just before the first root breakage. The uniform greenish blue colour in the root system indicates zero-value of damage variable d (SDV1 in the legend), meaning no damage has occurred. The second square mark on the curve is linked to the state of the root system showed by Figure 2.8 (b)-2. Figure

2.8 (b)-2 shows the moment after the successive breakage of three finer intermediate roots smaller than 2.5 cm in basal diameter, a lateral root of 5.5 cm in basal diameter and a thick chuck-like oblique root of 8.7 cm in basal diameter. Broken root segments are represented in red in Figure 2.8 (b)-2. These broken roots reduce the turning moment by 1905 N.m. The third square mark corresponds to the moment just before the breakage of a thick lateral root in the counter-winchward direction (the root marked by a circle in Figure 2.8 (b)-3), and the fourth square mark to the moment immediately after the root breakage (the damaged root zone circled in Figure 2.8 (b)-4). The breakage of this thick lateral root alone leads to a sudden drop in turning moment by 2130 N.m. After each drop in turning moment caused by root breakage, the redistribution of stresses released by the broken root(s) to the other roots leads to another recovery of the turning moment. The root breakage tendency (i.e. root types and locations) predicted by our model was compared to field observations during root system excavation. Field observations showed a large number of relatively finer roots, a large shallow root in the counter-winchward direction and a shallow root in the sector perpendicular to the winchward direction had broken. In particular, the damage in the thick shallow root in the counter-winchward direction was initiated very close to the stump, cracking along a large segment. Detailed root damage state in Figure 2.8 (b)-4 shows our model predicts qualitatively fairly well the observed root breakage tendency: the same shallow root in the counter-winchward direction was also broken close to the stump, and many small size roots were broken.

2.4 Discussion

Our strategy for developing the model was to provide a model with the same degree of physical realism for the three main components: (i) root architecture (ii) root mechanical strength and (iii) soil strength. As previous numerical works focused on root architecture (Dupuy et al., 2005b; Fourcaud et al., 2008), this new model was developed to integrate a more realistic description of individual root behaviour. A constitutive law for root mechanical rupture was developed to describe root failure under tension, bending and compression. Using data from the literature, we established a specific parameterization for root mechanical properties and their variation as a function of root dimensions. This method led to simulating the successive breakage of roots during uprooting, something which had not been done before. Also, the simulated tree-response curve obtained without any calibration was in good agreement with our observations. The following section is devoted to examining these results, and assessing the potential of this new model and its limitations.

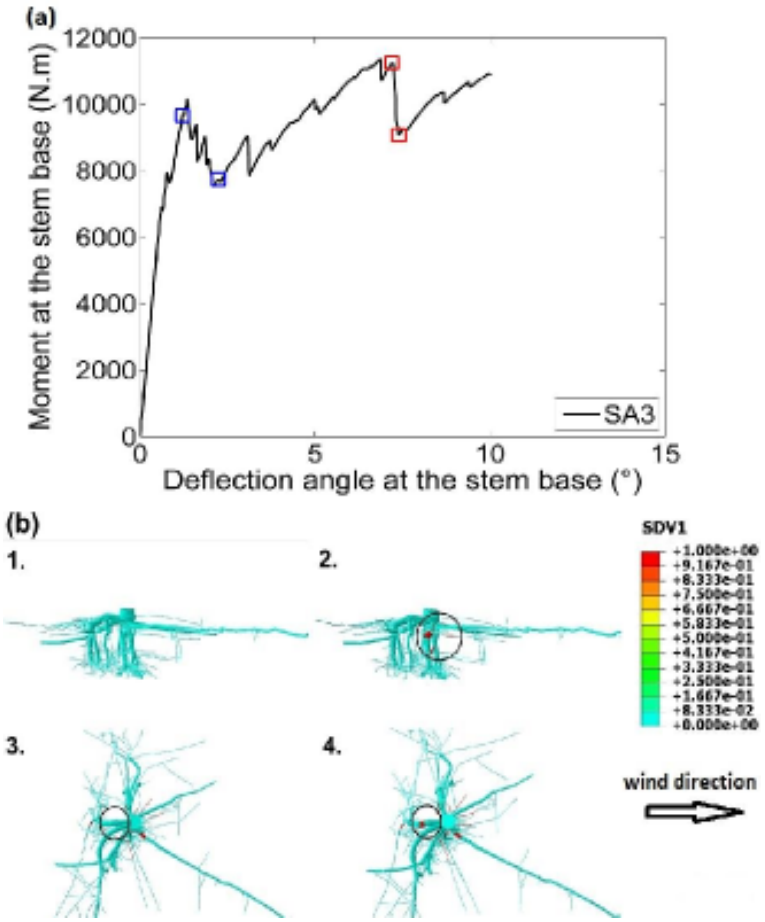

Figure 2.8 Linking successive root breakage effects to tree overturn response. (a) Turning moment of pulling force against deflection angle at the stem base (SA3) with four squares marking breakage points. (b) Root damage state (SDV1) in the root system at four moments corresponding to square marks on the curve in (a): (1) intact state of the root system related to the first blue square; (2) after several root breakages, marked by a black circle related to the second blue square; (3) state of root damage before breakage of a thick counter-winchward root occurs, marked by a black circle, related to the first red square; (4) state of root after breakage of a thick counterwinchward root occurs, marked by a black circle, related to the second red square.

2.4.1 Initial root-soil stiffness

The initial stiffness of the root-soil system was not properly estimated by the model. Whereas it is expected to be important to accurately estimate the tree inclination in addition to the trunk bending under the wind. In particular, for uprooting risk the initial stiffness should be required to estimate the moment applied to the crown due to wind and gravity and compare to the critical turning moment. Moreover it could be valuable when considering damage with tree inclination after a wind storm without uprooting or breakage, i.e. toppling, usually reported

for young trees (Moore and Maguire, 2008), or when considering the wind's interaction with trees for landscape-scale problems (Gardiner et al., 2000). In the latter case, it is common to model the root-soil system without flexibility due to a lack of quantitative information, despite the fact that including flexibility improves prediction (Jonsson et al., 2006; Neild and Wood, 1999). The present model overestimates the initial stiffness of the root–soil system. First of all, a sensitivity analysis was performed in order to identify the model parameters responsible for this discrepancy between the simulations and the observations. Four mechanical parameters of roots and soil were selected for this sensitivity analysis. The purpose was to quantify their separate influences on the initial behaviour of the root–soil system characterized by the initial slope of the force–angle response curve. Root tensile strength σ_{11}^t, compressive strength σ_{11}^c and fracture energy G_f were not selected in this analysis, because these parameters are involved during calculations only if root breakage occurs. However, according to the simulation results no root breakage was detected during the early loading stage considered. For all cases the initial stiffness of the root–soil system was calculated as the slope of the response curve for the reaction force ranging from 0 N to 4 kN (Figure 2.9). The initial stiffness is supposed to be calculated within the material elastic state of the system. However in the case of soil cohesion variation of -50%, soil zone surrounding the root system was yielding when the reaction force reached 4 kN (blue curve, Figure 2.9). Then the initial stiffness was revaluated just before first yielding zone appeared in the soil for this case (green curve, Figure 2.9). The initial slope of force–angle response curve is mainly influenced by the modulus of elasticity of the root and soil materials. A variation of $\pm$50% in the modulus of elasticity of the roots leads to a variation in the initial slope of –37.5% and +32.1%, positively related to the input variation. The same variation in the modulus of elasticity of the soil leads to a variation in the initial slope from –19.0% to +8.3%. Soil cohesion and friction angle are not influential factors as long as the overall soil state remains elastic at the early loading stage considered. For the case of a 50% decrease in soil cohesion, when the pulling force reached about 4kN, the plastic yielding occurred in a zone about 60 cm in size (including the stump) in the soil domain. The first evaluation of initial stiffness in the force interval [0, 4kN] gives a decrease of 19.2% in initial stiffness (blue circle in the third column of Figure 2.9). The fact that the yielding area appears on the soil surface at a very early loading stage in this case can be explained by the lower soil shear strength resulting from the reduced soil cohesion, according to the Mohr–Coulomb equation. Then, the revaluation of initial stiffness was computed in the interval ranging from the soil initial state to the soil elastic state just before yielding. The result shows that the slight variation of 1.3% is due to a decrease in soil cohesion by 50% (green circle in the third column of Figure 2.9). Finally the sensitivity analysis indicates that the overestimate of initial root–soil stiffness is due to the overestimation of input elastic data, namely E_r and E_s. Thus the accurate

estimation of root-soil stiffness probably required a good estimation of the elastic modulus for both soil and root. Then the overestimation is probably due to the lack of data on root mechanical properties. Furthermore, Young's modulus of roots at early loading stage was found to be lower than average values due to their initial tortuosity; and after stretching roots become stiffer, exhibiting average root material stiffness (Commandeur and Pyles, 1991). In the model, the Young's modulus was defined to be constant with respect to root geometry change during the course of tree-pulling, which may potentially lead to the overestimation of initial stiffness. This new insight for root-soil stiffness illustrates the potential of the present mechanistic model for further application, such as tree-wind interaction for landscape-scale problems for which root-soil flexibility remains poorly described (Jonsson et al., 2006; Szoradova et al., 2013).

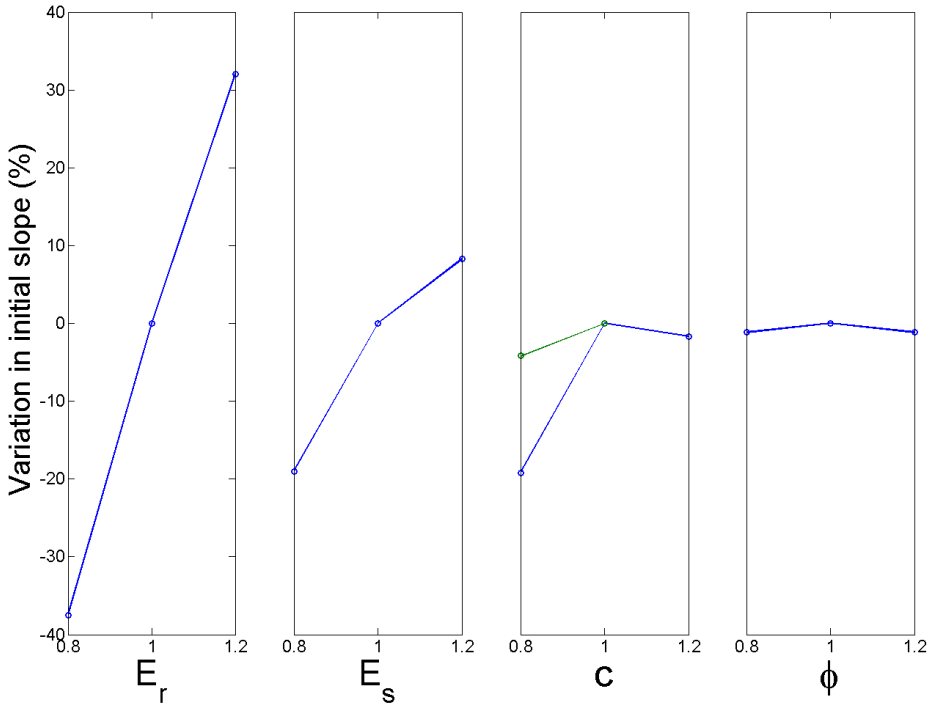

Figure 2.9 Sensitivity analysis of the initial slope of the response curves: initial slope variation versus ±50% variation in modulus of elasticity of roots (E_r), modulus of elasticity of soil (E_s), soil cohesion (c) and soil friction angle (ϕ). The initial stiffness of the root–soil systemwas evaluated twice for the case of a –50% decrease in soil cohesion (c), with the second evaluation marked by a green circle.

2.4.2 Modelling root failure

The relevance of this new model lies essentially in the improvement obtained in modelling root-soil failure. This gives a more realistic description of every important aspect of the first mechanistic model of root anchorage (Blackwell et al., 1990). For the first time we have produced a model that simulates root ruptures realistically, by combining a constitutive law for rupture in composite materials and mechanical parameters for wood available in the literature. Our constitutive law accounted for root brittle failure behaviour under tension, compression and bending. We demonstrated through a simulation case that the numerous drops in pulling force moment–angle curves were directly linked to successive root breakages. This type of moment-rotation behaviour with successive drops has been reported in previous field investigations on tree–pulling tests (Cucchi, 2004). In addition, the signature of root breakages during uprooting was also reported by Coutts (1983) who measured the sound made by successive root breakages by microphones. This behaviour with successive ruptures was also observed in studies performed to prevent soil erosion by using roots to increase slope stability. This cumulative rupture was reported for numerous field pull–out tests using fine root bundles and this trend could be reproduced in several models adapted from the fibre bundle model (Pollen et al., 2004; Riestenberg, 1994; Schwarz et al., 2012, 2013). In these cases, the problem was to evaluate the contribution of fine roots to soil reinforcement, so only the tensile failure of roots was accounted for, and root diameter was generally less than 1cm. In our case, the tree uprooting process involves coarse roots under tension, compression and bending failing progressively, which requires a model dedicated to uprooting.

Compared to previous tree anchorage models, our model is able to provide more realistic response curves with respect to the experiment and predicted a peak value of turning moment which defined properly the critical turning moment (Dupuy et al., 2005b, 2007; Rahardjo et al., 2009). Our results gave fairly accurate descriptions of the behaviour of the root–soil system during tree overturning. Despite the simplifications introduced for root–soil interaction and root material, the estimated critical turning moment was reasonably correct and close to that measured in the experiment. In addition to this first quantitative validation, this new model seems robust in terms of the physics simulated. We evaluated the energy induced by the pulling force throughout the process: all the simulations were in good agreement with the experiment. This validation in terms of energy is important because a good agreement in terms of energy is an indicator of well simulated physical process. Moreover, our damage model is derived from continuum damage mechanics for which energy estimation is an important aspect of model evaluation (Murakami, 2012). A more in-depth analysis of this aspect of the model would require better simulation of the rupture behaviour of individual roots. At this stage,

the constitutive law for root rupture is based on the literature and has not been validated by comparison to mechanical tests on individual roots.

Whereas the model appears to estimate the critical turning moment well, it differs from the observations when considering post-rupture behaviour. The simulations exhibited moment-rotation curves that increased after the first stage of the ruptures, contrary to the experimental curve. First from a physics point of view, if larger and stiffer roots take the role of other roots which carried the loads before their breakage, the recovery contributed by these roots can be much more significant than the ones with lower stiffness (i.e. lower E_r or smaller diameter). Our simulations defined higher E_r values from the wide range for coarse roots, which could potentially lead to a more significant recovery in turning moment. In addition, this discrepancy could also partially be explained by certain numerical prerequisites. Indeed, the root slippage caused by large deformations of the root-soil system was constrained by the root-soil interaction method, namely the embedded element method. Thus potential errors could arise due to the fact that no possible failure occurs at the root-soil interface. Recent developments in understanding soil reinforcement by fine roots permits modelling root–soil interactions more accurately by incorporate friction laws for root-soil interaction (Pollen, 2007; Schwarz et al., 2012, 2013). However friction laws prove to be expensive in terms of computational cost due to complex geometries and interactions in our model. Such a high level of complexity is probably not required in the near future because the "embedded element" method turned out to be a good compromise between accuracy and computational cost (see results in Appendix of Annexe A).

2.4.3 Root mechanical properties

One significant result of this study concerns the role of the mechanical strength of roots. By linking the global root-soil system response characterized by the response curve to local root breakages detected by visualization, we are able to detect broken roots at a given moment. The root breakage pattern due to tree-pulling was fairly well imitated, which allowed us to use the model as a "diagnostic tool" to explain the mechanical role played by main root components. The results show that root thickness and root location may strongly influence the contribution of tree response to overturning. Thick counter-winchward lateral roots contribute more significantly to anchorage strength in comparison to relatively fine lateral and intermediate roots. Furthermore, thick counter-winchward lateral roots contribute more than thick oblique roots. For the first time, we highlighted the role played by mechanical properties of roots in tree response to overturning, as previously suggested by Coutts (1983). In our study, we find that both higher root mechanical strength with higher E_r in all roots and higher strength with higher E_r only in thicker roots, provide better root anchorage, which is reasonably correct. But we had to simplify certain root mechanical properties due to the lack of data on root material. Firstly,

relationships among the material properties of coarse roots were assumed to be similar to stem wood. Thus the correlations established between E_r and the other three parameters, ρ_r, σ_{11}^t and σ_{11}^c, for stem wood applied to roots. However, it is generally believed that root mechanical properties differ from those of stem wood and vary enormously depending on root age, tree species, root physical properties such as cellulose content, water content, etc. (Genet et al., 2005). For example, the tensile strength measured for coarse roots may range from 9 MPa to 63 MPa (Coutts, 1983). For the same species of *P. pinaster*, the longitudinal modulus of elasticity measured may vary from 0.8 GPa to 11 GPa (Khuder et al., 2007; Stokes et al., 1997b). The data sets built in all our simulations always took higher values of E_r in the range [0.8 GPa, 11 GPa], which may lead to estimation errors on all the other parameters related to E_r. Furthermore, our sensitivity analysis has proved potentially overestimated E_r led to overestimated initial stiffness of the root-soil system. Secondly, relationships between root mechanical properties and root diameter were assumed to be positive linear, based on similar descriptive findings for coarse roots (Khuder et al., 2007; Stokes and Mattheck, 1996). This may have caused estimation errors on root anchorage strength. Moreover, another mechanical parameter G_f remained constant for all the simulation cases. This may have led to errors in characterizing root failure behaviour. Finally, we formulated a damage model with an assumption of brittle material for roots. However, load-displacement curves from fracture tests on single-edge-notched beams showed wood in compression exhibited less abrupt post-rupture behaviour than that predicted by our model (Dourado et al., 2008). In conclusion, more experiment results will be needed to improve and validate the damage model for roots.

2.4.4 Soil mechanical properties

This new model was tested using a set of measured soil properties corresponding to the soil conditions of the tree-pulling tests. This represents a significant improvement because previous modelling approaches either didn't consider soil material properties or used only literature findings to model general soil mechanical behaviour (Blackwell et al., 1990; Dupuy et al., 2005b; Rahardjo et al., 2009). However the role of soil compartment remains poorly described and is treated as homogeneous media so that improvements are required in the future to evaluate its impact on tree anchorage. The presence of a water table, rocks, hardpan and organic matter (dead leaves and stumps, roots, soil surface vegetation etc.) modifies the soil, making it much more porous and far from homogeneous material as considered here. In particular, numerous studies confirmed the local presence of fine roots can improve local soil shear strength by providing additional cohesion to the soil (Mao et al., 2012b; Pollen and Simon, 2005; Schwarz et al., 2010; Waldron, 1977; Waldron and Dakessian, 1981; Wu et al., 1979). The present model

could be used to investigate the influence of forest soil properties and its spatial variation on tree stability.

2.5 Conclusion

This paper presents a new model of tree anchorage capable of simulating root breakages for the first time. It also permits the localisation of damage within the root system and includes specific parameterization for root and soil properties based on measurements and experimental evidence reported in the literature. These simulations were performed without any calibration and were found to be in good agreement with the observations. The results are promising enough to envisage further applications to adult trees which are more vulnerable to uprooting than young specimens. However, the architecture of the root system of adult trees is different from that of young trees for *P. pinaster*. This could increase the degree of complexity of the model. For example, the formation of a rigid "cage" within a root system is common for older *P. pinaster* (Danjon et al., 2005). Thus relevant adaptions for more complex root structures should be made in the model in the future. Nevertheless, our model proved useful for examining the role of root mechanical properties and thus it represents a significant step forward in better understanding of the uprooting process as a function of tree characteristics and soil mechanical properties. Mechanical consequences can also be analysed as a function of certain root system asymmetry (for example, leeward chuck-like structure) or other specific root features (for example, sections of large shallow roots formed in "I" or oval beam type close to the stump). Therefore the model could help understand how trees "optimise" the allocation of root material. This is particularly important for our comprehension of tree anchorage. The model is also expected to provide useful information on the underground response of trees to uprooting during storms for landscape wind risk models in the future. In particular, by studying the influence of variations in soil material properties on tree overturning behaviour, the model is expected to help us understand the impact of soil management on rooting (cultivation, iron pans, high water tables, indurations, soil saturation).

2.6 Acknowledgements

This work was supported by the project FAST-A of Aquitaine Region, the project TWIST of the JCC Program of the French National Research Agency and the project ForWind (Ref. ANR-12-AGRO-0007) of the French National Research Agency. We thank Jean-Marc Bonnefond, Didier Garrigou and Pierre Trichet for their help in the tree-pulling experiments and soil property measurements; Antoine Danquechin Dorval and Raphael Segura for the root architecture

measurements; Sébastien Griffon and Hervé Rey for their help in using Xplo software; Mark Irvine for his technical support for the ABAQUS computations; and Dr Sylvain Dupont for fruitful discussions on numerical modelling and his critical reading of our manuscript.We are also deeply grateful to two reviewers for their valuable remarks and suggestions, which offered new insights in this work. AMAP (Botany and Computational Plant Architecture; http://amap.cirad.fr/) is a joint research unit including CIRAD (UMR51), CNRS (UMR5120), INRA (UMR931), IRD (2M123) and Montpellier 2 University (UM27).

Chapter 3

To what extent does root morphological plasticity explain the variability in Maritime pine stability?

Oral presentation

Ming Yang, Pauline Défossez, Frédéric Danjon, Thierry Fourcaud. Understanding tree root anchorage with the finite element method: a focus on the impact of root system morphology. In *IUFRO 2014 Wind and Trees International Conference*, 2014b

Publication in preparation

Ming Yang, Pauline Défossez, Frédéric Danjon, Thierry Fourcaud. To what extent does root morphological plasticity explain the variability in Maritime pine stability?

Summary

Understanding the processes that underlie the variability in tree stability to wind is of primary importance as windstorms are the major natural hazard affecting European forests. The ability of a tree to resist winds depends on its anchorage within the soil which relies on the root system morphology. Root system morphology varies with phenotypic plasticity in response to the environment.

In this research, we used a biomechanical model based on the Finite Element Method to understand how this variability in root system morphology impacted tree anchorage behaviour and its mechanical resistance to overturning. *Pinus pinaster* was chosen as a model species. To accurately capture the variability in root architecture, we developed virtual root patterns based on extensive measurements of root system architecture of mature specimens.

The biomechanical model demonstrated the contributions of the root components to tree anchorage. It suggested a classification of their mechanical importance as follows: taproot > windward shallow roots > perpendicular shallow roots > windward sinker roots > any other component with less than 5% in terms of contribution to anchorage strength.

The research hypothesized and demonstrated the importance of root system morphology for tree anchorage, and quantitatively showed how it explained the variability in anchorage strength.

Key words: components of root anchorage, Finite Element Method, *Pinus pinaster*, root system architecture, tree stability

3.1 Introduction

Tree root anchorage provides tree stability under wind loading. The function of tree anchorage together with water and nutrient acquisition form the main functions of roots to guarantee tree survival. The ability of plants to enhance their root functional traits facing various environmental conditions is a prime example of the phenotypic plasticity (see reviews in Bradshaw and Holzapfel (2006); Sultan (2000)). There have been a number of reports of wind-induced plasticity phenomena in trees: from cellular scale to plant organs scale (Braam, 2005; Moulia, 2013; Telewski, 2006). This includes changes in both physiological and morphological traits. This wind-induced plasticity has observed for roots of trees which adopt different strategies to optimize their mechanical anchorage. It may concern the rooting pattern itself. For instance, tap-root systems of *Pinus pinaster* represents a typical rooting pattern with selective windward or leeward reinforcement in root volume (Danjon et al., 2005). This has been also reported for root systems developing in slopes where tree allocate more volume to upslope lateral roots (Danjon et al., 2013b). But this plasticity may also involve localized reinforcement of root wood with higher mechanical strength (Stokes and Mattheck, 1996) and adaptive growth of root cross-sections in the form of oval, I- or T-shaped beams in the windward and leeward sectors (Coutts et al., 1999; Nicoll and Ray, 1996).

One of the consequences of the phenotypic plasticity of roots is that root morphological features are highly variable (Danjon et al., 2013b; Lynch and Brown, 2001). With progress in 3D digitising techniques for plant architecture (Godin et al., 1999; Ristova et al., 2013; Sinoquet and Rivet, 1997), there is now tree root architectural data available to explicitly represent the large variability in root system morphology which expresses the different strategies taken by the tree to fit environmental stresses (see in review (Danjon and Reubens, 2008)). While there is strong evidence that these morphological variability lead to variations in plant anchorage capacity (Coutts, 1983; Coutts and Lewis, 1983), this remains poorly documented and quantified. The complex and opaque soil medium restrains these processes from being easily measured or manipulated. Following the pioneer works on tree anchorage (Coutts, 1983, 1986; Coutts and Lewis, 1983), understanding the tree anchorage progressed with the use of the finite element method (FEM) to calculate the deformation of root-soil systems (Dupuy et al., 2005a,b; Fourcaud et al., 2008). This numerical approach provides a useful tool to examine the mechanics of the root system as function of the root architecture, the mechanical strength of roots and the mechanical strength of soil. But until now, the question of the role of root architecture was mainly addressed from a theoretical point of view to understand better how root branching and root patterns could relate to tree anchorage capacity (Dupuy et al., 2005b; Fourcaud et al., 2008). Our aim is to present additional modelling work closely associated to experiments in order to better capture the natural variability in root architecture of trees. Our

approach is in the line of developments of plant architectural modelling to link tree structure to its primary functions for comprehensive mechanisms of tree development and evolution (see review in (Barthélémy and Caraglio, 2007)). This has been applied for water, nutrient (Lynch, 2011) and biomechanical performance (Fournier, 1993; James et al., 2006; Sellier et al., 2006). But root biomechanics and mechanobiology remains poorly examined.

Our objective is to examine the tree stability resulting from different root morphological features taken by the tree for adaptive reasons and the role played by different main root components. Mature *P. pinaster* was selected as a model species because of the abundance of root architectural data for *P. pinaster* with progress in 3D digitising techniques (Danjon et al., 2005, 2013a) but the methodology proposed in this paper is relevant to many species sensitive to wind damage. The tree stability is estimated using an FEM anchorage model developed to simulate the tree uprooting (Figure 3.1). The parameterization of for the basic model processes was presented and discussed in Yang et al. (2014a) and the whole model was validated against various sets of data from different species (Dupuy et al., 2007; Yang et al., 2014a). Here we examine the stability of different root patterns which mimic existing natural morphological variations of root systems observed for *P. pinaster* to analyse the biomechanical behaviour of root system as function of morphological traits, quantify the contribution of each main root component and infer the impact of morphological variability on tree stability.

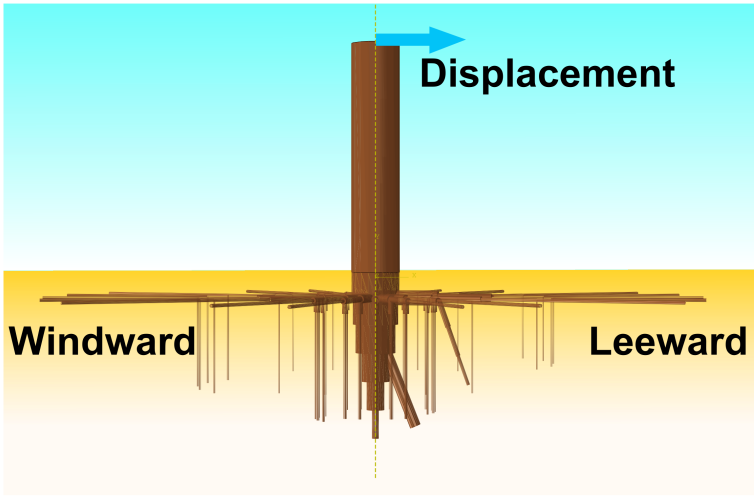

Figure 3.1 Tree-pulling simulation mimicking the tree uprooting process during wind storms. The wind action on the tree stem was modelled by a horizontal displacement. The root system was modelled by a virtual root pattern (MRA0 in Tables 3.1, 3.2, 3.3 and 3.4) with measured morphological features of mature *P. pinaster*

3.2 Materials and Methods

3.2.1 Building a virtual root pattern and its morphological variations

To gain an understanding of the plasticity of tree architecture, we developed a methodology to generate different virtual root patterns to be integrated in the biomechanical model for tree anchorage (Figure 3.2). A reference root pattern is designed based on experimental data to represent the main architectural characteristics observed for mature *P. pinaster*, then different morphological cases are derived representing for each case the loss of one root component (i.e. taproot, windward shallow roots, etc.) to represent natural variability. This methodology is based on a typology proposed by Danjon et al. (2005) to describe the root architecture of mature *P. pinaster*. This typology divides the root system into four sectors across two zones. The four sectors are defined by the prevailing wind direction: leeward, windward and perpendicular to wind direction. The two zones are defined by the root taper, a zone of rapid taper (ZRT) and a zone outside the ZRT (Figures 3.1 and 3.2). Besides the different root classes are considered: the root stump, the taproot, shallow roots in the ZRT, shallow roots beyond the ZRT, sinker roots extending from the first-order root or from the ZRT of shallow roots, sinker roots extending from the shallow roots beyond the ZRT, intermediate-depth horizontal roots, oblique roots and deep roots. In particular, root systems of mature *P. pinaster* are generally characterised by a large leeward shallow root carrying a large vertical or oblique third-order root named the “chuck”.

A first reference root pattern, MRA0 is designed, from which, 12 other configurations (MRA1 to MRA12) are built including the absence of specified root type(s) or compartment(s) as commonly reported (Crook and Ennos, 1996). Here, the reference root pattern MRA0 is parameterized using the measurements of *P. pinaster* root architectures reported in Danjon et al. (2013a). These measurements were done on seven individuals aged 19 with a mean DBH of 28.45 cm. Trees were cultivated at site L19 located in the southwest of France (44°42’ N, 0°46’ W) in a sandy podosol with a discontinuous hard pan at about 70 cm depth and a water table close to the soil surface during the winter. The root architecture was digitized so that each root was divided in 15 cm long segments with recording of direction, dimensions and branching points. The root diameters r_1 and r_2 were measured at two ends of each root segment. Further details can be found in Danjon et al. (2013a). The following assumptions were made to generate the reference root pattern MRA0: (i) all roots were assumed to be straight beam structures of circular cross-sections without forks or root grafts; (ii) each root segment volume equals the measured root volume of the corresponding measured segment. The radius for each

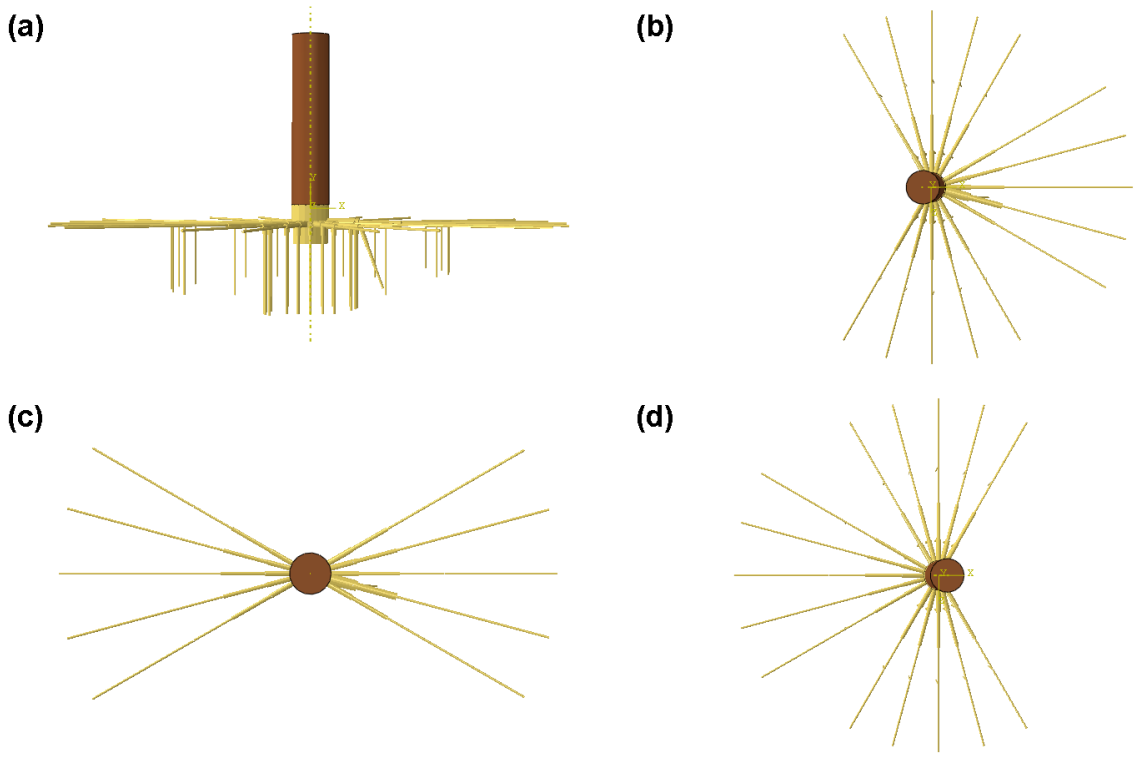

Figure 3.2 Four examples of morphological variations for the root pattern of *P. pinaster*: (a) the root pattern without a taproot; (b) the root pattern without windward roots; (c) the root pattern without roots in the sectors perpendicular to the prevailing wind direction; (d) the root pattern without leeward roots.

cylindrical segment is calculated from:

$$r = \sqrt{\frac{1}{3}(\bar{r_1}^2 + \bar{r_1}\bar{r_2} + \bar{r_2}^2)} \tag{3.1}$$

where $\bar{r_1}$ and $\bar{r_2}$ are the mean radius of respectively the larger base and the smaller base of the two ends of the corresponding measured segment. (iii) root taper was only considered within the ZRT of the root system: it was modelled by a chain of linked cylindrical segments tapering off in diameter. Beyond the ZRT all root segments were cylindrical; (iv) sinker roots extending from the first-order root were unified as one cylindrical second order sinker root; (v) all shallow roots were assumed to be horizontal; and the taproot and sinker roots extending from shallow roots were assumed to be vertical; (vi) intermediate-depth horizontal roots, oblique roots and deep roots were not considered. A detailed description of root pattern dimensions for MRA0 is given in Tables 3.1, 3.2, 3.3 and 3.4.

Items of root dimensions (Central part)	Model Value based on L19	Bilos Undamaged Value	Bilos Uprooted Value	Bilos Undamaged Range	Bilos Uprooted Range
Length (radius) of the ZRT	87.031	108.527	113.442	85.685-131.613	91.358-167.446
Basal diameter of the stump	35.054	46.636	45.418	34.41-57.13	31.17-53.99
Distal diameter of the stump	33.220	24.130	24.962	9.466-32.86	14.07-48.74
Depth of the stump	-33.0	-39.055	-42.323	-27.15, -46.24	-34.07, -49.58
Basal diameter of the taproot	29.218	24.130	24.962	9.466-32.86	14.07-48.74
Distal diameter of the taproot	5.110	2.196	1.558	0.1-10.1	0.1-8.864
Depth of the taproot	-112.779	-104.175	-105.709	-89.3, -127.3	-85.84, -134.7
Basal diameter of the 2nd order sinker	8.088	9.131	8.917	2-16.46	3.795-17.41
Angle between the axis of the 2nd order sinker and the vertical plan perpendicular to the pulling direction (°)	22.477	16.418	17.911	8.66-26.030	9.639-26.076
Length of the 2nd order sinker	76.807	60.342	64.31	13.94-130.7	31.18-102.2

Table 3.1 Main architectural characteristics of the root pattern MRA0 compared to 24 trees from the Bilos dataset (12 uprooted and 12 undamaged of similar size after the windstorm in 1999); (a) the central part. Note that root diameter and length are in cm, and most root diameters for Bilos are quadratic mean values because for each root section two diameters (major axis and minor axis) are measured.

Items of root dimensions (Windward)	Model Value based on L19	Bilos Undamaged Value	Bilos Uprooted Value	Bilos Undamaged Range	Bilos Uprooted Range
Number of windward shallow roots	5	5	4	3-7	0-9
Basal diameter of windward shallow roots	4.822	10.73	10.810	6.777-17.27	1.6-21.91
Diameter at the end of the ZRT of windward shallow roots	3.721	4.866	4.260	2.956-8.225	0.426-6.163
Diameter of windward shallow roots beyond the ZRT	2.198	1.965	1.460	0.875-3.554	0.4-3.148
Length of windward shallow roots	244.280	206.05	187.567	133.4-296.8	87.64-273.2
Number of windward sinker roots in the ZRT	5	7	6	3-15	0-16
Basal diameter of windward sinker roots in the ZRT	4.158	5.819	5.327	2.954-11.05	3.606-9.185
Distal diameter of windward sinker roots in the ZRT	2.339	2.265	2.4	0.268-11.1	0.776-5.958
Length of windward sinker roots in the ZRT	84.858	76.77	65.57	46.96-145.7	45.91-82.19
Number of windward sinker roots beyond the ZRT	5	6	5	1-18	0-22
Diameter of windward sinker roots beyond the ZRT	1.705	1.791	2.003	0.917-2.629	1.597-2.426
Length of windward sinker roots beyond the ZRT	62.012	61.542	55.242	32.09-88.29	31.97-92.1

Table 3.2 Main architectural characteristics of the root pattern MRA0 compared to 24 trees from the Bilos dataset; (b) the windward sector.

Items of root dimensions (Perpendicular)	Model Value based on L19	Bilos Undamaged Value	Bilos Uprooted Value	Bilos Undamaged Range	Bilos Uprooted Range
Number of perpendicular shallow roots	10	7	6	3-9	1-10
Basal diameter of perpendicular shallow roots	5.912	12.316	12.242	8.48-18.38	7.027-19.71
Diameter at the end of the ZRT of perpendicular shallow roots	4.245	5.030	4.831	3.405-7.64	1.235-8.262
Diameter of perpendicular shallow roots beyond the ZRT	2.258	2.174	2.150	1.101-3.607	0.570-5.82
Length of perpendicular shallow roots	211.514	205.2	194.482	127.7-259.2	151.3-260.7
Number of perpendicular sinker roots in the ZRT	5	11	11	5-20	1-22
Basal diameter of perpendicular sinker roots in the ZRT	4.606	5.827	5.123	3.871-7.748	3.6-7.154
Distal diameter of perpendicular sinker roots in the ZRT	2.602	2.111	1.66	0.75-6.103	0.1-3.812
Length of perpendicular sinker roots in the ZRT	81.485	71.429	63.003	46.26-111.2	42.5-94.77
Number of perpendicular sinker roots beyond the ZRT	5	6	6	0-13	0-12
Diameter of perpendicular sinker roots beyond the ZRT	1.453	1.791	2.121	0.876-2.714	1.328-3.442
Length of perpendicular sinker roots beyond the ZRT	58.517	57.085	47.494	18.41-88.09	11.27-64.26

Table 3.3 Main architectural characteristics of the root pattern MRA0 compared to 24 trees of Bilos dataset; (c) the sectors perpendicular to the wind direction.

Items of root dimensions (Leeward)	Model Value based on L19	Bilos Undamaged Value	Bilos Uprooted Value	Bilos Undamaged Range	Bilos Uprooted Range
Number of leeward shallow roots	5	2	2	0-5	0-5
Basal diameter of leeward shallow roots	5.436	14.29	11.749	6-20.96	1.8-20.4
Diameter at the end of the ZRT of leeward shallow roots	4.016	4.473	4.562	0.4-7.474	1.2-6.809
Diameter of leeward shallow roots beyond the ZRT	2.272	1.844	1.879	0.2-2.68	0.7-4.091
Length of leeward shallow roots	240.681	191.63	206.856	103.3-243.8	149.9-273.2
Basal diameter of the leeward shallow root carrying the chuck	10.736	27.757	26.306	22.65-33.2	22.8-37.79
Basal diameter of the chuck	4.063	9.010	9.834	1.2-18.33	2.1-18.89
Distal diameter of the chuck	2.296	3.871	3.629	0.1-11.74	0.1-10.61
Distance between the stem base and the base of the chuck	47.172	37.938	38.003	22.47-71.78	9.971-59.84
Insertion angle of the chuck and the vertical plan perpendicular to the shallow root carrying it (°)	19.537	18.52	23.535	7.81-26.93	14.53-30.07
Length of the chuck	64.079	43.345	58.756	12.3-66.52	19.72-87.85
Number of leeward sinker roots in the ZRT	5	4	6	0-9	0-9
Basal diameter of leeward sinker roots in the ZRT	4.024	6.759	6.659	1.432-10.5	2.924-13.28
Distal diameter of leeward sinker roots in the ZRT	2.054	3.195	3.520	0.1-7.767	0.1-13
Length of leeward sinker roots in the ZRT	79.843	55.237	58.09	18.59-89.09	17.89-85.17
Number of leeward sinker roots beyond the ZRT	5	3	3	0-7	0-10
Diameter of leeward sinker roots beyond the ZRT	1.449	1.521	2.009	1.028-2.491	1.345-3.402
Length of leeward sinker roots beyond the ZRT	46.208	46.44	42.587	28.34-55.18	20.54-59.49

Table 3.4 Main architectural characteristics of the root pattern MRA0 compared to 24 trees of Bilos dataset; (d) the leeward sector.

3.2.2 Configuring the root anchorage model

Field research employs tree-pulling experiments to mimic tree uprooting behaviour during windstorm. A tree is pulled over at low and constant speed by a quasi-horizontal cable attached to a winch. In the same spirit, we modelled the underground mechanical response of the tree during windthrow resulting mainly from three components, namely root system architecture, root and soil material properties. The previous anchorage model (Yang et al., 2014a) was adapted to create virtual root patterns instead of importing digitized root systems. Figure 3.1 showed the wind action was mimicked by a horizontal displacement applied on the top of a tree stem. The bottom of the stem was attached to the top of the root system. The root system was modelled by MRA0, and was embedded in a large soil medium in the form of a rectangular parallelepiped. The embedded element method was defined for root-soil interactions, so root displacements were linearly constrained by soil movement in the vicinity (Abaqus Analysis User's Guide 6.13).

Mechanical behaviour of the root-soil system predicted by the model depends also on the root material properties. This study used mechanical parameters for roots previously established from literature and soil from measurements. Roots were assumed to be linearly elastic and brittle, with a damage law describing the quasi-brittle behaviour in tension, compression and bending. Soil material was defined to be homogeneous, linearly elastic and plastic with a Mohr-Coulomb yield criterion. Mathematical equations governing the constitutive behaviour of these materials are documented in detail in Yang et al. (2014a), and associated parameter values were given in Table 3.5. The root-soil system was subjected to gravity loading (g=9.81 $m.s^{-2}$; in -Y direction). The soil inward and outward movements were constrained at vertical boundaries (i.e. XY and YZ planes) of the soil medium, and the bottom of the soil medium is constrained (zero for all degrees of freedom).

Having defined material properties and boundary conditions for the root-soil system, it remains to assign appropriate mesh density for roots and soil. The embedded element method implies the characteristic length of root elements should be close to that of soil elements in the vicinity for accuracy reasons. Besides, mesh quality is of primary importance because it may influence simulation results. Therefore mesh density was refined for the ZRT of the root pattern and the soil area containing the root pattern. The mesh design in these regions was optimised through a preliminary study where 8 mesh densities were tested (average size from 0.64 m to 0.173 m in the central area of soil). The values of critical turning moment were found to stabilise at a mesh density of 0.187 m, thus this was selected for all subsequent numerical experiments. The mesh spacing was 0.187 m in the central area of the soil and ranging from 0.187 m gradually to 1.2 m in the distal area. For the root pattern, the mesh density was 0.1 m in the ZRT and 0.15 m elsewhere.

Item (soil)	Symbol	Value	Units	Item (roots)	Symbol	Value	Units
Density	ρ_s	1410	kgm^{-3}	Density	ρ_r	421.4	kgm^{-3}
Modulus of elasticity	E_s	19.86	MPa	Modulus of elasticity	E_r	8	GPa
Poisson ratio	ν	0.33	–	Shear modulus/Young's modulus	$\frac{G_r}{E_r}$	0.0755	–
Cohesion	c	21.402	kPa	Tensile strength	σ_{11}^t	43.2	MPa
Friction angle	ϕ	14.62	°	Compressive strength	σ_{11}^c	20.6	MPa
Dilation angle	ψ	0	°	Energy of fracture	G_f	209.4	Jm^{-2}
				Viscous parameter	η	0.000075	–

Table 3.5 Mechanical properties of roots and soil material: elastic and plastic (Mohr-Coulomb) for soil and elastic-brittle for roots

In terms of model output, we highlight the response curve representing turning moment (TM) as a function of deflection angle calculated at the base of the stem, the critical turning moment (TMc; maximum value of TM), the mechanical response of individual roots related to their root compartments during the overturning process, mechanical contribution of each main component, and soil mechanical response. The mechanical contribution of a root component was characterised by the relative difference between the critical turning moment calculated from the case with loss of a root component (MRA1–MRA12) and that from the reference case (MRA0). The results allow us to revisit some of the main issues highlighted in previous experimental studies.

For all configurations, the stem was 1.60 m in length, and the imposed displacement was 1.2 m. The soil domain was 10 m in length, 10 m in width and 5 m in depth. At the centre of the soil block, a parallelepiped area of 6 m in length, 6 m in width and 1.25 m in depth was partitioned to specify the region containing the root pattern.

The anchorage model was developed in Abaqus environment, version 6.13 (http://www.3ds.com/products-services/simulia/portfolio/Abaqus/). A Fortran subroutine UMAT was used to define root damage behaviour, and a set of Python scripts to generate all MRAs and implement them in the anchorage model.

3.3 Results

3.3.1 Modelling root system architecture and its morphological variations

Measurements of root classes and compartments along with root architectural data obtained from site L19 allowed us to build a root pattern recapitulating main root morphological traits of mature *P. pinaster*. Another existing dataset obtained from Bilos (Danjon et al., 2005), located in the same region (44°29’ N, 0°57’ W), contains 24 root systems of mature *P. pinaster* aged 50 with a mean DBH of 37.84 cm. These data allowed a comparison of the relevance of different morphological features. Like regular tap-root systems, the visual root pattern (MRA0) was defined by the ZRT composed of rapid tapered root segments surrounding the root stump and guyed by large and long shallow roots extending radially outward from the stump (Figure 3.1). Most of the root dimensions of the root pattern match the range of the same variables from Bilos dataset except basal diameters of shallow roots, because trees of the Bilos dataset are older than that of L19 (mean DBH = 38 cm for Bilos against 28 cm for L19). Furthermore, root morphological features exhibited by MRA0 agrees well with a number of experimental findings: The ratio of the root volume distributed to the prevailing wind sectors to that of perpendicular

sectors is close to 60:40 for Bilos dataset (Danjon et al., 2005). The ratio calculated for MRA0 is 50:40. Besides, the length of shallow roots is found to be highly reinforced in the wind direction (Danjon et al., 2005; Stokes et al., 1995). In our case, mean length of shallow roots in the windward and leeward sectors is 15% higher than that of perpendicular sectors (calculated from Tables 3.2, 3.4 and 3.3).

Figure 3.2 showed four examples out of 12 morphological scenarios designed for the root pattern: namely the root pattern without taproot (MRA1), root loss in the windward sector (MRA2), in the leeward sector (MRA4) and in the two sectors perpendicular to the prevailing wind direction (MRA3). For mature *P. pinaster* from the Bilos dataset, Table 3.6 shows experimental evidence of missing or insufficiently developed main root component(s): three of 24 trees developed limited taproot (27 - 35 cm in length); none or very few windward roots were present for three trees; six trees developed insufficient perpendicular shallow roots (1-3 roots in total per tree); and nine trees exhibited insufficient leeward roots. Sinker roots may also be absent in the windward or leeward sectors. Therefore modelled root morphological variations match experimental evidence.

Natural morphological variations	Occurrence	Corresponding simulation case
Insufficient taproot (length <= 35 cm)	3 (2)	MRA1
Insufficient windward shallow roots (fewer or equal to 1)	3 (3)	MRA2
Insufficient perpendicular shallow roots (fewer or equal to 3)	6 (5)	MRA3
Insufficient leeward shallow roots (fewer or equal to 1)	9 (5)	MRA4
Insufficient windward sinker roots (fewer or equal to 4)	4 (4)	MRA5
Insufficient perpendicular sinker roots (fewer or equal to 8)	3 (1)	MRA6
Insufficient leeward sinker roots (fewer or equal to 4)	6 (2)	MRA7
No chuck	3 (2)	MRA8
No second order sinker	4 (3)	MRA9
Insufficient distal windward shallow roots (length <= 35 cm beyond ZRT)	4 (2)	MRA10
Insufficient distal perpendicular shallow roots (length <= 35 cm beyond ZRT)	2 (1)	MRA11
Insufficient distal leeward shallow roots (length <= 35 cm beyond ZRT)	1 (0)	MRA12

Table 3.6 Root morphological variations found in 24 trees from the Bilos dataset in comparison to the 12 modelled simulation cases. Note that for “Occurrence” the form of “x(y)” indicates a total occurrence of x trees for all 24 trees and an occurrence of y trees for the 12 uprooted trees.

3.3.2 Comparing estimated root anchorage strength to experiments

The response curve is commonly used in tree-pulling experiments and modelling to interpret tree anchorage behaviour. It is important the model yields reasonable tree anchorage behaviour, particularly the root anchorage strength characterised by TMc. First, response curves derived from simulations and field tree-pulling experiments showed similar behaviour: TM increased first with deflection angle, with some eventual drops and recoveries, after reaching the maximum (TMc) it began to fall progressively (Crook and Ennos, 1996; Crook et al., 1997; Cucchi, 2004; Ennos et al., 1993; Fraser, 1962). Secondly, the TMc estimated by the simulation with MRA0 was compared to field measurements. The linear positive correlation between the critical turning moment and $H * DBH^2$ is commonly considered as a good empirical predictor of tree anchorage strength (Cucchi et al., 2004). A previous campaign of 100 field tree-pulling experiments carried out on *P. pinaster* cultivated in the same region (Landes de Gascogne, Aquitaine of southwest France) allowed estimation of TMc for a given $H * DBH^2$ value (Cucchi et al., 2004; Cucchi, 2004). These experimental results were used for the quantitative comparison. First the $H * DBH^2$ value corresponding to the root pattern was determined by the linear relationship between $H * DBH^2$ and the total root volume derived from L19. A total root volume of 0.12 m^3 matched an H*DBH2 of 1.30 m^3. The empirical linear relationships based on $H * DBH^2$ predicted a range of 40-70 kN.m for TMc. The TMc predicted by the simplified model with MRA0 was 37 kN.m, which was close to experimental values and only 7.5% smaller than the lower limit of the range.

3.3.3 Simulating tree overturning process

The overall behaviour of the root-soil system was well represented by the simulated response curve. We wondered if it was also the case at the level of individual roots. Figure 3.3 illustrated the different types of stresses within the main root components of MRA0 at a deflection angle = 15°. Results suggested that the taproot was bent, leeward shallow roots stressed in compression, and windward shallow roots in tension. In addition, the root breakage pattern related to the change in the TM was also studied. After the taproot was bent, breakage was detected deep in the taproot which led to the first main drop in turning moment. Secondly leeward shallow roots were highly stressed first in compression combined with bending at the base before snapping. The drops in turning moment due to leeward failure are not significant enough to trigger the overall failure of the root-soil system. Then several perpendicular shallow roots snapped successively from the leeward side to the windward side. Finally segments of windward shallow roots at branching points within the ZRT were stressed by elevated tension, and these stresses were highest when overall critical turning moment (TMc) was reached. The windward breakage

ultimately led to the overall anchorage failure of the root-soil system. During the pulling process, the stiffness of the root-soil system was sequentially reduced by failure of each main root class (the taproot, shallow roots from the leeward side to the windward side). Many sinker roots within the ZRT snapped in sequence roughly from the leeward side to the windward side. The soil in the basal area yielded progressively, which broadly coincided with the most stressed area in the root system.

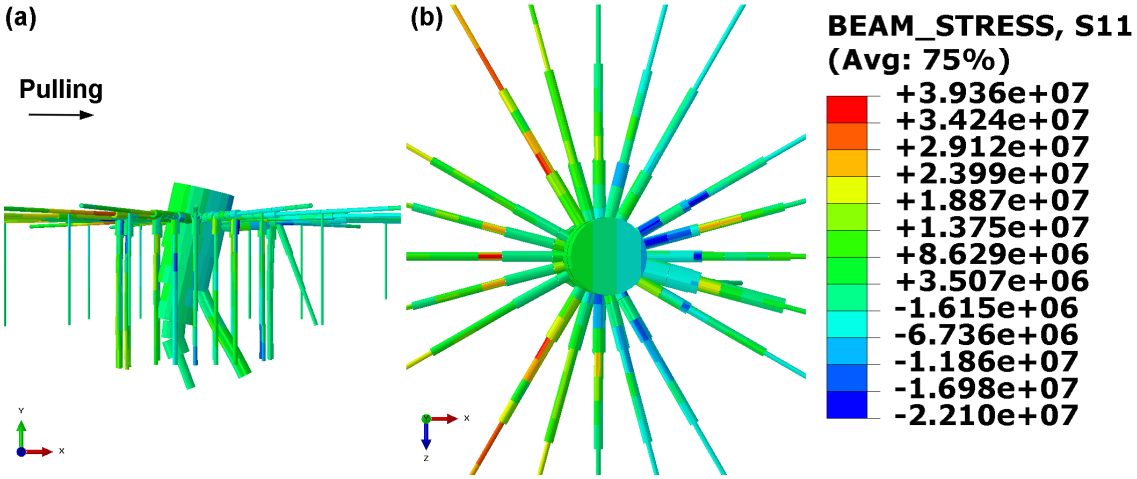

Figure 3.3 Different root components subjected to different types of stresses with respect to the prevailing wind direction (deflection angle = 15°): large leeward shallow roots were stressed in compression and bending close to the stem base; leeward sinkers in the ZRT were subjected to bending; windward shallow roots were stressed in tension further from the stem base. The most bent part of the taproot was already broken at this moment, which explains the absence of significant stresses. (a) top view; (b) side view.

3.3.4 Evaluating anchorage performance influenced by morphological variations

First, the same process was performed for all the other simulations to compare root breakage patterns. In the case of MRA0 and all cases with lateral root losses (MRA2-MRA4), root failure was likely to be initiated deep in the taproot, then start on the lee side close to the stem base and spread to the windward side. Accordingly, the first significant drop in turning moment is mainly due to the taproot, and the first recovery with decreased system stiffness is largely driven by leeward shallow roots. For the case without a taproot, lateral breakage occurred more evenly in both windward and leeward directions, and only small and gradual drops and recoveries in turning moment were recorded during the entire pulling process. This case is similar to the situation of a plate root system (Coutts, 1983, 1986). In the simulation, the absence of the

taproot delayed the leeward root snapping. Similarly for tree-pulling experiments with plate root systems, leeward roots might fail after windward roots have broken, i.e. after the critical turning moment is passed (Crook et al., 1997).

Secondly, response curves were calculated for simulations with MRA1-MRA12. The collection of response curves from all simulations (Figure 3.4) gave rise to a full evaluation of mechanical impact of each main root component. The main root anchorage components are: taproot accounting for 60.8% of the critical turning moment, the windward shallow roots along with associated sinker roots represented 24.8% of the critical turning moment, the perpendicular shallow roots with sinker roots represented 20.2% of the reference critical turning moment, windward sinker roots accounted for 9.6% of the critical turning moment, and leeward shallow roots with sinker roots accounted for 6.9% of the critical turning moment. Each of the other root components contributed less than 5% to root anchorage strength.

3.4 Discussion

3.4.1 Morphological variability of root patterns

Our method of building root patterns has enabled us to reveal the observed natural morphological variations of root systems in a simplified structure. For instance, root rot infected by fungi may cause considerably root damage and lead to reduced tree resistance to overturning (Fraser, 1962). Besides, the presence of old root stumps may prevent balanced root development and lead to morphological variations of root systems (Quine et al., 1991). Root systems without windward or leeward roots have also been observed in previous studies (Crook and Ennos, 1996; Crook et al., 1997). For older *P. pinaster*, the presence of hard pan or water table in soil may limit the taproot development (Coutts et al., 1990; Cucchi et al., 2004; Nicoll and Ray, 1996; Ray and Nicoll, 1998). The taproot, however, is believed to be a dominant factor in terms of root anchorage capacity (Danjon et al., 2005). To "compensate" for this restriction, a large number of sinker roots of similar depth may develop close to the stump, and along with the restricted taproot act as a unified taproot during uprooting (Crook et al., 1997). Apart from natural conditions, some silvicultural treatments may also alter the development pattern of root system morphology at young age. For example, development of surface roots can be limited by mechanical weeding (Danjon et al., 1999b; Deans, 1981; Hendrick, 1989; Savill, 1976).

3.4.2 A synthesis of experimental evidence supported by the model results

The spatial and temporal heterogeneity of root distribution gives rise to their different levels of mechanical response to windthrow, and different levels of mechanical contribution with respect to root morphological features. Our model demonstrated in detail that coarse roots from different locations played different mechanical roles in response to external wind forces. In addition, roots usually act successively instead of being stressed at the same time because the external forces are transmitted at different stages, from the trunk directly to the stump, then to the basal area of the root system, and eventually to locations from the stem (Coutts, 1983; Crook et al., 1997). Therefore natural morphological variations of root systems are found to have strong impact on tree stability.

A collection of experimental descriptive findings on morphological aspects were revisited to compare with the modelled prediction. Despite differences among root system morphologies and soil structures, the main root components and the soil roughly share similar qualitative behaviour during tree overturning for different plants of the same or different species, including plants with plate root systems and tap root systems ((Ennos et al., 1993) compared to (Coutts, 1983, 1986; Crook and Ennos, 1996; Crook et al., 1997)). This allows us to potentially widen the scope of our qualitative comparison for *P. pinaster* to other species. The different mechanical roles sequentially shared by main root components are repeatedly observed and analysed. First, the taproot behaviour within a tap-root system was examined: the taproot is found to rotate in the soil, moving towards the windward direction and subject to bending (Coutts, 1986; Crook and Ennos, 1996; Crook et al., 1997; Ennos et al., 1993; Mickovski and Ennos, 2003, 2002) . In some cases, it can break near the base (Crook and Ennos, 1996; Stokes, 1999). The taproot is found to be a dominant factor in terms of root anchorage, in particular for young seeded *P. pinaster* (Danjon et al., 1999a; Ennos et al., 1993; Ghani et al., 2009; Mickovski and Ennos, 2003, 2002). Secondly in terms of leeward laterals, they are found to be pushed deeper into soil, subjected to compression and bending (Coutts, 1983, 1986; Crook and Ennos, 1996; Crook et al., 1997; Stokes et al., 1998). They are very likely to break and snap very close to the stem base (Crook and Ennos, 1996; Crook et al., 1997; Stokes et al., 1998), and are found to contribute little to root anchorage strength compared to windward roots or the taproot for tap root system (Coutts, 1983, 1986; Crook and Ennos, 1996). In terms of the field observations above, our simulation revealed consistent results. But in some studies leeward failure is found to occur after the TMc is reached during field tree-pulling experiments (Crook et al., 1997), which differs from what the model predicted. This discrepancy between the model and the observations could result from the root mechanical behaviour being assumed to be elastic and brittle in tension and compression; and the root compressive strength was defined to be much

lower compared to the tensile strength (20.6 MPa against 43.2 MPa). However root materials subjected to compression (eventually combined with bending) could be non-brittle, with a period of plastic behaviour before snapping. Furthermore, the mechanical properties of leeward roots were defined as identical to all the other roots, but are probably not reinforced enough to sustain elevated bending stresses. Finally when considering windward laterals, literature shows that they are stressed in tension, eventually shear, and may either break or uprooted further from the stem base (Coutts, 1983, 1986; Crook and Ennos, 1996; Crook et al., 1997). The TMc can be characterized at the moment when windward laterals begin to snap (Crook et al., 1997). This is accompanied by successive breakage of many smaller windward roots (Crook and Ennos, 1996). The simulation captured the same breakage behaviour and the mechanical role of windward roots as in experiments. Indeed, with an abundance of data for brittle tensile behaviour of individual woody roots, root stressed in tension was well described by the damage model (Anderson et al., 1989; Coutts, 1983; Ennnos, 1990; Ennos, 1989; Stokes and Mattheck, 1996; Yang et al., 2014a). Analyses of TM related to root movement show shortly after windward root snapping, the turning moment only falls very slowly because the taproot is still active (Crook et al., 1997). The observed windward lateral uprooting, however, is not possible to model with the current configuration for root-soil mechanical interaction, namely the embedded element method. This is because the method assumed all roots segments were strongly attached to the soil medium in the vicinity. Windward roots are considered as a major component of root anchorage for plate root systems like *Picea sitchensis*, and several other species, namely older *P. pinaster*, *Impatiens glandulifera* and Mature *Helianthus annuus*. Soil movements are usually described with root movements: for plate-like root systems like Sitka spruce, further windward soil breaks at the edge of root-soil plate as the plate is lifted progressively (Coutts, 1983; Mickovski and Ennos, 2003, 2002). Soil beneath the plate may be stressed in tension and shear (Coutts, 1983).

To summarize, with a simplified root architectural parameter set, the simplified anchorage model was able to capture main mechanical characters of a tap root system subjected to overturning repeatedly reported in literature. The main difference of the behaviour of leeward shallow roots between the simulation and field observations was explained. Furthermore, this difference is considered to be minor because the mechanical contribution of the leeward hinge is too small to alter the overall behaviour of the root-soil system. Besides, the simplified root anchorage model also quantitatively agreed well with field data in terms of response curves and estimated root anchorage strength.

3.4.3 Variability in root anchorage induced by variability in root system morphology

Our simulations suggested a large variability in root anchorage capacity for the same species (*P. pinaster*) of similar size (Figure 3.4). This variability is closely related to the variations in root system morphology. Quantitative information indicated large root components close to the stem have the most important mechanical influence on root anchorage strength, which is consistent with experimental evidence: the loss of taproot alone may lead to a loss of more than half of the initial anchorage strength. In addition, large lateral roots can be determining factors for tree stability: the breakage of windward shallow roots led to overall failure and they contributed one fourth of initial anchorage strength, second only to the taproot. The mechanical influence of large shallow roots increased from the leeward side (6.9%) to the windward side (24.8%). Furthermore, windward sinkers also played a more important role for tree stability (9.6%) than leeward shallow roots. This is consistent with the experimental classification of main root anchorage components (Coutts, 1986; Crook et al., 1997) which suggested windward roots dominated leeward side. In addition, most roots from the basal area close to the stem were most stressed during uprooting. However shallow roots beyond the ZRT have little influence on anchorage performance of the root system. This may be closely linked to the self-optimisation design of the root system: roots from basal area are potentially most stressed, thus are generally reinforced with higher biomass allocation and stronger material properties for tree anchorage reasons; whereas distal root segments are mainly for water and nutrient acquisition. A large morphological variability was observed in Bilos dataset. A close examination on the various anchorage capacities of these trees also suggested the same trends: more uprooted trees developed insufficient taproots (two trees in uprooted group against one in undamaged group). In addition, two of uprooted trees had no windward roots whereas none of undamaged trees exhibited root loss in the windward sector. Besides most of the trees with insufficient development of perpendicular shallow roots were uprooted (five uprooted against one undamaged). Four trees from the uprooted group exhibited insufficient windward sinker roots whereas none of the undamaged group did.

3.4.4 Conclusion and Perspectives

The plastic development of root systems in response to various environmental conditions is a complex process occurring in the opaque soil medium. Root system development is closely linked to the above-ground activities such as biomass allocation, nutrient transport, and adaptive growth with respect to the prevailing wind. In addition, underground conditions such as temporal and spatial water and nutrient availability, mechanical impedance, mechanical

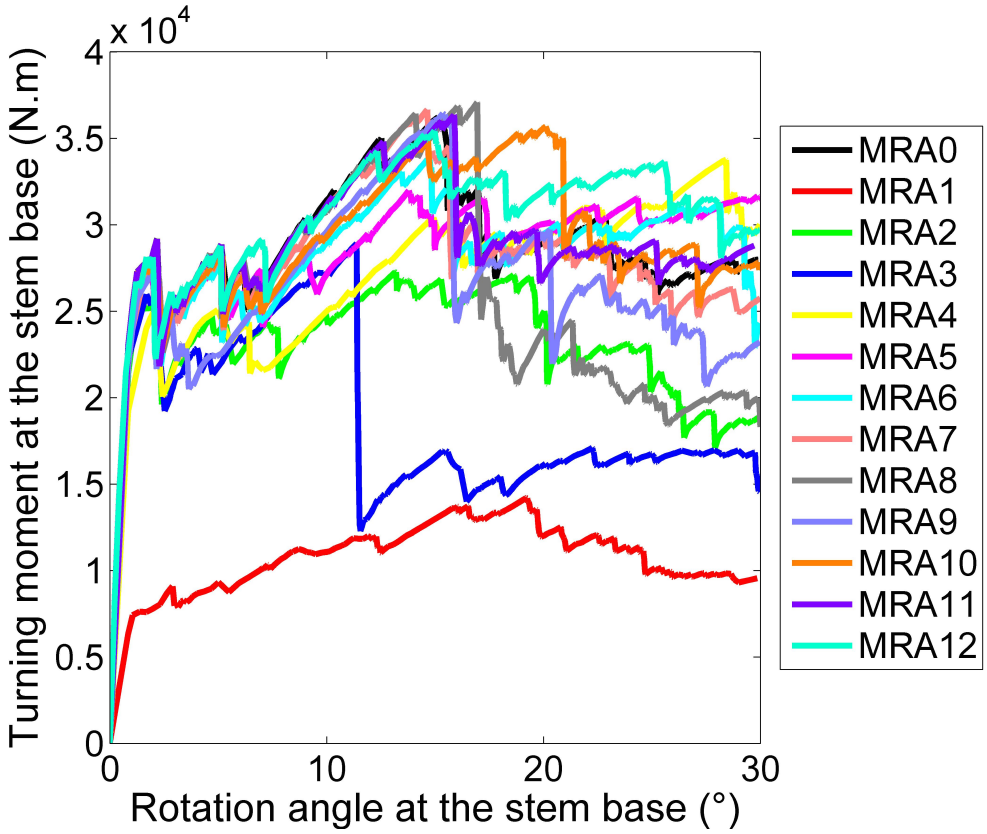

Figure 3.4 Response curves for all simulations representing the turning moment as a function of deflection angle (both calculated at the stem base). Simulations from MRA0 to MRA12 refer to the cases of root pattern designs in the Table 3.6

stress, etc. may also have a strong impact on the structural root growth, which determines the root system morphology (Coutts et al., 1999). The quantitative influences of variability in root system morphology on tree stability remain difficult to be evaluated in experimental research. However, the function of tree anchorage is of primary importance for tree survival. A modelling approach can be used in the hope of illustrating realistically these complicated processes thus providing quantitative information. Our simplified root anchorage model predicted realistic root anchorage performance with respect to experimental evidence. Therefore it can be used as a diagnostic tool to better understand morphological features of root systems involved in tree overturning behaviour. In this paper, we restricted our attention to mechanical consequences of morphological variability of root systems on tree anchorage function with a focus on root loss effect. But roots exhibit various forms of plastic response that modify the morphological features. For instance, edge trees of *P. pinaster* may develop a windward sector of larger size and thus become more resistant to the wind compared to inner trees (Cucchi et al., 2004). Besides, in the most stressed area of the root system the large roots develop strengthened

mechanical stiffness or strength (Stokes and Mattheck, 1996). Adaptive growth has been observed with cross-sections of I- or T- beam shapes for wind-oriented lateral roots close to the stem (Coutts et al., 1999; Nicoll and Ray, 1996). These characteristics may also enhance the function of root anchorage, and this can be investigated further with the anchorage model.

Chapter 4

Variations in roots and soil properties: impact on tree anchorage

Publication in preparation

Ming Yang, Pauline Défossez, Frédéric Danjon, Thierry Fourcaud. Variations in roots and soil properties: impact on tree anchorage.

Abstract

Tree anchorage is a primary function for plant survival which may approach its limit under extreme conditions such as windstorms. To better understand the processes and important factors influencing the windthrow, we have analysed the mechanical effects of root geometry and the material properties of roots and soil on the tree anchorage capacity with the recently developed anchorage model. The root system was represented by a 3D root pattern summarizing an adult *Pinus pinaster*. Taguchi's method was applied to reduce the large number of simulations. We have for the first time quantified separately the mechanical impact on root anchorage performance caused by variations in root geometry and material properties of roots and soil. Results showed root morphological traits played a dominant role over root and soil material properties, which was consistent with previous results on above-ground parts of the tree. Tree rooting depth, the dimensions of the basal area characterized by the Zone of Rapid Taper and the windward sector were found to be the most important factors. In addition, these important factors were supported by the previous results from the morphological simulation analyses and experimental evidence. These quantitative results are promising to be included in improvements in terms of model parameterization and simplified expressions of tree anchorage strength.

Key words: root anchorage, Finite Element Method, sensibility analysis, Taguchi's method, *Pinus pinaster*, tree stability

4.1 Introduction

Tree anchorage is a primary function of roots which concerns not only the basic mechanical self-support for the tree, but the mechanical resistance against natural hazards such as windstorms and snows as well (Fournier et al., 2013). There has been increasing damage induced by windstorms in Europe since the last century due to increasing growing stock. And it is predicted that the intensity of such storm events will increase in the future (Gardiner et al., 2010). As forests are involved in major economic activities in many countries worldwide and associated with a wide range of eco-system services (Chazdon, 2008), it is important to estimate the associated risks caused by windstorms. Uprooting is generally considered as a major failure mode, in particular for adult trees of large size in conditions of saturated soils (Gardiner et al., 2010). For example, this mode accounted for 69% of primary damage associated to the windstorm Klaus hitting Aquitaine region in France in 2009 (source: IFN). Understanding and evaluating tree anchorage behaviour are essential for risk prediction of wind damage. So far efforts have been mostly concentrated on field observations of windstorm damages (Cucchi and Bert, 2003; Quine, 1995) and experimental studies based on static tree-pulling tests (Cucchi et al., 2004). The anchorage strength of individual trees is thus estimated using statistical correlations between observed damage mode (resp. ultimate uprooting force) and tree allometric variables (height, dbh, stem weight, etc.). A number of models of wind risk prediction have been developed during the last 20 years (Gardiner et al., 2008), which are often implemented in decision support systems designed for forest managers (see ForestGales for instance, http://www.forestry.gov.uk/fr/INFD-5V8JC8). Although running at the stand and regional scales, most of them are based on mechanistic models of stem failure but empirical relationships of root anchorage strength (Ancelin et al., 2004; Gardiner et al., 2000; Lundström et al., 2007; Peltola et al., 1999). However empirical relationships neither provide any understanding of the underlying physical processes, nor include the effects induced by variations in root system architecture.

More complex root anchorage models have been developed taking into account the main structural components of the root system, as well as soil mechanical characteristics, using spring elements (Blackwell et al., 1990; Coutts, 1986). These models have only been applied to Sitka spruce that presents shallow root systems, but are not generic to be applied to more complex root system architecture. Moreover they are not adapted to describe realistically soil mechanical and physical behaviour. With recent developments in 3D digitization, a large amount of data of root system architecture has become available to be incorporated in more sophisticated numerical root anchorage models. For instance the Finite Element Method (FEM) was used to study numerically tree overturning processes considering explicitly the two main objects of the system, i.e. the root system and the soil medium, and their interactions. Realistic

digitized root systems were used to study the anchorage behaviour of poplar trees using this modelling approach (Dupuy et al., 2007). Simulations were carried out on 3D schematic patterns of tree root systems in order to compare the anchorage behaviour of different tree species (Dupuy et al., 2005b). The relative impact of different root components (e.g. taproot, deep and shallow lateral roots) was also studied through FEM analyses with simple 2D root patterns (Fourcaud et al., 2008). However most simulations performed in these previous studies used soil properties established for theoretical soil types (i.e. without considering real field data) as well as idealized root properties without failure. Recently an improved version of anchorage model has been developed considering individual root mechanical response more realistically, with a root breakage law within a real root system architecture (Yang et al., 2014a). Soil properties were also described realistically based on parameters measured in the laboratory. The model was tested on *P. pinaster* trees with available digitized root system architecture, soil and root mechanical information, together with a tree-pulling test. In addition, a simplified version of the model was presented, which reduced the highly complex topological features of real root systems of adult trees in order to study the mechanical impact of specific root compartments (i.e. four sectors defined with respect to wind direction, the Zone of Rapid Taper (ZRT), and root components, e.g. taproot, sinkers, laterals, etc.). Numerical sensitivity analyses carried out on *Pinus pinaster* root systems allowed for discrimination among impacts of root components on tree anchorage strength in sandy soils (Chapter 3, paper in preparation). The aim of the present study was to complete these sensitivity analyses considering variations in root allometry and soil mechanical properties for a root system topology of a given species *P. pinaster*, in order to identify the main structural and physical traits that influence root anchorage performance. We stress the root geometrical aspect compared to that of root and soil material properties because previous studies on above-ground parts of the tree confirmed that morphological aspect has a dominate effect over material properties (Sellier and Fourcaud, 2009; Sellier et al., 2008). We hypothesised this held true for the response of the below-ground part of the tree.

4.2 Materials and Methods

4.2.1 Reference root pattern

The morphology of mature *Pinus pinaster* root systems has been studied and described in previous papers (Danjon et al., 1999a, 2005, 2013a). Root systems of all ages can be described by a typology that defines specific root compartments and root classes. Based on this descriptive method, a reference mature *P. pinaster* root pattern was built to be used for the numerical

simulations. The root pattern was a large central taproot guyed by long horizontal shallow roots extending in all directions outward from the stump. In addition, a thick oblique sinker root of second order extended from the taproot. A number of third order sinker roots developed from the shallow roots close to the taproot. The Zone of Rapid Taper (ZRT) of horizontal shallow roots was characterised by the root segments close to the stump with diameters tapering off from the stem base. In particular, one leeward shallow root carrying a chuck root in the ZRT was distinguished from other leeward shallow roots by its larger diameter in the ZRT and the large chuck root it carried. The geometrical parameters of the root pattern were determined based on the measurements of seven root systems of 19-yeal-old *P. pinaster* with a mean Diameter at Breast Height (DBH) of 28.45 cm. Trees were excavated from the site L19 located in the southwest of France (44°42' N, 0°46' W). Mean annual rainfall was 850 mm and mean annual temperature 13°C. The site was characterised by a sandy podsol with a deep discontinuous hard pan located at about 70 cm depth and a water table close to the soil surface during winter. Further information can be found in Danjon et al. (Danjon et al., 2013a). Details on design of the root pattern with respect to adult *P. pinaster* features and validation of the root pattern shape in terms of root system morphology can be found in Tables 4.1, 4.2, 4.3, 4.4 and Chapter 3. For simplicity, all material parameters held constant within the root pattern. Table 4.2 gave the parameter values for material properties of roots and soil.

Items of root dimensions (the central part)	Model Value based on L19
Length (radius) of the ZRT	87.031
Basal diameter of the stump	35.054
Distal diameter of the stump	33.22
Depth of the stump	-33
Basal diameter of the taproot	29.218
Distal diameter of the taproot	5.11
Depth of the taproot	-112.779
Basal diameter of the 2nd order sinker	8.088
Angle between the axis of the 2nd order sinker and the vertical plan perpendicular to the pulling direction (°)	22.477
Length of the 2nd order sinker	76.807

Table 4.1 Main architectural characteristics of the reference root pattern; (a) the central part.

Items of root dimensions (the windward sector)	Model Value based on L19
Number of windward shallow roots	5
Basal diameter of windward shallow roots	4.822
Diameter at the end of the ZRT of windward shallow roots	3.721
Diameter of windward shallow roots beyond the ZRT	2.198
Length of windward shallow roots	244.28
Number of windward sinker roots in the ZRT	5
Basal diameter of windward sinker roots in the ZRT	4.158
Distal diameter of windward sinker roots in the ZRT	2.339
Length of windward sinker roots in the ZRT	84.858
Number of windward sinker roots beyond the ZRT	5
Diameter of windward sinker roots beyond the ZRT	1.705
Length of windward sinker roots beyond the ZRT	62.012

Table 4.2 Main architectural characteristics of the reference root pattern; (b) the windward sector.

Items of root dimensions (the sectors perpendicular to the prevailing wind)	Model Value based on L19
Number of perpendicular shallow roots	10
Basal diameter of perpendicular shallow roots	5.912
Diameter at the end of the ZRT of perpendicular shallow roots	4.245
Diameter of perpendicular shallow roots beyond the ZRT	2.258
Length of perpendicular shallow roots	211.514
Number of perpendicular sinker roots in the ZRT	5
Basal diameter of perpendicular sinker roots in the ZRT	4.606
Distal diameter of perpendicular sinker roots in the ZRT	2.602
Length of perpendicular sinker roots in the ZRT	81.485
Number of perpendicular sinker roots beyond the ZRT	5
Diameter of perpendicular sinker roots beyond the ZRT	1.453
Length of perpendicular sinker roots beyond the ZRT	58.517

Table 4.3 Main architectural characteristics of the reference root pattern; (c) the perpendicular sectors.

Items of root dimensions (the leeward sector)	Model Value based on L19
Number of leeward shallow roots	5
Basal diameter of leeward shallow roots	5.436
Diameter at the end of the ZRT of leeward shallow roots	4.016
Diameter of leeward shallow roots beyond the ZRT	2.272
Length of leeward shallow roots	240.681
Basal diameter of the leeward shallow root carrying the chuck	10.736
Basal diameter of the chuck	4.063
Distal diameter of the chuck	2.296
Distance between the stem base and the base of the chuck	47.172
Insertion angle of the chuck and the vertical plan perpendicular to the shallow root carrying it (°)	19.537
Length of the chuck	64.079
Number of leeward sinker roots in the ZRT	5
Basal diameter of leeward sinker roots in the ZRT	4.024
Distal diameter of leeward sinker roots in the ZRT	2.054
Length of leeward sinker roots in the ZRT	79.843
Number of leeward sinker roots beyond the ZRT	5
Diameter of leeward sinker roots beyond the ZRT	1.449
Length of leeward sinker roots beyond the ZRT	46.208

Table 4.4 Main architectural characteristics of the reference root pattern; (d) the leeward sector. Note that the root diameter and length are in cm.

4.2.2 Root anchorage model

The root anchorage model recently developed by Yang et al. (2014a) within the FEM software Simulia Abaqus 6.13 (http://www.3ds.com/products-services/simulia/portfolio/abaqus/latest-release/) was used in this study after having been tested for the same species at different development stages. The root anchorage model was composed of a large parallelepiped soil domain (length × width × depth: 10 m × 10 m × 5 m), a root system was meshed with beam elements and placed in the centre of the soil domain with a rigid vertical stem attached to the top of the root stump. Tree pulling was mimicked by a horizontal displacement applied at 1.63 m high on the stem. Soil material properties were assumed to be linear elastic at the initial state and plastic following the Mohr-Coulomb's failure criterion available in the Abaqus material library. Values of soil mechanical parameters, namely the Young's modulus, the angle of internal friction and soil cohesion, were determined by direct shear tests in laboratory with 12 soil samples with the same soil moisture as measured in the Nézer forest (Table 4.2; Chapter 2). Roots were assumed to be quasi-brittle materials characterised by a combination of linear elastic behaviour during the initial state and damage behaviour following a damage criterion and a damage evolution law (Yang et al., 2014a). Root segments were thus able to fail in tension, compression and bending. Due to scarcity of mechanical data for *P. pinaster* roots, parameters of root material properties were derived from a combination of diverse experimental data of green wood and structural roots previously published for several forest species (Khuder et al., 2007; Kretschmann, 2010; Stokes and Mattheck, 1996; Stokes et al., 1997b). Root-soil mechanical interactions were modelled by the embedded element method which consisted of imposing kinematic consistency of root nodal displacements with that of soil in the vicinity. The outward and inward Degrees Of Freedom (D.O.F.) with respect to each vertical face of the soil domain were fixed to 0 and the bottom of the soil domain was defined by a fully built-in condition (all six D.O.F. set to 0; ENCASTRE in Abaqus). The entire root-soil system was subjected to a gravity load prior to and during the overturning process with the acceleration of $g = 9.81\ m \cdot s^{-2}$ in the vertical direction $(-Y)$. The root system was meshed with 2-node linear Timoshenko beam elements which took into account the transversal shear behaviour (B31 in Abaqus element library). The soil domain was discretised into 8-node linear brick element with the formulation of reduced integration (C3D8R in Abaqus element library). To study the root anchorage behaviour, we examined the turning moment vs deflection angle response curve, which was defined for each simulation at the stem base. Therefore the critical turning moment (TMc; i.e. the maximum value of turning moment) can be derived from the response curve and used as an output variable for the sensitivity analysis.

Item (soil)	Symbol	Value	Units	Item (roots)	Symbol	Value	Units
Density	ρ_s	1410	kgm^{-3}	Density	ρ_r	421.4	kgm^{-3}
Modulus of elasticity	E_s	19.86	MPa	Modulus of elasticity	E_r	8	GPa
Poisson ratio	ν	0.33	–	Shear modulus/Young's modulus	$\frac{G_r}{E_r}$	0.0755	–
Cohesion	c	21.402	kPa	Tensile strength	σ_{11}^t	43.2	MPa
Friction angle	ϕ	14.62	°	Compressive strength	σ_{11}^c	20.6	MPa
Dilation angle	ψ	0	°	Energy of fracture	G_f	209.4	Jm^{-2}
				Viscous parameter	η	0.000075	–

Table 4.5 Mechanical properties of roots and soil material: elastic and plastic (Mohr-Coulomb) for soil and elastic-brittle for roots

4.2.3 Numerical experiments

The sensitivity analyses were performed separately on two distinct parameter sets corresponding to root geometry and root and soil material properties respectively. Simulations were done on a reference *P. pinaster* root system topology built from field data (see the section of "Reference root pattern"). However, in order to simplify the system, we decided to only consider the root components with a major influence derived from the previous numerical study (Chapter 3, paper in preparation), namely the taproot, the windward shallow roots, the shallow roots perpendicular to the direction of prevailing wind, the leeward shallow roots and the windward sinker roots.

Taguchi's method was used to design the numerical experiments, in the same manner as Sellier and Fourcaud (2009) who investigated the geometrical and material influence of the tree crown on the aerodynamic behaviour of *P. pinaster* trees subjected to strong winds. Considering the large amount of input variables (usually called "factors") to be tested (23 for geometry and 11 for materials), Taguchi's method allowed for reduction of the number of experiments to be performed without restricting the scope of the problem. The two sets of parameters were separately examined considering a variation of ±20% of reference values taken from field data, which gives three different values for each parameter. Regarding the number of factors and levels of variation, the orthogonal array L54 was built for the geometrical parameter set (See Appendix C), and L27 for the material parameter set (see Appendix C). The number of simulations to be performed was thus reduced (from 3^{23}) to 54 for the geometrical parameter set and (from 3^{11}) to 27 for the material parameter set. The sensitivity of the system to a specific input variable (either from the geometrical set or from the material set) was defined by its influence on the output variable (i.e. critical turning moment) measured by the relative variation:

$$Var_j^i = \frac{\bar{Y}_j^i}{\bar{Y}} \tag{4.1}$$

where Var_j^i is the relative variation of the output variable Y (the critical turning moment) estimated for the input factor i (either geometrical or material parameters) at the level of variation j (-20%, 1 or +20%), $\bar{Y}$ the mean value of the output variable averaged over all the simulations performed for the parameter set (either geometry or material), and $\bar{Y}_j^i$ the mean value of the output variable averaged over simulations at the level of variation j for the factor i.

4.3 Results

The critical turning moment was insensitive to most of the factors in both the geometrical and the material parameter sets. Among a few cases with stronger factor impacts, the variations

with respect to different parameters may be divided into different levels. The highest variations were always induced by root geometrical parameters. Secondly the material properties, namely root material strength and soil plastic failure, have more mechanical influence than stiffness parameters (Young's modulus, Poisson ratio, etc.) on the tree anchorage behaviour.

4.3.1 Root geometry

Figure 4.1 showed the effects of geometrical variations ($\pm$20% for all parameters) on the critical turning moment (TMc) which characterised the root anchorage strength. TMc varied moderately with most of the factors. However we identified particularly the marked variations with regard to the depth of the taproot which defined the tree rooting depth (about $\pm$15%). Secondly, sensitive responses also occurred to the variations in the intermediate diameter of the taproot (measured at three-fourths of total taproot length from the base) and the dimensions of the ZRT. Finally, the basal diameter of the taproot and that of the windward shallow roots had a stronger influence than the rest of parameters. The critical turning moment varied positively with the variations of these factors, in particular linearly with the taproot depth within the defined interval. All the other factors had negligible influence on the root anchorage strength.

These factors ranked by their mechanical influence were consistent with results from the previous study analysing the mechanical impact of major root loss with the same reference root pattern and the root anchorage model (Chapter 3). The combination of the current and the previous studies indicated the most important geometrical factors coincided with the major failure points during successive root breakage. These major failure points were found to lead to either significant loss in turning moment or significant reduction in the stiffness of the root-soil system during the overturning process.

4.3.2 Material properties of soil and roots

Figure 4.2 showed the response of the TMc to variations in root and soil material properties. Similarly to the geometrical parameters, most of the material parameters had little effect on root anchorage strength. The two most important factors, the root tensile strength and root compressive strength, only gave rise to less than 8% of variation in TMc, slightly larger than all the other material factors. The variations in TMc were positive and linear regarding these two factors. In addition, soil cohesion and the angle of internal friction also had a noticeable influence on the root anchorage. The TMc varied positively but nonlinearly with these factors.

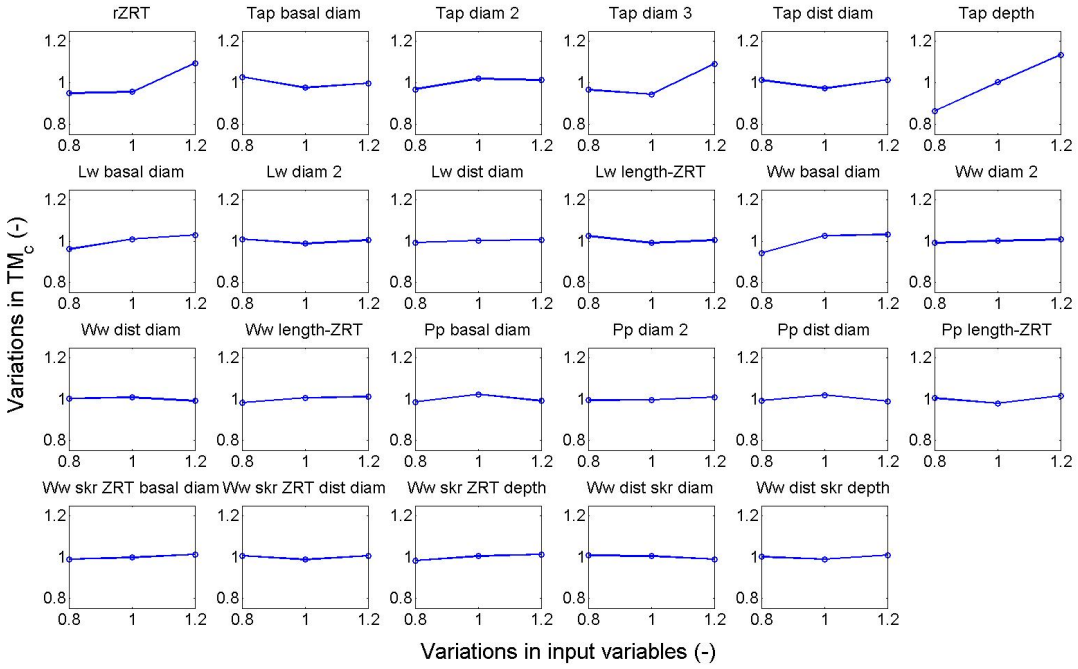

Figure 4.1 Variations in root anchorage strength caused by $\pm 20\%$ of variation in each root geometrical factor, namely, the radial dimension of the ZRT measured from the stump centre (rZRT), the basal diameter of the taproot, the intermediate diameters of the taproot (Tap diam2 and Tap diam 3), the distal diameter of the taprrot (Tap dist diam), the depth of the taproot (Tap depth), the basal diameter of the leeward shallow roots (Lw basal diam), the intermediate diameter of the leeward shallow roots (Lw diam 2), the distal diameter of the leeward shallow roots (Lw dist diam), the length of the leeward shallow roots outside the ZRT (Lw length-ZRT), the basal diameter of the windward shallow roots (Ww basal diam), the intermediate diameter of the windward shallow roots (Ww diam 2), the distal diameter of the windward shallow roots (Ww dist diam), the length of the windward shallow roots outside the ZRT (Ww length-ZRT), the basal diameter of the perpendicular shallow roots (Pp basal diam), the intermediate diameter of the perpendicular shallow roots (Pp diam 2), the distal diameter of the perpendicular shallow roots (Pp dist diam), the length of the leeward shallow roots outside the ZRT (Pp length-ZRT), the basal diameter of the windward sinker roots in the ZRT (Ww skr ZRT basal diam), the distal diameter of the windward sinker roots in the ZRT (Ww skr ZRT dist diam), the depth of the windward sinker roots in the ZRT (Ww skr ZRT depth), the diameter of the windward sinker roots outside the ZRT (Ww dist skr diam) and the depth of the windward sinker roots outside the ZRT (Ww dist skr depth).

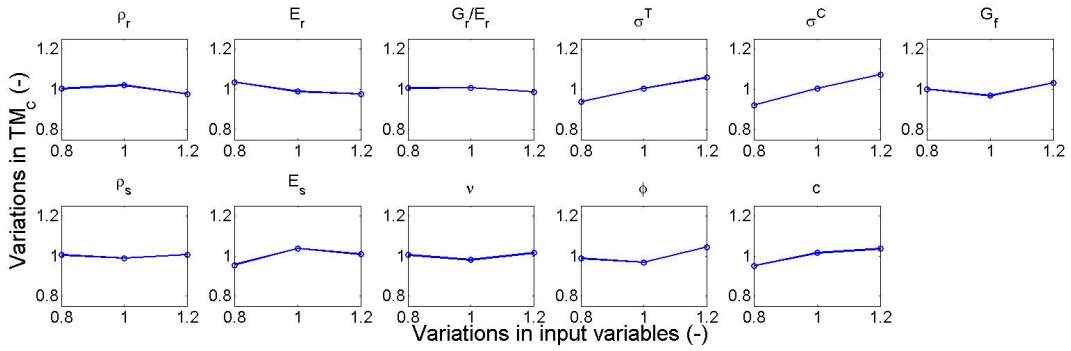

Figure 4.2 Variations in root anchorage strength caused by ±20% of variation in each factor of the root and soil material properties, namely, root density (ρ_r), Young's modulus of root material (E_r), the ratio of shear modulus with respect to Young's modulus of root material ($\frac{G_r}{E_r}$), root tensile strength (σ^T), root compressive strength (σ^C), root fracture energy (G_f), soil density (ρ_s), Young's modulus of soil material (E_s), Poisson ratio of soil material (ν), angle of internal friction of soil (ϕ) and soil cohesion (c).

4.4 Discussion

This sensitivity analysis of *P. pinaster* root anchorage strength in relation to geometrical and material factors was based on simulations performed with the FEM software Abaqus and completed a previous study focusing on the effect of root system architecture (Chapter 3).

4.4.1 Key factors of root anchorage strength

Our study suggests that root morphology has a predominant influence on tree anchorage strength in comparison to wood and soil material properties. Indeed all of the most pronounced effects on the critical turning moment came from variations of tree rooting depth, the dimensions of the ZRT, the taproot and windward shallow roots. This could also be indirectly supported by some basic mechanical concepts from beam theories. The overall failure of the root-soil system depends largely on successive breakage of individual roots under tension, compression and/or bending. The force required to break a root segment in tension or in compression is linearly correlated to its tensile or compressive strength but related to the square of its diameter. For roots subjected to bending, the maximum bending moment required to break a root segment is related to the maximum deflection and the fourth power of the root diameter, and is inversely related to the square of the distance of the failure point to the fixed end of the root segment. This suggests that variations in root diameters could lead to more significant effects on root failure behaviour, and therefore the overall root system failure, than the same scale of variation in root material strength.

This result is consistent with a similar sensitivity analysis carried out by Sellier and Fourcaud (2009) on the dynamical response of the above-ground structure of *P. pinaster* trees submitted to turbulent winds. However, this last study showed more pronounced effects probably caused by tree dynamical behaviour, e.g. a variation in a range of $\pm 20\%$ of the stem DBH resulted in a variation of more than 100% of the turning moment calculated at the stem base.

4.4.2 Toward model simplifications

The root anchorage model consisted of many input variables including those tested in this study: 23 geometrical factors and 11 material factors. This is mainly due to the fact that the entire root system architecture is explicitly taken into account and all material properties require a full parameter description in the model. *A priori*, this type of model requires a detailed knowledge of each compartment, namely root system architecture and material properties. However this is sometimes difficult to achieve because it requires extensive field work and laboratory tests to supply model information. According to results of our sensitivity analysis, only a limited number of factors control important changes in the overall root anchorage behaviour. This implies that a number of simplifications can be made to the model.

In terms of model parameter estimation, different levels of priority should be considered with respect to the mechanical impact on root anchorage behaviour evaluated for each parameter. For instance, instead of trying to integrate every detail of the root system architecture which takes tremendous time to measure in the field, measuring only the dimensions of the taproot, the ZRT and large windward shallow roots should be sufficient to provide an approximate estimation of root anchorage strength. In terms of material properties, most attention should be focused on root and soil material strength.

Improvements in terms of modelling could also be made based on the knowledge derived from the sensitivity analysis. Our finite element model offered its advantages when it concerned the understanding of a specific mechanism, the tree overturning for example. Because every aspect of the problem can be either well described or modelled with a simplified version, a realistic description leads to a realistic simulated overturning process at different levels, namely individual root behaviour, soil deformation and the overall response of the root-soil system. Visualisations of these processes allow exploration of hidden features during field research. But a realistic description implies not only tremendous measurements but higher costs in terms of computation time as well. Similarly to the idea for improvements for model parameter estimation, the model improvements may be grounded on the solid model description of root anchorage and the hierarchical organisation of different factors provided by results of the sensitivity analysis. An improved model should in particular describe the most important factors in detail and simplify the aspects associated with factors of minor impacts.

4.4.3 Relevance of important factors

The root anchorage model was tested in the previous study (Chapter 3) in terms of simplified morphological representation of the root system and mechanical response to overturning as a function of tree size. The key geometrical factors suggested by the current study are consistent with the previous results. The taproot (especially the maximum depth of the taproot) and the dimensions of ZRT which characterise the size of the root-soil plate are the two elements found to be essential to tree anchorage capacity. Root anchorage strength barely changed with most of the other parameters tested. According to the previous analysis on mechanical impact of major root loss (Chapter 3), the absence of the taproot led to a 60.8% decrease in critical turning moment. Likewise the windward shallow roots, second contributing factor, led to a loss of 24.8% in critical turning moment in case of missing. Therefore it is not surprising that ±20% root geometrical variations generally change relatively little root anchorage strength. In addition, the key factors found in this study are supported by a number of experimental facts (Coutts, 1983, 1986; Crook et al., 1997; Cucchi et al., 2004). These findings have been commonly used in empirical relationships of risk models and analytical anchorage models to estimate the root anchorage strength (Achim and Nicoll, 2009; Blackwell et al., 1990; Gardiner et al., 2000; Peltola et al., 1999). The windward sector highlighted in our study was also found to play an important role for edge trees of *P. pinaster*, characterized by larger size and more resistive response of these trees compared with inner trees from the same stand (Cucchi et al., 2004). Furthermore, some other types of root adaptive growth may be explained: tap-root systems with a well-developed taproot usually exhibit better root anchorage performance; root systems tend to allocate more biomass to the ZRT and to the windward and the leeward sectors, because reinforcement in the main root components in these areas is mechanically more efficient than in other sectors (Danjon et al., 2005). Most factors of material properties had a secondary impact on root anchorage strength compared to geometrical parameters. In addition, root material strength was found to be more important than soil strength. In terms of material strength of structural roots, little information has been found for these properties and variations within a tree directly linked to the tree anchorage strength (Niklas, 1999; Stokes and Mattheck, 1996). Probably because it is difficult for field research to directly link different contributing factors of root and soil material properties involved to the tree performance during overturning process; and it is also not obvious to separate them from other involved factors acting simultaneously.

4.4.4 Perspectives

The model described the individual root behaviour mainly based on experimental findings for green wood. However, the compositions of root materials are not exactly the same as stem wood (eg. (Bert and Danjon, 2006)); moreover most root mechanical properties are not well known. Measurements of the mechanical properties of large structural roots and their variations with respect to the location relative to the tree stem could be helpful in validating our results. In terms of soil mechanical properties, we only examined one dataset representing one soil under fixed conditions (humidity, porosity, etc.) with moderate variations ($\pm$20%). In natural conditions, soils exhibit a large temporal and spatial variability in natural forest conditions and are strongly influenced by environmental factors (presence of hard pan, water content, etc.) (Danjon et al., 2005; Fraser, 1962). The effects of these factors are still less known (Kamimura et al., 2013). These heterogeneous features may be taken into account further by defining different soil horizons with different mechanical properties and water content.

Conclusion

Cette thèse avait pour objectif d'améliorer notre compréhension du processus de déracinement de l'arbre et d'identifier des traits structuraux et matériels ayant un effet du premier ordre sur l'ancrage racinaire du Pin maritime (*P. pinaster*). Nous avons utilisé un modèle FEM qui présente l'avantage d'intégrer à la fois l'architecture racinaire, les propriétés géométriques et mécaniques des racines, la résistance mécanique du sol et les propriétés d'interface racines-sol. Ce modèle est donc bien approprié pour examiner le rôle de chacun de ces facteurs sur la résistance globale du système sol-racines. Mais cela nécessite des données expérimentales pour modéliser et paramétrer ces différents compartiments (architecture, racines, sol). Or l'architecture, les propriétés des racines et du sol présentent en milieu naturel une grande variabilité dont il faut également tenir compte. La démarche suivie dans cette thèse est donc de décrire au mieux la physique de l'ancrage tout en intégrant des connaissances sur la variabilité des paramètres en un lien étroit avec les études expérimentales.

Un premier résultat important de cette thèse concerne l'introduction de la rupture dans le modèle. Jusqu'ici, les modèles FEM décrivaient une déformation plastique des racines. Le modèle actuel présenté dans le chapitre 2 permet de simuler et de suivre la chronologie des ruptures successives au cours du processus de déracinement. Cela permet de définir un seuil de rupture globale de l'ancrage comme une résultante de l'architecture et de la résistance des matériaux en jeu (racines, sol). C'est un résultat prometteur pour la modélisation des risques au vent. Car il devrait permettre à terme d'améliorer les modèles de risque au vent actuels qui n'incluent pas de relation mécaniste de rupture de l'ancrage à la différence des relations utilisées pour la rupture du tronc (le volis). Un second résultat important est l'évaluation du modèle. L'évaluation de ce type de modèles FEM se heurte aux limites expérimentales actuelles (i) des limites techniques de caractérisation de l'architecture racinaire (ii) une faible connaissance des propriétés mécaniques (racines de structure, sol forestier, interface sol-racines). Notre approche a consisté à améliorer le paramétrage du modèle pour les racines et le sol en se basant sur des mesures et non sur des valeurs théoriques comme cela avait été fait jusqu'à présent. Le modèle a été confronté à un essai de flexion pour lequel l'ensemble des paramètres a été mesuré (hormis la résistance mécanique des racines). On a alors exploré un ensemble de sorties du

modèle qui n'avait pas été exploitées jusqu'ici et évalué le modèle sur sa capacité à prévoir la courbe de réponse force-déplacement mais aussi la rigidité de flexion, le travail fourni par le système racine-sol lors du basculement de l'arbre, et la localisation des endommagements. Nous avons démontré que la nouvelle version du modèle incluant la rupture des racines améliore significativement les prévisions du modèle.

Dans la même logique, nous nous sommes appuyés sur les données expérimentales pour construire une architecture modèle simplifiée de système racinaire de *P. pinaster* avec l'idée d'étudier l'importance de ses différentes composantes sur le mécanisme d'ancrage. Différents travaux avaient examiné les effets de l'architecture mais sur des systèmes théoriques peu représentatifs de l'architecture d'un arbre sensible au chablis. Le chapitre 3 montre le rôle essentiel joué par le pivot et les racines traçantes. Ce résultat confirme de nombreuses études expérimentales et théoriques, et pour la première fois permet de quantifier ces effets. Cette approche basée sur une maquette numérique ouvre des perspectives vers une simplification du modèle d'ancrage en proposant un nombre réduit de paramètres architecturaux pertinents pour la mécanique de l'ancrage, et aussi sur une simplification des mesures de systèmes racinaires dont on souhaite déterminer la résistance à la verse ou au chablis. Cette étude des effets architecturaux a été complétée par une analyse de sensibilité aux paramètres géométriques et mécaniques des racines et du sol (chapitre 4). Conformément à la mécanique classique des poutres, on retrouve que les effets des propriétés mécaniques du sol et des racines sont inférieurs à ceux des paramètres géométriques. Et si l'on compare les études du chapitre 3 et 4, on trouve que les effets architecturaux sont dominants par rapport à ceux des propriétés des racines et du sol. Ainsi la suppression d'un pivot réduit de 61% le moment critique contre 15% pour une variation de 20% de la longueur du pivot. Ces résultats viennent ainsi établir et quantifier ces effets sur la base d'un modèle mécanique confirmant des connaissances jusque-là empiriques. Cette thèse a donc permis de tracer des lignes conductrices pour à l'avenir simplifier et paramétrer de façon judicieuse le modèle afin d'étendre son utilisation à d'autres espèces et d'autres conditions de sol et différentes pratiques sylvicoles.

Au terme de ce travail, trois points principaux nous semblent devoir être revisités dans des perspectives à court terme. Le premier concerne la modélisation du sol. Nous avons considéré un milieu comme homogène. Or les hétérogénéités du sol (horizon induré, nappe phréatique, densité variable) doivent jouer un rôle non négligeable dans la résistance du système sol-racine. Cela suppose de discrétiser les propriétés du sol et d'introduire l'effet de la teneur en eau, soit en couplant contrainte et succion, soit plus simplement en paramétrant les propriétés du sol en fonction de la teneur en eau. On pourra utiliser ce type de développements pour examiner les effets dus au sol qui dans une approche homogène sont faibles. Le second point qui nous semble important d'examiner est les effets liés à des sollicitations dynamiques. En effet, le

modèle actuel traite des déformations statiques, or la réponse du sol et la fatigue du système racinaire sous chargement cyclique et dynamique par les rafales de vent pourraient induire des comportements spécifiques qu'une approche statique ne permet pas de révéler.

Pour compléter, le modèle de rupture choisi pour les racines devrait mieux rendre compte des lois de comportement observées pour du bois vert. Il est en effet connu que les comportements à la rupture, en particulier dans la direction des fibres pour l'utilisation d'éléments de poutres en FEM, sont différents en tension (rupture fragile) et en compression (rupture ductile). D'autre part les ruptures en flexion sont essentiellement dues à une délamination des fibres, ce qui doit amener à une modélisation spécifique de ce mode.

Il nous semble que ces développements du modèle ne devront pas se faire au détriment de son utilisation et au prix d'un paramétrage lourd et difficile à mettre en œuvre. En effet, l'objectif à plus long terme des développements du modèle est son application à la gestion du risque de chablis en forêt. Ce modèle FEM doit permettre de résoudre des questions finalisées pour lesquelles une approche expérimentale est très difficile à mettre en œuvre. Parmi ces applications on peut citer (i) le développement d'une méthode de diagnostic non destructive de sensibilité au chablis *in situ* et (ii) l'évaluation de l'impact de pratiques sylvicoles sur le risque de chablis. Sur le premier point il s'agit d'appliquer le modèle dans des contextes où l'information est réduite et d'évaluer la capacité du modèle à prévoir l'occurrence de chablis. Les informations réduites peuvent être par exemple un écart à la verticalité du tronc mesurée sur le terrain ou des mesures non destructives de la résistance en flexion élastique de l'arbre (racines, tronc). Le deuxième point concerne l'utilisation du modèle pour simuler différentes pratiques sylvicoles relatives aux sols (labour, débroussaillage avec endommagement des racines superficielles...). Ces pratiques induisent des modifications du système racinaire et de la structure du sol dont on connait encore très mal l'impact sur le risque au chablis.

Bibliographie

Abernethy, B. and Rutherfurd, I. D. The distribution and strength of riparian tree roots in relation to riverbank reinforcement. *Hydrological processes*, 15(1) :63–79, 2001.

Achim, A. and Nicoll, B. C. Modelling the anchorage of shallow-rooted trees. *Forestry*, page cpp004, 2009.

Ancelin, P., Courbaud, B., and Fourcaud, T. Development of an individual tree-based mechanical model to predict wind damage within forest stands. *Forest ecology and management*, 203 (1) :101–121, 2004.

Anderson, C., Coutts, M., Ritchie, R., and Campbell, D. Root extraction force measurements for sitka spruce. *Forestry*, 62(2) :127–137, 1989.

Bardet, J.-P. Experimental soil mechanics. 1997.

Barthélémy, D. and Caraglio, Y. Plant architecture : a dynamic, multilevel and comprehensive approach to plant form, structure and ontogeny. *Annals of botany*, 99(3) :375–407, 2007.

Bengough, A. G., Bransby, M. F., Hans, J., McKenna, S. J., Roberts, T. J., and Valentine, T. A. Root responses to soil physical conditions ; growth dynamics from field to cell. *Journal of Experimental Botany*, 57(2) :437–447, 2006.

Bengough, A. a. and Mullins, C. Mechanical impedance to root growth : a review of experimental techniques and root growth responses. *Journal of soil science*, 41(3) :341–358, 1990.

Bert, D. and Danjon, F. Carbon concentration variations in the roots, stem and crown of mature pinus pinaster (ait.). *Forest Ecology and Management*, 222(1-3) :279–295, FEB 15 2006. ISSN 0378-1127. doi : 10.1016/j.foreco.2005.10.030.

Blackwell, P., Rennolls, K., and Coutts, M. A root anchorage model for shallowly rooted sitka spruce. *Forestry*, 63(1) :73–91, 1990.

Blennow, K. and Sallnäs, O. Winda - a system of models for assessing the probability of wind damage to forest stands within a landscape. *Ecological Modelling*, 175(1) :87–99, 2004.

Bourrier, F., Kneib, F., Chareyre, B., and Fourcaud, T. Discrete modeling of granular soils reinforcement by plant roots. *Ecological Engineering*, 61 :646–657, 2013.

Braam, J. In touch : plant responses to mechanical stimuli. *New Phytologist*, 165(2) :373–389, 2005.

Bradshaw, W. E. and Holzapfel, C. M. Evolutionary response to rapid climate change. *Science(Washington)*, 312(5779) :1477–1478, 2006.

Burbidge, N. T. Root development in pinus pinaster and the seasonal variation of its mycorrhizae. *Australian Forestry*, 1(1) :33–40, 1936.

Busgen, M., Munch, E., and Thomson, T. *The structure and life of forest trees*. Chapman & Hall, 1929.

Cairns, M. A., Brown, S., Helmer, E. H., and Baumgardner, G. A. Root biomass allocation in the world's upland forests. *Oecologia*, 111(1) :1–11, 1997.

Chazdon, R. L. Beyond deforestation : restoring forests and ecosystem services on degraded lands. *science*, 320(5882) :1458–1460, 2008.

Commandeur, P. R. and Pyles, M. R. Modulus of elasticity and tensile strength of douglas-fir roots. *Canadian journal of forest research*, 21(1) :48–52, 1991.

Coutts, M. Root architecture and tree stability. *Plant and Soil*, 71(1-3) :171–188, 1983.

Coutts, M. Components of tree stability in sitka spruce on peaty gley soil. *Forestry*, 59(2) : 173–197, 1986.

Coutts, M. and Lewis, G. When is the structural root system determined in sitka spruce ? *Plant and Soil*, 71(1-3) :155–160, 1983.

Coutts, M., Walker, C., and Burnand, A. Effects of establishment method on root form of lodgepole pine and sitka spruce and on the production of adventitious roots. *Forestry*, 63(2) : 143–159, 1990.

Coutts, M., Nielsen, C., and Nicoll, B. The development of symmetry, rigidity and anchorage in the structural root system of conifers. *Plant and Soil*, 217(1-2) :1–15, 1999.

Crook, M. and Ennos, A. The anchorage mechanics of deep rooted larch, larix europea× l. japonica. *Journal of Experimental Botany*, 47(10) :1509–1517, 1996.

Crook, M., Ennos, A., and Banks, J. The function of buttress roots : a comparative study of the anchorage systems of buttressed (aglaia and nephelium ramboutan species) and non-buttressed (mallotus wrayi) tropical trees. *Journal of Experimental Botany*, 48(9) : 1703–1716, 1997.

Cucchi, V., Meredieu, C., Stokes, A., Berthier, S., Bert, D., Najar, M., Denis, A., and Lastennet, R. Root anchorage of inner and edge trees in stands of maritime pine (pinus pinaster ait.) growing in different podzolic soil conditions. *Trees-Structure and Function*, 18(4) :460–466, JUL 2004. ISSN 0931-1890. doi : 10.1007/s00468-004-0330-2.

Cucchi, V. *Sensibilité au vent des peuplements de pin maritime (Pinus pinaster Ait.)*. PhD thesis, 2004.

Cucchi, V. and Bert, D. Wind-firmness in pinus pinaster ait. stands in southwest france : influence of stand density, fertilisation and breeding in two experimental stands damaged during the 1999 storm. *Annals of Forest Science*, 60(3) :209–226, 2003.

Czarnes, S., Hallett, P., Bengough, A., and Young, I. Root-and microbial-derived mucilages affect soil structure and water transport. *European Journal of Soil Science*, 51(3) :435–443, 2000.

Danjon, F., Bert, D., Godin, C., and Trichet, P. Structural root architecture of 5-year-old pinus pinaster measured by 3d digitising and analysed with amapmod. *Plant and Soil*, 217(1-2) : 49–63, 1999a. ISSN 0032-079X.

Danjon, F., Sinoquet, H., Godin, C., Colin, F., and Drexhage, M. Characterisation of structural tree root architecture using 3d digitising and amapmod software. *Plant and Soil*, 211(2) : 241–258, 1999b. ISSN 0032-079X.

Danjon, F., Fourcaud, T., and Bert, D. Root architecture and wind-firmness of mature pinus pinaster. *New Phytologist*, 168(2) :387–400, NOV 2005. ISSN 0028-646X. doi : 10.1111/j.1469-8137.2005.01497.x.

Danjon, F., Drnou, C., Dupuy, L., and Lebourgeois, F. Racines, sol mcanique de l'ancrage de l'arbre et stabilit. *La fort face aux temptes. Coll. Synthses, Quae Editions. Paris*, page 155, 2009.

Danjon, F., Caplan, J. S., Fortin, M., and Meredieu, C. Descendant root volume varies as a function of root type : estimation of root biomass lost during uprooting in pinus pinaster. *Frontiers in Plant Science*, 4(402), 2013a. ISSN 1664-462X. doi : 10.3389/fpls.2013.00402. URL http://www.frontiersin.org/functional_plant_ecology/10.3389/fpls.2013.00402/abstract.

Danjon, F., Khuder, H., and Stokes, A. Deep phenotyping of coarse root architecture in r. pseudoacacia reveals that tree root system plasticity is confined within its architectural model. *PLoS ONE*, 8(12) :e83548, 12 2013b. doi : 10.1371/journal.pone.0083548. URL http://dx.doi.org/10.1371%2Fjournal.pone.0083548.

Danjon, F. and Reubens, B. Assessing and analyzing 3d architecture of woody root systems, a review of methods and applications in tree and soil stability, resource acquisition and allocation. *Plant and Soil*, 303(1-2) :1–34, 2008.

de Coligny, F., Ancelin, P., Cornu, G., Courbaud, B., Dreyfus, P., Goreaud, F., Gourlet-Fleury, S., Meredieu, C., Orazio, C., and Saint-André, L. Capsis : Computer-aided projection for strategies in silviculture : Open architecture for a shared forest-modelling platform. In *Proceedings of the IUFRO Working Party S*, volume 5, pages 01–04, 2004.

Deans, J. Dynamics of coarse root production in a young plantation of picea sitchensis. *Forestry*, 54(2) :139–155, 1981.

Défossez, P., Cointe, A., Coureau, J.-L., Morel, S., Bonnefond, J.-M., Garrigou, D., Lambrot, C., Danjon, F., and Fourcaud, T. Propriétés mécaniques des racines de structure de pinus pinaster. In *Journées scientifiques du GDR3544 Sciences du Bois*, 2014.

Della-Marta, P. M. and Pinto, J. G. Statistical uncertainty of changes in winter storms over the north atlantic and europe in an ensemble of transient climate simulations. *Geophysical Research Letters*, 36(14), 2009.

Di Iorio, A., Lasserre, B., Petrozzi, L., Scippa, G. S., and Chiatante, D. Adaptive longitudinal growth of first-order lateral roots of a woody species (spartium junceum) to slope and different soil conditions ?upward growth of surface roots. *Environmental and experimental botany*, 63(1) :207–215, 2008.

Dietrich, R., Bengough, A., Jones, H., and White, P. Can root electrical capacitance be used to predict root mass in soil ? *Annals of botany*, 112(2) :457–464, 2013.

Dlouha, J. *Comportement viscoélastique longitudinal du bois vert : diversité et prdiction long terme*. PhD thesis, Université Montpellier II-Sciences et Techniques du Languedoc, 2009.

Dourado, N., Morel, S., De Moura, M., Valentin, G., and Morais, J. Comparison of fracture properties of two wood species through cohesive crack simulations. *Composites Part A : applied science and manufacturing*, 39(2) :415–427, 2008.

Dupont, S. and Brunet, Y. Edge flow and canopy structure : A large-eddy simulation study. *Boundary-Layer Meteorology*, 126(1) :51–71, 2008. ISSN 0006-8314. doi : 10.1007/s10546-007-9216-3. URL http://dx.doi.org/10.1007/s10546-007-9216-3.

Dupuy, L., Fourcaud, T., and Stokes, A. A numerical investigation into factors affecting the anchorage of roots in tension. *European Journal of Soil Science*, 56(3) :319–327, JUN 2005a. ISSN 1351-0754. doi : 10.1111/j.1365-2389.2004.00666.x.

Dupuy, L., Fourcaud, T., and Stokes, A. A numerical investigation into the influence of soil type and root architecture on tree anchorage. *Plant and Soil*, 278(1-2) :119–134, DEC 2005b. ISSN 0032-079X. doi : 10.1007/s11104-005-7577-2.

Dupuy, L. X., Fourcaud, T., Lac, P., and Stokes, A. A generic 3d finite element model of tree anchorage integrating soil mechanics and real root system architecture. *American Journal of Botany*, 94(9) :1506–1514, SEP 2007. ISSN 0002-9122.

Ennnos, A. R. The anchorage of leek seedlings : the effect of root length and soil strength. *Annals of Botany*, 65(4) :409–416, 1990.

Ennos, A. R. The mechanics of anchorage in seedlings of sunflower, helianthus annuus l. *New Phytologist*, 113(2) :185–192, 1989.

Ennos, A., Crook, M., and Grimshaw, C. A comparative study of the anchorage systems of himalayan balsam impatiens glandulifera and mature sunflower helianthus annuus. *Journal of Experimental Botany*, 44(1) :133–146, 1993.

Ennos, R. *Trees*. Smithsonian, Bruxelles, 2001.

Fitter, A. Architecture and biomass allocation as components of the plastic response of root systems to soil heterogeneity. *Exploitation of environmental heterogeneity by plants*, pages 305–323, 1994.

Follrich, J., Müller, U., and Gindl, W. Effects of thermal modification on the adhesion between spruce wood (picea abies karst.) and a thermoplastic polymer. *Holz als Roh-und Werkstoff*, 64(5) :373–376, 2006.

Fourcaud, T., Blaise, F., Lac, P., Castéra, P., and de Reffye, P. Numerical modelling of shape regulation and growth stresses in trees. *Trees*, 17(1) :31–39, 2003.

Fourcaud, T., Ji, J.-N., Zhang, Z.-Q., and Stokes, A. Understanding the impact of root morphology on overturning mechanisms : A modelling approach. *Annals of Botany*, 101(8) : 1267–1280, MAY 2008. ISSN 0305-7364. doi : 10.1093/aob/mcm245.

Fournier, M. Modélisation mécanique des vibrations propres d'un arbre soumis aux vents, en fonction de sa morphologie. *Ann. Sci. For.*, 50 :401–412, 1993.

Fournier, M., Dlouhà, J., Jaouen, G., and Almeras, T. Integrative biomechanics for tree ecology : beyond wood density and strength. *Journal of experimental botany*, page ert279, 2013.

Fraser, A. The soil and roots as factors in tree stability. *Forestry*, 35(2) :117–127, 1962.

Fredlund, D., Morgenstern, N., and Widger, R. The shear strength of unsaturated soils. *Canadian Geotechnical Journal*, 15(3) :313–321, 1978.

Gan, J., Fredlund, D., and Rahardjo, H. Determination of the shear strength parameters of an unsaturated soil using the direct shear test. *Canadian Geotechnical Journal*, 25(3) :500–510, 1988.

Gandhi, K. J., Gilmore, D. W., Katovich, S. A., Mattson, W. J., Zasada, J. C., and Seybold, S. J. Catastrophic windstorm and fuel-reduction treatments alter ground beetle (coleoptera : Carabidae) assemblages in a north american sub-boreal forest. *Forest Ecology and Management*, 256(5) :1104–1123, 2008.

Gardiner, B., Peltola, H., and Kellomaki, S. Comparison of two models for predicting the critical wind speeds required to damage coniferous trees. *Ecological Modelling*, 129(1) : 1–23, MAY 3 2000. ISSN 0304-3800.

Gardiner, B., Byrne, K., Hale, S., Kamimura, K., Mitchell, S. J., Peltola, H., and Ruel, J.-C. A review of mechanistic modelling of wind damage risk to forests. *Forestry*, 81(3) :447–463, 2008. doi : 10.1093/forestry/cpn022. URL http://forestry.oxfordjournals.org/content/81/3/447.abstract.

Gardiner, B., Blennow, K., Carnus, J.-M., Fleischer, P., Ingemarson, F., Landmann, G., Lindner, M., Marzano, M., Nicoll, B., Orazio, C., Peyron, J.-L., Reviron, M.-P., Schelhaas, M.-J., Schuck, A., Spielmann, M., and Usbeck, T. *Destructive Storms in European Forests : Past and Forthcoming Impacts*. EFIatlantic, Bruxelles, 2010.

Genet, M., Stokes, A., Salin, F., Mickovski, S., Fourcaud, T., Dumail, J., and van Beek, R. The influence of cellulose content on tensile strength in tree roots. *Plant and Soil*, 278(1-2) :1–9, DEC 2005. ISSN 0032-079X. doi : 10.1007/s11104-005-8768-6.

Ghani, M. A., Stokes, A., and Fourcaud, T. The effect of root architecture and root loss through trenching on the anchorage of tropical urban trees (eugenia grandis wight). *Trees*, 23(2) : 197–209, 2009.

Gifford, R. M. *Carbon content of woody roots : revised analysis and a comparison with woody shoot components*. Australian Greenhouse Office, 2000.

Godin, C. and Caraglio, Y. A multiscale model of plant topological structures. *Journal of theoretical biology*, 191(1) :1–46, 1998.

Godin, C., Costes, E., and Sinoquet, H. A method for describing plant architecture which integrates topology and geometry. *Annals of botany*, 84(3) :343–357, 1999.

Griffon, S. and de Coligny, F. Amapstudio : an editing and simulation software suite for plants architecture modelling. *Ecological Modelling*, 290 :3–10, 2014.

Hendrick, E. The effect of cultivation method on the growth and root anchorage of sitka spruce. *Irish Forestry*, 46(1) :19–28, 1989.

Hendrick, R. L. and Pregitzer, K. S. The dynamics of fine root length, biomass, and nitrogen content in two northern hardwood ecosystems. *Canadian Journal of Forest Research*, 23 (12) :2507–2520, 1993. doi : 10.1139/x93-312. URL http://dx.doi.org/10.1139/x93-312.

Hibbitt, D., Karlsson, B., and Sorensen, P. Abaqus analysis user ?s manual. *Pawtucket, USA*, 2013.

James, K. R., Haritos, N., and Ades, P. K. Mechanical stability of trees under dynamic loads. *American Journal of Botany*, 93(10) :1522–1530, OCT 2006. ISSN 0002-9122.

Ji, J., Kokutse, N., Genet, M., Fourcaud, T., and Zhang, Z. Effect of spatial variation of tree root characteristics on slope stability. a case study on black locust (robinia pseudoacacia) and arborvitae (platycladus orientalis) stands on the loess plateau, china. *Catena*, 92 :139–154, 2012.

Jonsson, M., Foetzki, A., Kalberer, M., Lundström, T., Ammann, W., and Stöckli, V. Root-soil rotation stiffness of norway spruce (picea abies (l.) karst) growing on subalpine forested slopes. *Plant and Soil*, 285(1-2) :267–277, 2006.

Kamimura, K., Saito, S., Kinoshita, H., Kitagawa, K., Uchida, T., and Mizunaga, H. Analysis of wind damage caused by multiple tropical storm events in japanese cryptomeria japonica forests. *Forestry*, page cpt011, 2013.

Keller, T. and Hakansson, I. Estimation of reference bulk density from soil particle size distribution and soil organic matter content. *Geoderma*, 154(3) :398–406, 2010.

Khuder, H., Stokes, A., Danjon, F., Gouskou, K., and Lagane, F. Is it possible to manipulate root anchorage in young trees ? *Plant and Soil*, 294(1-2) :87–102, MAY 2007. ISSN 0032-079X. doi : 10.1007/s11104-007-9232-6.

Kostler, J. N., Bruckner, E., and Bibelriether, H. Die wurzeln der waldbaume. *Untersuchungen zur Morphologie der Waldbaume in Mitteleuropa. Verlag Paul Parey : Hamburg & Berlin*, 284 :3–4, 1968.

Krajcinovic, D. *Damage mechanics*, volume 41. Elsevier, 1996.

Kretschmann, D. E. *Wood Handbook, Wood as an Engineering Material*, pages 5.1–5.46. Madison, WI : U.S. Department of Agriculture, Forest Service, Forest Products Laboratory, 2010.

Linde, P., Pleitner, J., de Boer, H., and Carmone, C. Modelling and simulation of fibre metal laminates. In *2004 ABAQUS Users' Conference*, pages 421–439, 2004.

Lundström, T., Jonas, T., Stöckli, V., and Ammann, W. Anchorage of mature conifers : resistive turning moment, root–soil plate geometry and root growth orientation. *Tree Physiology*, 27 (9) :1217–1227, 2007.

Lynch, J. P. Root phenes for enhanced soil exploration and phosphorus acquisition : tools for future crops. *Plant Physiology*, 156(3) :1041–1049, 2011.

Lynch, J. P. and Brown, K. M. Topsoil foraging–an architectural adaptation of plants to low phosphorus availability. *Plant and Soil*, 237(2) :225–237, 2001.

Mao, Z., Bonis, M., Rey, H., Saint-Andr, L., Stokes, A., and Jourdan, C. Which processes drive fine root elongation in a natural forest ecosystem ? *Plant Ecology & Diversity*, Accepted, 2012a.

Mao, Z., Saint-André, L., Genet, M., Mine, F.-X., Jourdan, C., Rey, H., Courbaud, B., and Stokes, A. Engineering ecological protection against landslides in diverse mountain forests : choosing cohesion models. *Ecological Engineering*, 45 :55–69, 2012b.

Mao, Z., Yang, M., Bourrier, F., and Fourcaud, T. Evaluation of root reinforcement models using numerical modelling approaches. *Plant and Soil*, pages 1–22, 2014.

Mason, E. Causes of juvenile instability of pinus radiata in new zealand. *New Zealand Journal of Forest Science*, 15 :263–280, 1985.

McCarthy, J., Hood, I., Brockerhoff, E., Carlson, C., Pawson, S., Forward, M., Walbert, K., and Gardner, J. Predicting sapstain and degrade in fallen trees following storm damage in a pinus radiata forest. *Forest ecology and management*, 260(9) :1456–1466, 2010.

Mickovski, S. B. and Ennos, A. R. The effect of unidirectional stem flexing on shoot and root morphology and architecture in young pinus sylvestris trees. *Canadian Journal of Forest Research*, 33(11) :2202–2209, 2003.

Mickovski, S. B. and Ennos, R. A. A morphological and mechanical study of the root systems of suppressed crown scots pine pinus sylvestris. *Trees*, 16(4-5) :274–280, 2002.

Mickovski, S. B., Stokes, A., Van Beek, R., Ghestem, M., and Fourcaud, T. Simulation of direct shear tests on rooted and non-rooted soil using finite element analysis. *Ecological Engineering*, 37(10) :1523–1532, 2011.

Mooney, S., Pridmore, T., Helliwell, J., and Bennett, M. Developing x-ray computed tomography to non-invasively image 3-d root systems architecture in soil. *Plant and Soil*, 352(1-2) : 1–22, 2012.

Moore, J. R. Differences in maximum resistive bending moments of pinus radiata trees grown on a range of soil types. *Forest Ecology and Management*, 135(1) :63–71, 2000.

Moore, J. R. and Maguire, D. A. Natural sway frequencies and damping ratios of trees : concepts, review and synthesis of previous studies. *Trees*, 18(2) :195–203, 2004.

Moore, J. R. and Maguire, D. A. Simulating the dynamic behavior of douglas-fir trees under applied loads by the finite element method. *Tree physiology*, 28(1) :75–83, 2008.

Moulia, B. Plant biomechanics and mechanobiology are convergent paths to flourishing interdisciplinary research. *Journal of experimental botany*, 64(15) :4617–4633, 2013.

Murakami, S. *Continuum damage mechanics : a continuum mechanics approach to the analysis of damage and fracture*, volume 185. Springer, 2012.

Neild, S. and Wood, C. Estimating stem and root-anchorage flexibility in trees. *Tree physiology*, 19(3) :141–151, 1999.

Nicoll, B. C. and Ray, D. Adaptive growth of tree root systems in response to wind action and site conditions. *Tree physiology*, 16(11-12) :891–898, 1996.

Nicoll, B. C., Gardiner, B. A., Rayner, B., and Peace, A. J. Anchorage of coniferous trees in relation to species, soil type, and rooting depth. *Canadian Journal of Forest Research*, 36 (7) :1871–1883, 2006.

Nicoll, B. C., Gardiner, B. A., and Peace, A. J. Improvements in anchorage provided by the acclimation of forest trees to wind stress. *Forestry*, 81(3) :389–398, 2008.

Niklas, K. J. and Spatz, H.-C. Worldwide correlations of mechanical properties and green wood density. *American Journal of Botany*, 97(10) :1587–1594, 2010.

Niklas, K. Variations of the mechanical properties of acer saccharum roots. *Journal of Experimental Botany*, 50(331) :193–200, 1999.

Passioura, J. Soil conditions and plant growth. *Plant, cell & environment*, 25(2) :311–318, 2002.

Peltola, H., Kellomaki, S., Vaisanen, H., and Ikonen, V.-P. A mechanistic model for assessing the risk of wind and snow damage to single trees and stands of scots pine, norway spruce, and birch. *Canadian Journal of Forest Research*, 29(6) :647–661, 1999.

Pivato, D., Dupont, S., and Brunet, Y. A simple tree swaying model for forest motion in windstorm conditions. *Trees*, 28(1) :281–293, 2014. ISSN 0931-1890. doi : 10.1007/s00468-013-0948-z. URL http://dx.doi.org/10.1007/s00468-013-0948-z.

Pollen, N. Temporal and spatial variability in root reinforcement of streambanks : accounting for soil shear strength and moisture. *Catena*, 69(3) :197–205, 2007.

Pollen, N. and Simon, A. Estimating the mechanical effects of riparian vegetation on stream bank stability using a fiber bundle model. *Water Resources Research*, 41(7), 2005.

Pollen, N., Simon, A., and Collison, A. Advances in assessing the mechanical and hydrologic effects of riparian vegetation on streambank stability. *Riparian vegetation and fluvial geomorphology*, pages 125–139, 2004.

Quine, C. Assessing the risk of wind damage to forests : practice and pitfalls. *Wind and Trees. Cambridge University Press, Cambridge*, pages 379–403, 1995.

Quine, C., Burnand, A., Coutts, M., and Reynard, B. Effects of mounds and stumps on the root architecture of sitka spruce on a peaty gley restocking site. *Forestry*, 64(4) :385–401, 1991.

Rahardjo, H., Harnas, F., Leong, E. C., Tan, P.-Y., Fong, Y.-K., and Sim, E. Tree stability in an improved soil to withstand wind loading. *Urban Forestry & Urban Greening*, 8(4) :237–247, 2009.

Ray, D. and Nicoll, B. C. The effect of soil water-table depth on root-plate development and stability of sitka spruce. *Forestry*, 71(2) :169–182, 1998.

Read, D., Bengough, A., Gregory, P., Crawford, J. W., Robinson, D., Scrimgeour, C., Young, I. M., Zhang, K., and Zhang, X. Plant roots release phospholipid surfactants that modify the physical and chemical properties of soil. *New phytologist*, 157(2) :315–326, 2003.

Reubens, B., Poesen, J., Danjon, F., Geudens, G., and Muys, B. The role of fine and coarse roots in shallow slope stability and soil erosion control with a focus on root system architecture : a review. *Trees*, 21(4) :385–402, 2007.

Riestenberg, M. M. *Anchoring of thin colluvium by roots of sugar maple and white ash on hillslopes in Cincinnati*. US Government Printing Office, 1994.

Ristova, D., Rosas, U., Krouk, G., Ruffel, S., Birnbaum, K. D., and Coruzzi, G. M. Rootscape : a landmark-based system for rapid screening of root architecture in arabidopsis. *Plant physiology*, 161(3) :1086–1096, 2013.

Rodriguez, M., de Langre, E., and Moulia, B. A scaling law for the effects of architecture and allometry on tree vibration modes suggests a biological tuning to modal compartmentalization. *American Journal of Botany*, 95(12) :1523–1537, 2008.

Saffih-Hdadi, K., Défossez, P., Richard, G., Cui, Y.-J., Tang, A.-M., and Chaplain, V. A method for predicting soil susceptibility to the compaction of surface layers as a function of water content and bulk density. *Soil and Tillage Research*, 105(1) :96–103, 2009.

Savill, P. The effects of drainage and ploughing of surface water gleys on rooting and windthrow of sitka spruce in northern ireland. *Forestry*, 49(2) :133–141, 1976.

Schelhaas, M.-J., Nabuurs, G.-J., and Schuck, A. Natural disturbances in the european forests in the 19th and 20th centuries. *Global Change Biology*, 9(11) :1620–1633, 2003. ISSN 1365-2486. doi : 10.1046/j.1365-2486.2003.00684.x. URL http://dx.doi.org/10.1046/j.1365-2486.2003.00684.x.

Schelhaas, M., Kramer, K., Peltola, H., Van der Werf, D., and Wijdeven, S. Introducing tree interactions in wind damage simulation. *Ecological Modelling*, 207(2) :197–209, 2007.

Schwarz, M., Lehmann, P., and Or, D. Quantifying lateral root reinforcement in steep slopes–from a bundle of roots to tree stands. *Earth Surface Processes and Landforms*, 35(3) : 354–367, 2010.

Schwarz, M., Cohen, D., and Or, D. Pullout tests of root analogs and natural root bundles in soil : Experiments and modeling. *Journal of Geophysical Research : Earth Surface (2003–2012)*, 116(F2), 2011.

Schwarz, M., Cohen, D., and Or, D. Spatial characterization of root reinforcement at stand scale : Theory and case study. *Geomorphology*, 171 :190–200, 2012.

Schwarz, M., Giadrossich, F., and Cohen, D. Modeling root reinforcement using a root-failure weibull survival function. *Hydrology and Earth System Sciences*, 17(11) :4367–4377, 2013.

Sellier, D. and Fourcaud, T. Crown structure and wood properties : influence on tree sway and response to high winds. *American Journal of Botany*, 96(5) :885–896, MAY 2009. ISSN 0002-9122. doi : 10.3732/ajb.0800226.

Sellier, D., Fourcaud, T., and Lac, P. A finite element model for investigating effects of aerial architecture on tree oscillations. *Tree Physiology*, 26(6) :799–806, 2006.

Sellier, D., Brunet, Y., and Fourcaud, T. A numerical model of tree aerodynamic response to a turbulent airflow. *Forestry*, 81(3) :279–297, JUL 2008. ISSN 0015-752X.

Sinoquet, H. and Rivet, P. Measurement and visualization of the architecture of an adult tree based on a three-dimensional digitising device. *Trees*, 11(5) :265–270, 1997.

Sinoquet, H., Rivet, P., Godin, C., et al. Assessment of the three-dimensional architecture of walnut trees using digitising. 1997.

Smith, J. E., Heath, L. S., Skog, K. E., Birdsey, R. A., et al. Methods for calculating forest ecosystem and harvested carbon with standard estimates for forest types of the united states. 2006.

Stokes, A. Strain distribution during anchorage failure of pinus pinaster ait. at different ages and tree growth response to wind-induced root movement. *Plant and Soil*, 217(1-2) :17–27, 1999. ISSN 0032-079X.

Stokes, A. and Mattheck, C. Variation of wood strength in tree roots. *Journal of Experimental Botany*, 47(298) :693–699, MAY 1996. ISSN 0022-0957. doi : 10.1093/jxb/47.5.693.

Stokes, A., Nicoll, B., Coutts, M., and Fitter, A. Responses of young sitka spruce clones to mechanical perturbation and nutrition : effects on biomass allocation, root development, and resistance to bending. *Canadian Journal of Forest Research*, 27(7) :1049–1057, JUL 1997a. ISSN 0045-5067.

Stokes, A., Berthier, S., Sacriste, S., and Martin, F. Variations in maturation strains and root shape in root systems of maritime pine (pinus pinaster ait.). *TREES-STRUCTURE AND FUNCTION*, 12(6) :334–339, MAY 1998. ISSN 0931-1890.

Stokes, A., Fitter, A., and Courts, M. Responses of young trees to wind and shading : effects on root architecture. *Journal of Experimental Botany*, 46(9) :1139–1146, 1995.

Stokes, A., Martin, F., Sacriste, S., and Fourcaud, T. Adaptation of tree roots to wind loading ?the relationship between mechanical behaviour and wood formation. In *Plant biomechanics (conference proceedings I, papers). Centre for Biomimetics, University of Reading*, pages 339–346, 1997b.

Sultan, S. E. Phenotypic plasticity for plant development, function and life history. *Trends in plant science*, 5(12) :537–542, 2000.

Szoradova, A., Praus, L., and Kolarik, J. Evaluation of the root system resistance against failure of urban trees using principal component analysis. *Biosystems Engineering*, 115(3) : 244–249, 2013.

Tamasi, E., Stokes, A., Lasserre, B., Danjon, F., Berthier, S., Fourcaud, T., and Chiatante, D. Influence of wind loading on root system development and architecture in oak (quercus robur l.) seedlings. *Trees*, 19(4) :374–384, 2005.

Telewski, F. W. A unified hypothesis of mechanoperception in plants. *American Journal of Botany*, 93(10) :1466–1476, 2006.

Telewski, F. W. and Jaffe, M. J. Thigmomorphogenesis : field and laboratory studies of abies fraseri in response to wind or mechanical perturbation. *Physiologia Plantarum*, 66(2) : 211–218, 1986.

Timoshenko, S. *Strength of materials*, volume 1. D. Van Nostrand Company, inc., 1940.

Waldron, L. The shear resistance of root-permeated homogeneous and stratified soil. *Soil Science Society of America Journal*, 41(5) :843–849, 1977.

Waldron, L. and Dakessian, S. Soil reinforcement by roots : calculation of increased soil shear resistance from root properties. *Soil science*, 132(6) :427–435, 1981.

Wu, T. H., McKinnell III, W. P., and Swanston, D. N. Strength of tree roots and landslides on prince of wales island, alaska. *Canadian Geotechnical Journal*, 16(1) :19–33, 1979.

Wu, W. and Sidle, R. C. A distributed slope stability model for steep forested basins. *Water Resources Research*, 31(8) :2097–2110, 1995.

Wu, Y., Guo, L., Cui, X., Chen, J., Cao, X., and Lin, H. Ground-penetrating radar-based automatic reconstruction of three-dimensional coarse root system architecture. *Plant and Soil*, 383(1-2) :155–172, 2014.

Yang, M., Défossez, P., and Fourcaud, T. Improving finite element models of roots-soil mechanical interactions. In *Proceedings of the 7th International Conference on Functional-Structural Plant Models*, pages 204–206, 2013.

Yang, M., Défossez, P., Danjon, F., and Fourcaud, T. Tree stability under wind : simulating uprooting with root breakage using a finite element method. *Annals of botany*, page mcu122, 2014a.

Yang, M., Défossez, P., Danjon, F., and Fourcaud, T. Understanding tree root anchorage with the finite element method : a focus on the impact of root system morphology. In *IUFRO 2014 Wind and Trees International Conference*, 2014b.

Annexe A

Publication (Chapitre 2)

Annals of Botany Page 1 of 15
doi:10.1093/aob/mcu122, available online at www.aob.oxfordjournals.org

ANNALS OF BOTANY
Founded 1887

PART OF A SPECIAL ISSUE ON FUNCTIONAL–STRUCTURAL PLANT MODELLING

Tree stability under wind: simulating uprooting with root breakage using a finite element method

Ming Yang[1,2], Pauline Défossez[1,2,*], Frédéric Danjon[3,4] and Thierry Fourcaud[5]

[1]*INRA, UMR1391 ISPA, F-33140 Villenave d'Ornon, France,* [2]*Bordeaux Sciences Agro, UMR 1391 ISPA, F-33170 Gradignan, France,* [3]*INRA, UMR1202 BIOGECO, F-33610 Cestas, France,* [4]*Université de Bordeaux, UMR1202 BIOGECO, F-33610 Cestas, France and* [5]*CIRAD, UMR AMAP, Boulevard de la Lironde, F-34398 Montpellier Cedex 5, France*
** For correspondence. E-mail Pauline.Defossez@bordeaux.inra.fr*

Received: 20 December 2013 Returned for revision: 25 February 2014 Accepted: 28 April 2014

• **Background and Aims** Windstorms are the major natural hazard affecting European forests, causing tree damage and timber losses. Modelling tree anchorage mechanisms has progressed with advances in plant architectural modelling, but it is still limited in terms of estimation of anchorage strength. This paper aims to provide a new model for root anchorage, including the successive breakage of roots during uprooting.
• **Methods** The model was based on the finite element method. The breakage of individual roots was taken into account using a failure law derived from previous work carried out on fibre metal laminates. Soil mechanical plasticity was considered using the Mohr–Coulomb failure criterion. The mechanical model for roots was implemented in the numerical code ABAQUS using beam elements embedded in a soil block meshed with 3-D solid elements. The model was tested by simulating tree-pulling experiments previously carried out on a tree of *Pinus pinaster* (maritime pine). Soil mechanical parameters were obtained from laboratory tests. Root system architecture was digitized and imported into ABAQUS while root material properties were estimated from the literature.
• **Key Results** Numerical simulations of tree-pulling tests exhibited realistic successive root breakages during uprooting, which could be seen in the resulting response curves. Broken roots could be visually located within the root system at any stage of the simulations. The model allowed estimation of anchorage strength in terms of the critical turning moment and accumulated energy, which were in good agreement with *in situ* measurements.
• **Conclusions** This study provides the first model of tree anchorage strength for *P. pinaster* derived from the mechanical strength of individual roots. The generic nature of the model permits its further application to other tree species and soil conditions.

Key words: Tree anchorage, root mechanical properties, soil mechanical strength, failure modelling, functional–structural plant modelling, finite element method, ABAQUS, coarse root architecture, windthrow, *Pinus pinaster*, maritime pine.

INTRODUCTION

Windstorms are among the primary causes of destruction in forests (Gandhi *et al.*, 2008; McCarthy *et al.*, 2010). In particular, they are the major hazard affecting European forests, causing tree and timber losses. Moreover, reported wind-induced damage in Europe has increased since the last century due to forest expansion (Gardiner *et al.*, 2010). The increasing stock and average age of European forests and the observed ongoing climate changes, with the prediction of stronger windstorms (Della-Marta and Pinto, 2009), may also lead to a growing wind risk. For instance, storm Klaus, which hit southern Europe in January 2009, resulted in an estimated 43 000 000 m^3 of timber being blown down in southwest France, including a volume of 37 000 000 m^3 for *Pinus pinaster* (GPMF, 2011).

Numerous efforts have been made to model forest damage caused by wind (Gardiner *et al.*, 2008). They have led to several predictive models for forest damage (overturning, stem breakage), i.e. HWIND, GALES and FOREOLE (Peltola *et al.*, 1999; Gardiner *et al.*, 2000; Ancelin *et al.*, 2004). These models included empirical relationships to determine the tree's resistance to overturning based on tree-pulling tests. They are therefore are limited to the site conditions for which they were built (GALES and FOREOLE). Moreover, the resistance to overturning predicted by these empirical relationships used rough and simplified parameterization (HWIND).

Tree anchorage capacities vary with time and result from complex interactions between growing roots and their physical and biological environment. Previous observations and experimental studies have reported that part of root architecture plasticity is due to biomechanical acclimation when trees are subjected to wind loads (Stokes *et al.*, 1995; Nicoll and Ray, 1996; Coutts *et al.*, 1999; Tamasi *et al.*, 2005; Lundström *et al.*, 2007; Nicoll *et al.*, 2008; Danjon *et al.*, 2013). In particular, biomechanical acclimation of trees has been proved in the case of adult *P. pinaster* trees, for which asymmetrical patterns can play an important mechanical role in tree anchorage (Danjon *et al.*, 2005). In the context of global change it is very important for wind risk prediction models to take into account the ability of trees to develop stronger anchorage with specific root traits as a biomechanical response to the wind. We therefore have to provide a tool capable of predicting tree stability by taking into account the acclimation of root systems and changes in soil strength as a function of climate conditions. This requires progress in understanding the

uprooting process as a function of tree characteristics and soil material properties. The first studies on tree uprooting mechanisms were based on the experimental work of Coutts (1983, 1986), who also developed the first systematic method of analysing tree anchorage (Coutts, 1986). This author quantified the relative impacts of different anchorage components on Sitka spruce, i.e. root–soil weight, root material strength under tension and soil strength, on the overturning resistance of spruce. This method led to the first mechanistic model of tree anchorage (Blackwell *et al.*, 1990) that described the root anchorage strength in terms of these components. Understanding of the anchorage mechanism progressed with the use of numerical analysis and advances in plant architecture digitizing (Dupuy *et al.*, 2005*b*, 2007; Fourcaud *et al.*, 2008). This approach used the finite element method (FEM) to calculate the deformation of root–soil systems in three dimensions. Real and simulated root systems with their specific architectural properties were considered in the simulations. These analyses allowed comparison of the theoretical anchorage performances of different root types, i.e. tap-, herringbone-, heart- and plate-like root systems, in clay and sandy soils. In addition, Fourcaud *et al.* (2008) attempted to quantify the relative roles of root components, e.g. superficial laterals, deep roots and tap roots, in anchorage strength in different soil types using a simple 2-D FEM model. Rahardjo *et al.* (2009) developed a finite element model of root anchorage and used a parametric study to examine the influence of soil properties. Thus, numerical models have been used essentially to investigate the influence of root architecture on tree anchorage using theoretical parameters for soil and roots. Less is known about the failure mechanism, which is crucial for predicting the occurrence of uprooting. This implies to better understand the effect of soil–root friction, root strength and soil strength on the whole response of root systems involved in the overturning process.

Our paper has two objectives. Firstly it presents a new model of tree anchorage that simulates the root breakage mechanism during tree uprooting, and secondly it tests this model in comparison with a field experiment in the case of young *P. pinaster*, which has simpler root architecture than adult specimens. In the first section we present the basis of the model and the tree-pulling tests performed in the field. In the second section, we analyse the simulated response of the whole root system and compare it with measurements, and in the last section we discuss the model's capacity to simulate uprooting.

MATERIALS AND METHODS

Anchorage model

The FEM model presented here is based on the initial work by Dupuy *et al.* (2007) and uses the ABAQUS software, version 6.13 (http://www.3ds.com/products-services/simulia/portfolio/Abaqus/). The model is composed of three parts: (1) the parallelepiped soil domain; (2) the root system; and (3) a perfectly rigid stem used as a lever arm to mimic tree uprooting (Fig. 1). All relevant details not given here can be found in Dupuy *et al.* (2007). The vertical rigid stem was tied to the top of the stump of the root system; therefore, the stem base and the top of the stump always had the same displacement. The 3-D root architecture was modelled as an assemblage of discretized beams with a

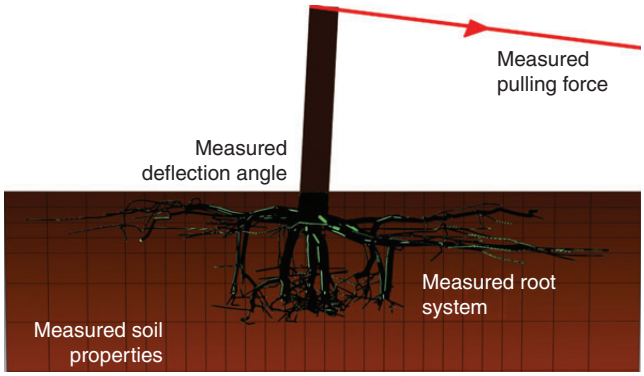

FIG. 1. Anchorage model with root system architecture and soil properties measured for tree-pulling simulations. Model outputs are the response curve of turning moment versus the deflection angle at the stem base and the total energy supplied by the pulling force. Deflection angle is defined as the angle between the vertical and the stem.

defined topology, branching pattern and geometry. It was imported in ABAQUS from the software Xplo (http://amapstudio.cirad.fr/soft/xplo/start; Griffon and de Coligny, 2013) dedicated to the encoding and visualization of plant architectures.

In this new model, the developments were focused on root–soil interaction, the mechanical behaviour of root material and the characteristics of the soil. Due to the complexity of meshing root architecture with 3-D solid elements, the roots were considered as embedded beam elements. We evaluated the relevance of this choice in a preliminary study carried out on a 3-D direct shear test of a soil block with root inclusions. Simulations considering roots modelled with embedded beam elements were compared with simulations using 3-D solid elements and root–soil interface friction properties (see Appendix). This study concluded that (1) the embedded beam elements mimicked the friction behaviour at the root–soil interface with a friction coefficient of ~0·1; and (2) for friction coefficients ranging from 0·1 to 0·9, the relative difference between the two approaches was always <21 % during the entire shear process. Embedded beam elements were then used in the anchorage model, implying that all the roots were slender structures embedded in the soil region. The roots were meshed with 3-D two-node linear Timoshenko beam elements with circular cross-sections (B31 in the ABAQUS element library).

The anchorage model described above allows the tree anchorage behaviour of various tree species to be modelled under different soil conditions. In our study, we chose a specific case of *P. pinaster* planted in sandy soil. The inputs of the model were: (1) a digitized root system of *P. pinaster* excavated after an *in situ* tree-pulling experiment; (2) soil properties from soil measurements in the laboratory; (3) root material properties from data taken from the literature, as described in the following sections. The model outputs were expressed by using response curves, i.e. 'turning moment' versus 'deflection angle at the stem base' and the energy supplied to the system during uprooting.

Formalism of individual root rupture. In the previous modelling work of Dupuy *et al.* (2007), the roots could only yield in the same way as metals, which exhibit plastic-like yielding, and the stresses remained stored in the roots after reaching the plasticity criterion. However, the roots were expected to exhibit brittle

behaviour in tension, with their cumulated stress released and redistributed to the remaining roots during the uprooting process. Such features have been repeatedly observed and modelled when considering soil reinforcement by fine roots with diameter generally <1 cm (Abernethy and Rutherfurd, 2001; Pollen and Simon, 2005; Pollen, 2007). Therefore, roots were modelled as brittle material in the present root anchorage model. An elastic failure law based on continuum damage mechanics was developed for roots under tension, compression and bending, based on previous constitutive laws regarding fibre metal laminates (Linde *et al.*, 2004). The law described by Linde *et al.* (2004) was adapted for wood beam elements and implemented in ABAQUS through the UMAT user subroutine.

In this model, roots are elastic in their initial state. During incremental loading, the damage initiation criterion is evaluated at each material point in every beam cross-section to detect the onset of damage. If the damage initiation criterion is reached, root stiffness degradation can be derived from the damage evolution law. The linear elastic behaviour defined in the beam cross-section axis is given by:

$$\begin{pmatrix} \sigma_{11}^{el} \\ \tau_{21}^{el} \\ \tau_{31}^{el} \end{pmatrix} = [\boldsymbol{C}] \begin{pmatrix} \varepsilon_{11}^{el} \\ \gamma_{21}^{el} \\ \gamma_{31}^{el} \end{pmatrix} \quad (1)$$

and

$$[\boldsymbol{C}] = \begin{bmatrix} E_r & 0 & 0 \\ 0 & G_r & 0 \\ 0 & 0 & G_r \end{bmatrix} \quad (2)$$

where σ_{11}^{el}, τ_{11}^{el} and τ_{21}^{el} represent the beam's elastic axial stress component and two elastic shear stress components along two perpendicular directions in the cross-section, respectively; E_r and G_r are modulus of elasticity and shear modulus, respectively; $[\boldsymbol{C}]$ is the non-degraded root stiffness tensor in its matrix form; and ε_{11}^{el}, γ_{21}^{el} and γ_{31}^{el} represent the axial strain component and two shear strain components, respectively. The damage initiation criterion f is defined in terms of ultimate tensile strain ε_{11}^{t}, ultimate compressive strain ε_{11}^{c} and actual strain ε_{11}. Damage onset occurs when fulfilling the criterion:

$$f = \sqrt{\frac{\varepsilon_{11}^{t}}{\varepsilon_{11}^{c}}(\varepsilon_{11})^2 + \left(\varepsilon_{11}^{t} - \frac{(\varepsilon_{11}^{t})^2}{\varepsilon_{11}^{c}}\right)\varepsilon_{11}} > \varepsilon_{11}^{t} \quad (3)$$

where

$$\varepsilon_{11}^{t} = \frac{\sigma_{11}^{t}}{E_r} \quad (4)$$

$$\varepsilon_{11}^{c} = \frac{\sigma_{11}^{c}}{E_r} \quad (5)$$

σ_{11}^{t} and σ_{11}^{c} being the tensile strength and compressive strength of the root material, respectively, and f is zero for axial strain ε_{11} ranging from 0 to $\varepsilon_{11}^{t} - \varepsilon_{11}^{c}$. Beyond this small interval it increases with increasing axial strain in both tensile and compressive directions. Figure 2A gives an example of the behaviour of $f - \varepsilon_{11}^{t}$ (using data SA5, Table 3). As long as the damage initiation criterion is reached, the damage variable d is

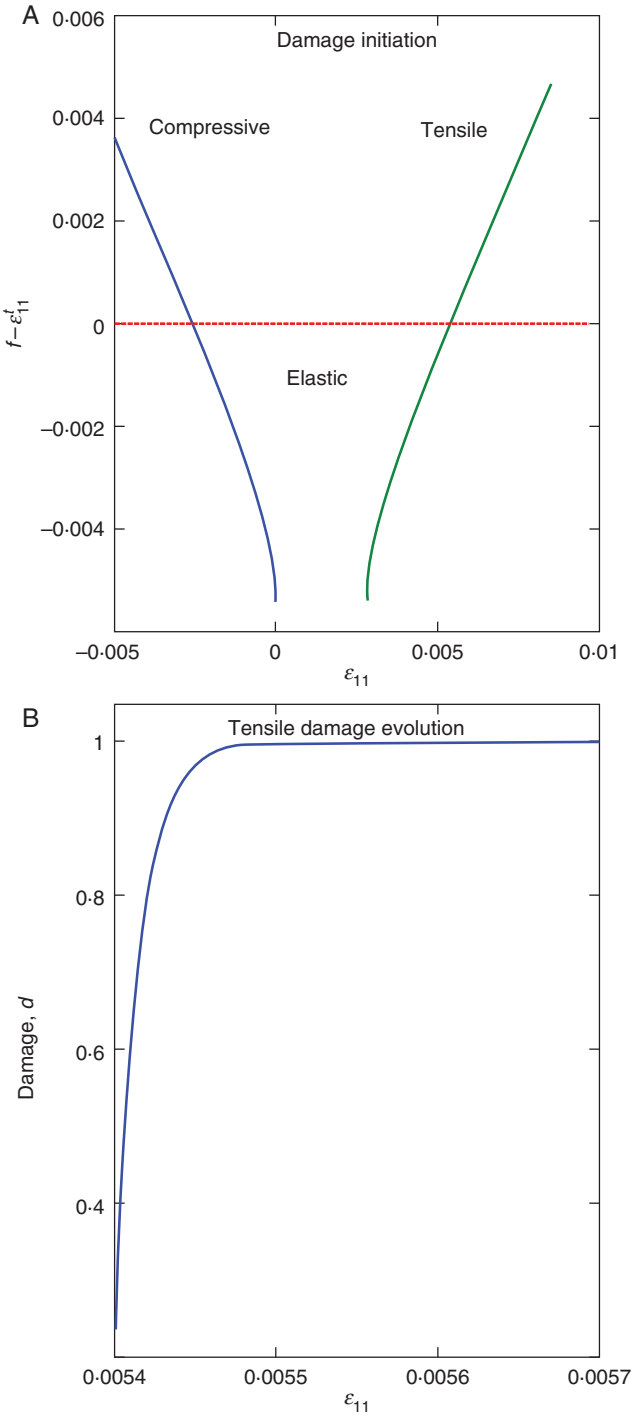

FIG. 2. Root failure behaviour described by the constitutive law. (A) Damage initiation criterion $f - \varepsilon_{11}^{t}$ compared with 0; green curve above 0 (red horizontal line) means damage initiation in the tensile direction, blue curve above 0 means damage initiation in the compressive direction and both below 0 means an elastic state. (B) Damage (d) developed in the tensile axial direction.

defined as the damage evolution law:

$$d = 1 - \frac{\varepsilon_{11}^{t}}{f} e^{-\left(\frac{E_r \varepsilon_{11}^{t}(f-\varepsilon_{11}^{t})L^c}{G_f}\right)} \quad (6)$$

where L^c in our case is the characteristic length of the beam element and G_f is the fracture energy of the root material. The damage variable d is valid and takes continuous values from 0 to 1 from the axial failure strains defined by f in the compressive and tensile directions. Figure 2B gives an example of the behaviour of d in the tensile direction (data set SA5 of Table 3). The damage variable d increases abruptly, which means our constitutive law models root brittleness correctly. Finally, stiffness degradation in the root material is modelled by including the damage variable in the stiffness matrix as follows:

$$[\boldsymbol{C}_{\mathbf{d}}] = \begin{bmatrix} (1-d)E_r & 0 & 0 \\ 0 & (1-d)G_r & 0 \\ 0 & 0 & (1-d)G_r \end{bmatrix}. \quad (7)$$

This shows that, after reaching the damage initiation criterion, the evolution of d causes the stiffness in the root material to decrease progressively. In our case, convergence difficulties occurred during calculations due to the complex geometry (the multi-branched root system) and large deformations. Thus, viscous regularization is applied to the damage variable d to improve convergence, and the regularized damage variable d^v is used in the program instead of d:

$$\dot{d}^v = \frac{1}{\eta}(d - d^v) \quad (8)$$

where η is the viscosity parameter controlling the rate at which d^v approaches the true damage variable d. The value of η is assumed to be small compared with the size of the increment to satisfy the assumption of quasi-brittle material.

Verification of the model for individual root failure. Before applying the constitutive law to the whole root system, it is necessary to test whether it reproduces the brittle rupture of the root material; rupture is expected to occur at the strength limits (σ_{11}^t or σ_{11}^c) with a sharp decrease in stress after failure. Tensile, compressive and bending tests were performed numerically in ABAQUS on a cantilever beam 1 m in length and 0·04 m in diameter, with a characteristic length ($L^c = 0{\cdot}1$ m) and the root material properties for SA5 given in Table 3. Displacement was separately imposed at the free end of the beam in the tensile direction, the compressive direction and perpendicular to the axial direction (Fig. 3A). Panels 1, 2 and 3 in Fig. 3 show the force-displacement curves obtained at the free tip of the beam during calculations for tensile, compressive and bending simulation tests, respectively. Figure 3B4 illustrates the numerical effect due to the viscous regularization parameter η. Panels 1 and 2 in Fig. 3B show that the root tensile and compressive strength predicted by tests agree well with the input (σ_{11}^t and σ_{11}^c). Root compressive behaviour is as brittle as that in tension and the root fails in compression at a lower axial strain, while the degradation of bending strength and stiffness is more gradual (Fig. 3B3). Parameter η for viscous regularization was calibrated by beam tensile tests with five different η values ranging from 0·00001 to 0·1, compared with the

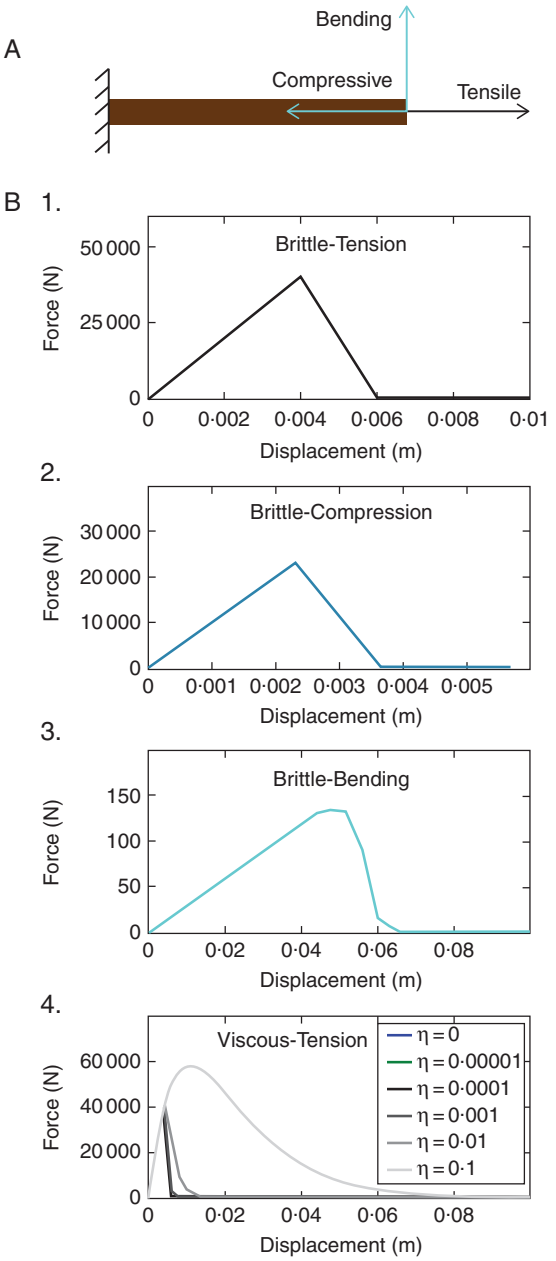

FIG. 3. Numerical root failure behaviour tests and results. (A) A cantilever beam of wood material subjected to different displacements at the free end: tensile, compressive and bending tests. (B) Force–displacement curves predicted by simulations at the free end: 1, tensile test; 2, compressive test; 3, bending test; 4, tensile tests including viscous effect (η values are 0·0, 1·0e−5, 1·0e−4, 1·0e−3, 1·0e−2 and 1·0e−1).

increment of 0·02 (Fig. 3B4). The three smaller η values (0·00001, 0·0001 and 0·001) predict curve behaviour similar to that without viscous regularization. However, the results from larger η values (0·01 and 0·1) predict less brittle tensile behaviour and overestimate the tensile strength of the root specimen. Thus, small η values compared with the characteristic size of increments should be used to avoid numerical discrepancies when modelling root mechanical behaviour. In the following, simulations hold for $\eta = 0{\cdot}000075$.

Field experiment and parameter measurements

Site and tree-pulling experiment. A tree-pulling experiment was carried out on 24 April 2012 on a selected 13-year-old *P. pinaster* tree 0·18 m in diameter at breast height (Nézer forest in the southwest of France, altitude 15 m, latitude 44·6/44° 36′0″ N, longitude −1·03333/1° 1′60″ W; la Mairie du Teich). In 2012 the site had a total yearly rainfall of 846·7 mm and a mean temperature of 9·2 °C (Météo France). The pulling direction was perpendicular to the prevailing wind direction (northwest). The experimental protocol was similar to that used by Nicoll *et al*. (2006) and many others (Coutts, 1986; Moore, 2000; Cucchi *et al*., 2004; Kamimura *et al*., 2012). The selected tree was overturned with a motorized winch (WinchMax 7550, 5681 kg; Winchmax, UK; http://www.winchmax.co.uk/). The cable was attached to the stem of the pulled tree at the height of 1·68 m. The winch was attached to the stem base of an anchor tree at a distance of ≃12 m from the pulled tree so that the pulling force can be considered horizontal with an error of 1 %. The part of the tree above this height was cut off. The pulling force was measured by a load cell (SM 5420, 50 kN; Sensel, France) and the stem deflection angles on the top and at the base of the stem were measured by two inclinometers (SN: 25276; Sensel, France). The turning moment was calculated using the horizontal component of the pulling force.

Root architecture. Root system excavation, measurements and modelling were performed according to Danjon *et al*. (1999, 2005). On 15 May 2012 the soil surrounding the damaged root system was removed with a high-pressure soil pick (Soil Pick; MBW Inc., USA; http://www.mbw.com/products/Pick.aspx) and the root system was excavated with a large mechanical shovel. Roots thinner than 1 cm in basal diameter were removed before the measurements. Root breakages were marked and large root deformations corrected manually, in order to return as close as possible to the undamaged state of the root system. In the meantime, the root system was discretized by a Polhemus Fastrak low magnetic field digitizer (Polhemus, Colchester, VT, USA; http://www.polhemus.com) and encoded in a standard format (MTG) commonly used for representing branching topological relationships at different observation scales (Godin and Caraglio, 1998). The MTG file was then read by Xplo software and exported to the root anchorage model in a format readable by ABAQUS.

Soil mechanical parameters. Around the pulled tree, soil was sampled at four locations in the main cardinal directions at depths of 0–10, 10–30 and 30–60 cm, just above water table level (≃60 cm depth) to measure soil bulk density and water content and to collect material for the mechanical tests. Then, 12 sandy soil samples were reconstituted with an initial dry bulk density of 1410 kg m^{-3} and an initial gravimetric water content of 0·11 g g^{-1}, both corresponding to the mean values measured in the field. Direct shear tests were conducted using a Wykeham Farrance shear testing machine to characterize soil mechanical properties. The soil material was assumed to be initially linear elastic (defined by modulus of elasticity E_s), combined with plastic behaviour modelled using the Mohr–Coulomb failure criterion available in the ABAQUS materials library (Table 1):

TABLE 1. *Measurements of mechanical properties of soil material: elastic–plastic with the Mohr–Coulomb criterion*

	Symbol	Value	Unit
Density	ρ_s	1410	kg m^{-3}
Modulus of elasticity	E_s	19·86	MPa
Poisson's ratio	ν	0·33	–
Cohesion	c	21·402	kPa
Friction angle	ν	14·62	°
Dilation angle	ψ	0	°

$$\tau_{max} = \sigma_n \tan \phi + c \quad (9)$$

where τ_{max} is soil shear strength, σ_n the normal pressure in the soil failure plane, ϕ the soil internal friction angle and c the soil cohesion (Bardet, 1997).

Simulation set-up

Simulations were performed to mimic the field experiment. The stem height at which the pulling force was applied was 1·68 m. The soil domain (dimensions 8 m × 8 m × 4 m) was meshed with eight-node linear brick elements with reduced integration (C3D8R in the ABAQUS element library), with the region containing the roots meshed into finer elements with an approximate edge size of 0·25 m. Symmetrical boundary conditions (XSYMM and YSYMM in the ABAQUS Analysis User's Guide) were imposed on the four laterals of the soil domain so that these faces were blocked to constrain soil motions with respect to the planes considered (x, z and y, z). The boundary condition of fully built-in (ENCASTRE in the ABAQUS Analysis User's Guide) was defined for the bottom of the soil to block all six degrees of freedom in the x, y plane. The root architecture measured was imported into ABAQUS as already explained. Loading was applied on the root–soil system in two steps: the gravity body force was applied first with gravity constant $\mathbf{g} = 9{\cdot}81$ m s^{-2}, then a horizontal displacement of 1·2 m was imposed in the direction of the x axis at the top of the stem to ensure a maximum deflection angle of 45°. This displacement implies large deformations in the root–soil system, which makes sure that maximum turning moment occurs largely before the end of the simulation. The reaction force and corresponding displacement at the top of the stem were recorded during the simulation. The force–displacement response curves were analysed by calculating the work done by the pulling force as the integral of pulling force F as a function of the maximum horizontal displacement, d_0, imposed on the top of the stem:

$$W(F, d_0) = \int_0^{d_0} F(x)\mathrm{d}x \quad (10)$$

with x the horizontal displacement. The 3-D anchorage model requires a set of root parameters, namely ρ_r (root density), E_r, σ_{11}^t, σ_{11}^c and G_f, to characterize root mechanical behaviour. The relationships among these parameters were developed using recent evidence for stem wood of pine species and roots of *P. pinaster* reported in the literature (Stokes and Mattheck,

1996; Stokes *et al.*, 1997; Khuder *et al.*, 2007; Niklas and Spatz, 2010; Kretschmann, 2010). Niklas and Spatz (2010) showed that the modulus of elasticity E_r was linearly correlated to root density ρ_r, tensile strength σ^t_{11} and compressive strength σ^c_{11} for the stem wood of more than 100 worldwide species. Here data for green wood samples of 16 pine species (Kretschmann, 2010) were used to obtain these relationships (Table 2). Values of ρ_r and E_r were found to decrease with increasing distance from the tree stem in the lateral roots of *P. pinaster* (Khuder *et al.*, 2007). Thus, considering that the diameter decreases with increasing distance, ρ_r and E_r were assumed to be positively linearly correlated to root diameter. E_r was fixed at 8 GPa for a root diameter of 3·5 cm in the first simulation, SA1 (range taken from data source: Stokes *et al.*, 1997; Khuder *et al.*, 2007). A linear variation in E_r from 7·2 to 8·8 GPa was defined for SA1 for root diameters ranging from 1 to 6 cm (Fig. 4). The value of E_r for roots of diameter <1 and >6 cm was fixed at constant values equal to 7·2 and 8·8 GPa, respectively (Fig. 4). Then all the other mechanical parameters related to E_r were determined using relationships in Table 2. The fracture energy G_f was fixed at a value found in the literature (Dourado *et al.*, 2008), i.e. 209·4 J m^{-2} for the stem wood of *P. pinaster* for all the simulation cases. To take into account variety in mechanical properties and variety in relationships between mechanical and geometric properties (i.e. root diameter in our study), four other simulation cases were defined in the same way with (1) different E_r central values for roots of diameter 3·5 cm (9·2 and 6·8 GPa in SA2 and SA3, respectively; Fig. 4); and (2) different variations in E_r for the range of root diameters (1 and 6 cm) ($\pm$ 20 % and $\pm$ 0 % with respect to the central value in SA4 and SA5, respectively; Fig. 4).

Two other simulations, SA6 and SA7, without root failure behaviour were also performed in comparison with the previous five simulations and the experiment. Simulation SA6 defines elastic behaviour for all roots with E_r of 8 GPa and a Poisson ratio of 0·3 for all roots, and SA7 defines elastoplastic behaviour, with the elastic behaviour again $E_r = 8$ GPa and plastic threshold the same value of σ^t_{11} as that defined for SA5. All root mechanical parameters used in these simulations are summarized in Table 3.

TABLE 2. *Linear correlations between* E_r *(in GPa) and* $\{\rho_r, \sigma^t_{11}, \rho_r\}$ *for green wood of 16 pine species*

	Correlation	Unit	R^2
ρ_r	38·94 E_r + 109·91	kg m^{-3}	0·641
σ^t_{11}	5·07 E_r + 2·61	MPa	0·577
σ^c_{11}	2·37 E_r + 1·69	MPa	0·633

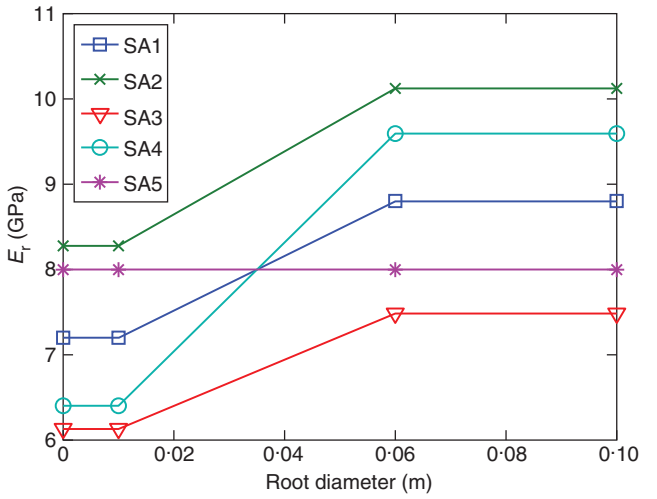

FIG. 4. Linear relationships of modulus of elasticity of root material (E_r) versus root diameter applied to the entire root system for five simulation cases (SA1–SA5). More detailed information about parameter values in each case is presented in Table 3.

RESULTS

Moment–rotation response curves

Simulations in comparison with the experiment. The response curves provided by the simulations with root breakage and the *in situ* tree-pulling test were compared, taking the deflection angle at the stem base. The simulated response curves exhibited typical behaviour for brittle material with successive root breakages (Fig. 5). Large decreases in turning moment are due to root breakages whereas very small decreases are mainly due to numerical errors related to local algorithmic convergence difficulties. The simulations suggest that the contribution of roots to anchorage strength is strongly influenced by their mechanical properties. For example, the abrupt decrease in turning moment by 2130 N m at 7·3° for simulation SA3, caused by the breakage of a thick counter-winchward lateral root, was delayed in cases SA1 and SA2 which had globally higher E_r, σ^t_{11} and σ^c_{11}. The cases with higher E_r, σ^t_{11} and σ^c_{11} in all roots (SA1 and SA2) and the case with higher E_r, σ^t_{11} and σ^c_{11} only in thicker roots (SA4) predicted greater anchorage strength (i.e. critical turning moment).

Root breakage in comparison with no root breakage. The response curves, i.e. the turning moment of the pulling force against the deflection angle at the stem base, obtained from two simulations (SA6 and SA7) without root breakage were compared with a representative simulation, SA1, defining root breakage and the experiment (Fig. 6). SA6 predicted a continuously increasing turning moment within the considered interval of deflection angle. Therefore, defining the critical turning moment for root anchorage strength would be inappropriate. The turning moment predicted by SA7 reached the global maximum deflection angle at 27·5°, after which it decreased slightly and gradually. The slight decrease in turning moment is probably due to both the negative contribution of soil softening behaviour after plastic yielding and the zero contribution of the root after plastic yielding. Within the considered interval, SA1 predicted a response curve similar to that of the experiment in terms of magnitude of turning moment. SA6 and SA7 predicted clearly much higher values in turning moment with respect to SA1 and the experiment.

Evolution of apparent stiffness of the root–soil system during the tree-pulling process. Simulations including root breakages exhibited abrupt decreases in the moment–rotation response curves, followed by increases. These local increases characterize the root–soil system strength, which changes during the uprooting process. It can be quantified in terms of apparent stiffness of

TABLE 3. *Root data sets for five simulations (SA1–SA5) using the 3-D anchorage model*

	Unit	Root diameter interval	SA1	SA2	SA3	SA4	SA5	SA6	SA7
E_r	GPa	<1 cm	7·2	8·3	6·1	6·4	8	8	8
		1–6 cm	7·2–8·8	8·3–10·1	6·1–7·5	6·4–9·6	8	8	8
		>6 cm	8·8	10·1	7·5	9·6	8	8	8
ρ_r	kg m^{-3}	<1 cm	379·3	421·4	337·2	337·2	421·4	421·4	421·4
		1–6 cm	379·3–463·6	421·4–515·0	337·2–412·2	337·2–505·7	421·4	421·4	421·4
		>6 cm	463·6	515·0	412·2	505·7	421·4	421·4	421·4
σ^t_{11}	MPa	<1cm	38·8	44·3	33·4	34·5	43·2		43·2
		1–6 cm	38·8–47·5	44·3–54·1	33·4–40·8	34·5–51·8	43·2		43·2
		>6 cm	47·5	21·1	40·8	51·8	43·2		43·2
σ^c_{11}	MPa	<1 cm	18·6	21·1	16·0	16·5	20·6		
		1–6 cm	18·6–22·7	21·1–25·8	16·0–19·6	16·5–24·8	20·6		
		>6 cm	22·7	25·8	19·6	24·8	20·6		

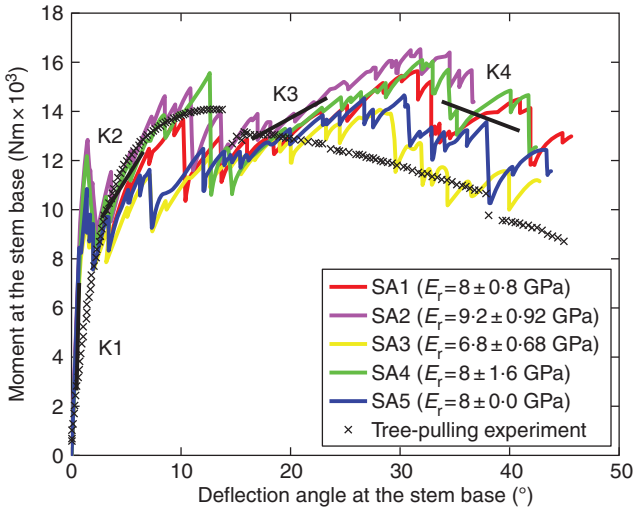

FIG. 5. Comparison among five simulations (SA1–SA5) with different data sets of root mechanical parameters and the curve measured from the tree-pulling experiment: turning moment of pulling force against deflection angle at the stem base. K1, K2, K3 and K4 are averaged system stiffnesses (slopes) at four intervals of deflection angle.

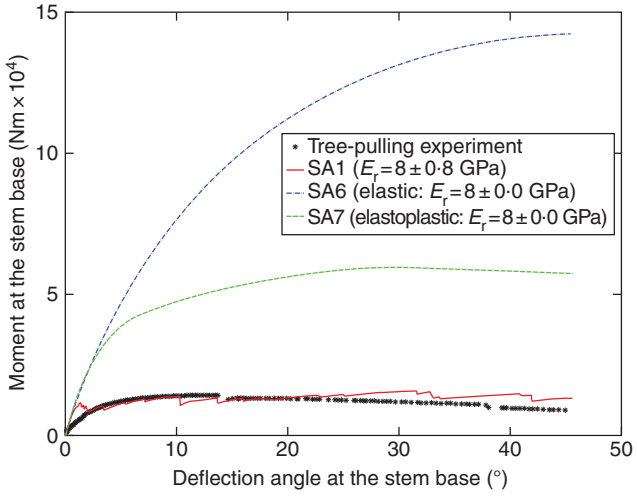

FIG. 6. Comparison among the two simulations without root breakage (SA6 and SA7), simulation SA1, including root breakage, and the experiment: turning moment of pulling force against deflection angle at the stem base.

the root–soil system due to successive breakages and successive activation of new roots to sustain the loading. The trend of system stiffness degradation as a function of deflection angle is thus represented by progressively decreased apparent slopes (i.e. K1, K2, K3 and K4) within four intervals of deflection angle. To determine K1, K2, K3 and K4, we proceeded as follows: (1) for each of the five simulation curves, we first identified four successive intervals with an apparent slope to be determined for each of them; (2) the apparent slope within each interval of the simulation was determined by linear regression; (3) then, each Ki was calculated for interval i as the mean value of apparent slopes from five simulation cases. For all simulations, the first recovery of the turning moment characterized by K2 gave rise to a local maximum turning moment at $\simeq$10°. This interval matched the deflection angle at which the critical turning moment occurred in the experiment (14°). However, the second recovery of turning moment characterized by K3 gave rise to the global maximum at $\simeq$30°, slightly higher than the previous one. Compared with the simulation curves, the curve from the experiment was much smoother, being divisible into three parts marked by two abrupt decreases in turning moment, at 14° and 38° respectively. Recovery after the peak value was small enough to be neglected. Taking the global peak as the critical turning moment, simulations SA1–SA5 overestimated anchorage strength by up to 17·8 %. Another main difference between the measured and simulated response curves was the initial stiffness behaviour. Firstly, the initial stiffness estimated by all simulations was higher than the measured value. Secondly, the measured stiffness gradually decreased, as characterized by the smoothness of the curve, whereas in the simulations the decreases in initial stiffness due to root breakages were abrupt and without transition.

Energy induced by the pulling force: simulations in comparison with the experiment

The fundamentals of continuum damage mechanics have related numerous energy-based concepts and approaches to the damage behaviour of materials (Krajcinovic, 1996; Murakami, 2012). Simulations were analysed using the stored energy of the root–soil system induced by the pulling force. Figure 7

shows the evolution of energy induced by the pulling force as a function of the horizontal displacement at the pulling point during the tree-pulling process, for simulations SA1–SA5 and the experiment. For all the simulations, the energy was in good agreement with that of the experiment. At the initial loading stage (horizontal displacement of pulling point ranging from 0 to 0·2 m) the root–soil system in all the simulations was stiffer than that in the experiment. Therefore, the predicted energy was initially higher in all the simulations.

Linking successive root breakage to tree mechanical response to overturning

Our model can now be used to examine successive root breakage during the uprooting process. Figure 8 illustrates how broken roots can be detected and the connection between successive root breakage and the mechanical effect on root anchorage strength. The response curve shows the turning moment calculated at the stem base versus the deflection angle at the stem base (Fig. 8A). The first square mark on the curve is linked to Fig. 8B1, which shows the state of the intact root system just before the first root breakage. The uniform greenish blue colour in the root system indicates the zero value of the damage variable *d* (SDV1 in the legend), meaning no damage has occurred. The second square mark on the curve is linked to the state of the root system shown in Fig. 8B2. Figure 8B2 shows the moment after the successive breakage of three finer intermediate roots <2·5 cm in basal diameter, a lateral root 5·5 cm in basal diameter and a thick chuck-like oblique root 8·7 cm in basal diameter. Broken root segments are represented in red in Fig. 8B2. These broken roots reduce the turning moment by 1905 N m. The third square mark corresponds to the moment just before the breakage of a thick lateral root in the counter-winchward direction (the root marked by a circle in Fig. 8B3), and the fourth square mark to the moment immediately after root breakage (the damaged root zone circled in Fig. 8B4).

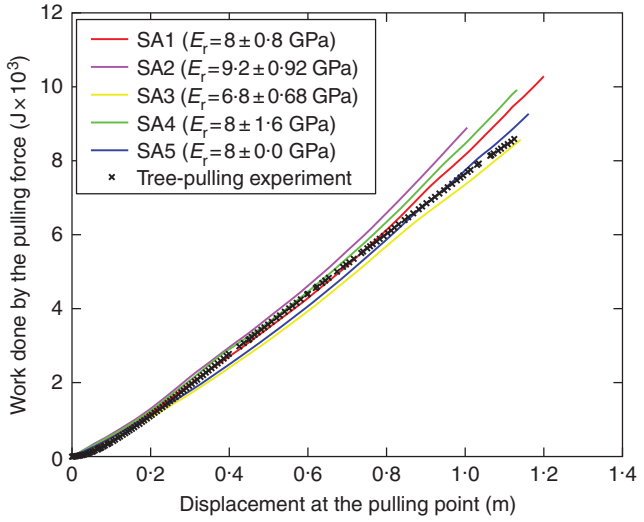

FIG. 7. Evolution of the work done by the pulling force during the tree-pulling process predicted by simulations (SA1–SA5) compared with that measured in the tree-pulling experiment.

Breakage of this thick lateral root alone leads to a sudden drop of 2130 N m in turning moment. After each drop in turning moment caused by root breakage, the redistribution of stresses released by the broken root(s) to the other roots leads to another recovery of the turning moment. The root breakage tendency (i.e. root types and locations) predicted by our model was compared with field observations during root system excavation. Field observations showed breakage of a large number of relatively finer roots, a large shallow root in the counter-winchward direction and a shallow root in the sector perpendicular to the winchward direction. In particular, the damage in the thick shallow root in the counter-winchward direction was initiated very close to the stump, cracking along a large segment. The detailed root damage state in Figure 8B4 shows that our model predicts qualitatively fairly well the observed root breakage tendency; the same shallow root in the counter-winchward direction was also broken close to the stump, and many small roots were broken.

DISCUSSION

Our strategy for developing the model was to provide a model with the same degree of physical realism for the three main components: (1) root architecture; (2) root mechanical strength; and (3) soil strength. As previous numerical work has focused on root architecture (Dupuy *et al.*, 2005*b*; Fourcaud *et al.*, 2008), this new model was developed to integrate a more realistic description of individual root behaviour and soil. A constitutive law for root mechanical rupture was developed to describe root failure under tension, bending and compression. Using data from the literature, we established a specific parameterization for root mechanical properties and their variation as a function of root dimensions. This method led to simulation of the successive breakage of roots during uprooting, something that had not been done before. Also, the simulated tree response curve obtained without any calibration was in good agreement with our observations. The following section is devoted to an examination of these results and an assessment of the potential of this new model and its limitations.

Initial root–soil stiffness

The initial stiffness of the root–soil system was not properly estimated by the model. However, it is important to accurately estimate tree inclination in addition to trunk bending under the effect of wind. In particular, to assess the risk of uprooting the initial stiffness is required in order to estimate the moment applied to the crown due to wind and gravity and compare it with the critical turning moment. Moreover, it could be valuable when considering damage resulting from tree inclination after a windstorm without uprooting or breakage, i.e. toppling, usually reported for young trees (Moore *et al.*, 2008), or when considering the wind's interaction with trees for landscape-scale problems (Gardiner *et al.*, 2000). In the latter case, it is common to model the root–soil system without flexibility due to a lack of quantitative information, despite the fact that including flexibility improves prediction (Neild and Wood, 1999; Jonsson *et al.*, 2006). The present model overestimates the initial stiffness of the root–soil system. We performed a sensitivity analysis in order to identify the model parameters responsible for this discrepancy

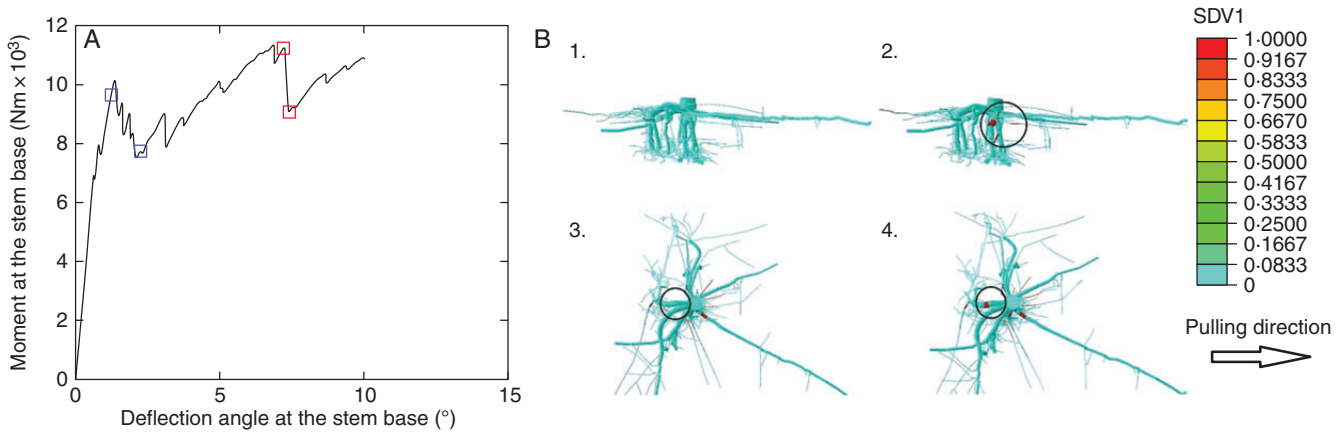

FIG. 8. Linking successive root breakage effects to tree overturn response. (A) Turning moment of pulling force against deflection angle at the stem base (SA3) with four squares marking breakage points. (B) Root damage state (SDV1) in the root system at four moments corresponding to square marks on the curve in (A): (1) intact state of the root system related to the first blue square; (2) after several root breakages, marked by a black circle related to the second blue square; (3) state of root damage before breakage of a thick counter-winchward root occurs, marked by a black circle, related to the first red square; (4) state of root after breakage of a thick counter-winchward root occurs, marked by a black circle, related to the second red square.

between the simulations and the observations. Four mechanical parameters of roots and soil were selected for this sensitivity analysis. The purpose was to quantify their separate influences on the initial behaviour of the root–soil system characterized by the initial slope of the force–angle response curve. Root tensile strength σ^{t}_{11}, compressive strength σ^{c}_{11} and fracture energy G_f were not selected in this analysis, because these parameters are involved in calculations only if root breakage occurs. However, according to the simulation results no root breakage was detected during the early loading stage considered. For all cases the initial stiffness of the root–soil system was calculated as the slope of the response curve for reaction forces ranging from 0 N to 4 kN (Fig. 9). The initial stiffness is supposed to be calculated within the material elastic state of the system. However, in the case of soil cohesion variation of −50 %, the soil zone surrounding the root system was yielding when the reaction force reached 4 kN (blue curve in Fig. 9). The initial stiffness was revaluated just before the first yielding zone appeared in the soil in this case (green curve in Fig. 9). The initial slope of the force–angle response curve is mainly influenced by the modulus of elasticity of the root and soil materials. A variation of ± 50 % in the modulus of elasticity of the roots leads to a variation in the initial slope of −37·5 and +32·1 %, positively related to the input variation. The same variation in the modulus of elasticity of the soil leads to a variation in the initial slope from −19·0 to +8·3 %. Soil cohesion and friction angle are not influential factors as long as the overall soil state remains elastic at the early loading stage considered. For the case of a 50 % decrease in soil cohesion, when the pulling force reached ∼4 kN, the plastic yielding occurred in a zone ∼60 cm in size (including the stump) in the soil domain. The first evaluation of initial stiffness in the force interval [0, 4 kN] gives a decrease of 19·2 % in initial stiffness (blue circles in the third column of Fig. 9). The fact that the yielding area appears on the soil surface at a very early loading stage in this case can be explained by the lower soil shear strength resulting from the reduced soil cohesion, according to the Mohr–Coulomb equation $\tau_{max} = \sigma_n \tan\phi + c$. Revaluation of initial stiffness was then computed in the interval ranging from the soil initial state to the soil elastic state just before yielding. The result shows that the slight variation of 1·3 % is due to a decrease of 50 % in soil cohesion (green circles in the third column of Fig. 9). Finally, the sensitivity analysis indicates that the overestimate of initial root–soil stiffness is due to the overestimation of input elastic data, namely E_r and E_s. Thus, the accurate estimation of root–soil stiffness probably requires a good estimate of the elastic modulus for both soil and root. The overestimation is probably due to the lack of data on root mechanical properties. Furthermore, Young's modulus of roots at the early loading stage was found to be lower than average values due to their initial tortuosity, and after stretching roots become stiffer, exhibiting average root material stiffness (Commandeur and Pyles, 1991). In the model, Young's modulus was defined to be constant with respect to root geometry change during the course of tree-pulling, which may potentially lead to overestimation of initial stiffness. This new insight into root–soil stiffness illustrates the potential of the present mechanistic model for further application, such as tree–wind interaction for landscape-scale problems for which root–soil flexibility remains poorly described (Jonsson *et al.*, 2006; Szoradova *et al.*, 2013).

Modelling root failure

The relevance of this new model lies essentially in the improvement obtained in modelling root–soil failure. This gives a more realistic description of every important aspect of the first mechanistic model of root anchorage (Blackwell *et al.*, 1990). For the first time, we have produced a model that simulates root ruptures realistically, by combining a constitutive law for rupture in composite materials and mechanical parameters for wood available in the literature. Our constitutive law accounted for root brittle failure behaviour under tension, compression and bending. We demonstrated through a simulation case that the numerous drops in turning moment were directly linked to successive root breakages. This type of behaviour with successive drops has been reported in previous field investigations on tree-pulling tests (Cucchi, 2004). In addition, the signature of

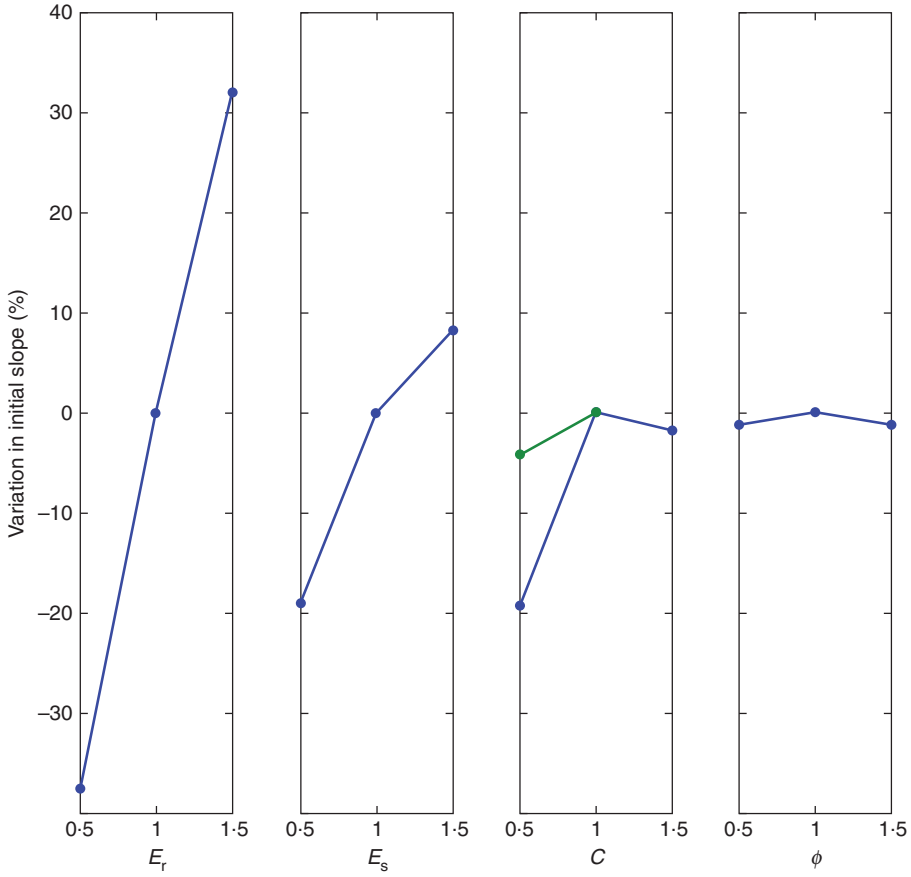

FIG. 9. Sensitivity analysis of the initial slope of the response curves: initial slope variation versus ±50 % variation in modulus of elasticity of roots (E_r), modulus of elasticity of soil (E_s), soil cohesion (c) and soil friction angle (ϕ). The initial stiffness of the root–soil system was evaluated twice for the case of a −50 % decrease in soil cohesion (c), with the second evaluation marked by a green circle.

root breakages during uprooting was also reported by Coutts (1983), who measured the sound made by successive root breakages using microphones. This behaviour with successive ruptures was also observed in studies performed to prevent soil erosion by using roots to increase slope stability. This cumulative rupture was reported for numerous field pull-out tests using fine root bundles and this trend could be reproduced in several models adapted from the fibre bundle model (Riestenberg, 1994; Pollen *et al.*, 2004; Schwarz *et al.*, 2012, 2013). In these cases, the problem was to evaluate the contribution of fine roots to soil reinforcement, so only the tensile failure of roots was accounted for, and root diameter was generally <1 cm. In our case, the tree uprooting process involves coarse roots under tension, compression and bending failing progressively, which requires a model dedicated to uprooting.

Compared with previous tree anchorage models, our model is able to provide more realistic response curves with respect to the experiment and predicted a peak value of turning moment that defined properly the critical turning moment (Dupuy *et al.*, 2005*b*, 2007; Rahardjo *et al.*, 2009). Our results gave fairly accurate descriptions of the behaviour of the root–soil system during tree overturning. Despite the simplifications introduced for root–soil interaction and root material, the estimated critical turning moment was reasonably correct and close to that measured in the experiment. In addition to this first quantitative validation, this new model seems robust in terms of the physics simulated. Our damage model is derived from continuum damage mechanics, for which energy estimation is essential (Murakami, 2012). All the simulations were in good agreement with the experiment in terms of energy induced by the pulling force. A more in-depth analysis of this aspect of the model would require better simulation of the rupture behaviour of individual roots. At this stage, the constitutive law for root rupture is based on the literature and has not been validated by comparison with mechanical tests on individual roots.

Whereas the model appears to estimate the critical turning moment well, it differs from the observations when considering post-rupture behaviour. The simulations exhibited moment–rotation curves that increased after the first stage of the ruptures, contrary to the experimental curve. First from a physics point of view, if larger and stiffer roots take the role of other roots which carried the loads before their breakage, the recovery contributed by these roots may be much more significant than that contributed by roots with lower stiffness (i.e. lower E_r or smaller diameter). Our simulations defined higher E_r values from the wide range for coarse roots, which could potentially lead to a more significant recovery in turning moment. In addition, this discrepancy could also be partially explained by

certain numerical prerequisites. Indeed, the root slippage caused by large deformations of the root–soil system was constrained by the root–soil interaction method used, namely the embedded element method. Thus, potential errors could arise due to the fact that no possible failure occurs at the root–soil interface. Recent developments in understanding soil reinforcement by fine roots permits root–soil interactions to be modelled more accurately by incorporating friction laws for root–soil interaction (Pollen, 2007; Schwarz *et al.*, 2012, 2013). However, friction laws prove to be expensive in terms of computational cost due to complex geometries and interactions in our model. Such a high level of complexity will probably not be required in the near future because the embedded element method turned out to be a good compromise between accuracy and computational cost (see results in Appendix).

Root mechanical properties

One significant result of this study concerns the role of the mechanical strength of roots. By linking the global root–soil system response characterized by the response curve to local root breakages detected by visualization, we are able to detect broken roots at a given moment. The root breakage pattern due to tree-pulling was fairly well imitated, which allowed us to use the model as a diagnostic tool to explain the mechanical role played by the main root components. The results show that root thickness and root location may strongly influence the contribution of the tree response to overturning. Thick counter-winchward lateral roots contribute more significantly to anchorage strength in comparison with relatively fine lateral and intermediate roots. Furthermore, thick counter-winchward lateral roots contribute more than thick oblique roots. For the first time, we highlight the role played by mechanical properties of roots in the tree's response to overturning, as previously suggested by Coutts (1983). In our study, we found that both higher root mechanical strength with higher E_r in all roots and higher strength with higher E_r only in thicker roots provided better root anchorage, which is reasonably correct. But we had to simplify certain root mechanical properties due to the lack of data on root material. Firstly, relationships among the material properties of coarse roots were assumed to be similar to those in stem wood. Thus, the correlations established between E_r and the other three parameters, ρ_r, σ^t_{11} and σ^c_{11}, for stem wood also applied to roots. However, it is generally believed that the mechanical properties of roots differ from those of stem wood and vary enormously depending on root age, tree species and root physical properties such as cellulose and water contents (Genet *et al.*, 2005). For example, the tensile strength measured for coarse roots may range from 9 to 63 MPa (Coutts, 1983). For the same species (*P. pinaster*), the longitudinal modulus of elasticity measured may vary from 0·8 to 11 GPa (Stokes *et al.*, 1997; Khuder *et al.*, 2007). The data sets built into all our simulations always took higher values of E_r in the range of 0·8–11 GPa, which may lead to estimation errors for all the other parameters related to E_r. Furthermore, our sensitivity analysis showed that overestimation of E_r potentially led to overestimation of the initial stiffness of the root–soil system. Secondly, relationships between root mechanical properties and root diameter were assumed to be positive linear, based on similar descriptive findings for coarse roots (Stokes and Mattheck, 1996; Khuder *et al.*, 2007). This may have caused estimation errors for root anchorage strength. Moreover, another mechanical parameter, G_f, remained constant for all the simulation cases. This may have led to errors in characterizing root failure behaviour. Finally, we formulated a damage model with an assumption of brittle material for roots. However, load displacement curves from fracture tests on single-edge-notched beams showed that wood in bending exhibited less abrupt post-rupture behaviour than that predicted by our model (Dourado *et al.*, 2008). In conclusion, more experiment results will be needed to improve and validate the damage model for roots.

Soil mechanical properties

This new model was tested using a set of measured soil properties corresponding to the soil conditions of the tree-pulling tests. This represents a significant improvement because previous modelling approaches either did not consider soil material properties or used only literature findings to model general soil mechanical behaviour (Blackwell *et al.*, 1990; Dupuy *et al.*, 2005*b*; Rahardjo *et al.*, 2009). However, the role of the soil compartment remains poorly described and is treated as a homogeneous medium, so that improvements are required in the future to evaluate its impact on tree anchorage. The presence of a water table, rocks, hardpan and organic matter (dead leaves and stumps, roots, soil surface vegetation etc.) modifies the soil, making it much more porous and far from a homogeneous material, as considered here. In particular, numerous studies confirmed that the local presence of fine roots can improve local soil shear strength by providing additional cohesion to the soil (Waldron, 1977; Wu *et al.*, 1979; Waldron and Dakessian, 1981; Pollen and Simon, 2005; Schwarz *et al.*, 2010; Mao *et al.*, 2012). The present model could be used to investigate the influence of forest soil properties and its spatial variation on tree stability.

Conclusions

This paper presents a new model of tree anchorage capable of simulating root breakages for the first time. It also permits the localization of damage within the root system and includes specific parameterization for root and soil properties based on measurements and experimental evidence reported in the literature. These simulations were performed without any calibration and were found to be in good agreement with the observations. The results are promising enough to allow consideration of further applications to adult trees, which are more vulnerable to uprooting than young specimens. However, the architecture of the root system of adult trees is different from that of young trees for *P. pinaster*. This could increase the degree of complexity of the model. For example, the formation of a rigid 'cage' within a root system is common for older *P. pinaster* (Danjon *et al.*, 2005). Thus, relevant adaptations for more complex root structures should be made in the model in the future. Nevertheless, our model proved useful for examining the role of root mechanical properties and thus it represents a significant step forward in our understanding of the uprooting process as a function of tree characteristics and soil mechanical properties. Mechanical consequences can also be analysed as a function of certain aspects of root system asymmetry (e.g. leeward chuck-like structure) or

other specific root features (e.g. sections of large shallow roots formed as an 'I' or oval beam type close to the stump). Therefore, the model could help us understand how trees optimize the allocation of root material. This is particularly important for our comprehension of tree anchorage. The model is also expected to provide useful information on the underground response of trees to uprooting during storms for landscape wind risk models in the future. In particular, by studying the influence of variations in soil material properties on tree overturning behaviour, the model is expected to help us understand the impact of soil management on rooting (cultivation, iron pans, high water tables, indurations and soil saturation).

ACKNOWLEDGEMENTS

This work was supported by the project FAST-A of Aquitaine Region, the project TWIST of the JCC Program of the French National Research Agency and the project ForWind (Ref. ANR-12-AGRO-0007) of the French National Research Agency.

We thank Jean-Marc Bonnefond, Didier Garrigou and Pierre Trichet for their help in the tree-pulling experiments and soil property measurements; Antoine Danquechin Dorval and Raphael Segura for the root architecture measurements; Sébastien Griffon and Hervé Rey for their help in using Xplo software; Mark Irvine for his technical support for the ABAQUS computations; and Dr Sylvain Dupont for fruitful discussions on numerical modelling and his critical reading of our manuscript. We are also deeply grateful to two reviewers for their valuable remarks and suggestions, which offered new insights in this work.

AMAP (Botany and Computational Plant Architecture; http://amap.cirad.fr/) is a joint research unit including CIRAD (UMR51), CNRS (UMR5120), INRA (UMR931), IRD (2M123) and Montpellier 2 University (UM27).

LITERATURE CITED

Abernethy B, Rutherford ID. 2001. The distribution and strength of riparian tree roots in relation to riverbank reinforcement. *Hydrological Processes* **15**: 63–79.

Ancelin P, Courbaud B, Fourcaud T. 2004. Development of an individual tree-based mechanical model to predict wind damage within forest stands. *Forest Ecology and Management* **203**: 101–121.

Bardet JP. 1997. *Experimental soil mechanics*. Upper Saddle River, NJ: Prentice-Hall.

Blackwell PG, Rennolls K, Coutts MP. 1990. A root anchorage model for shallowly rooted Sitka spruce. *Forestry* **63**: 73–91.

Commandeur PR, Pyles MR. 1991. Modulus of elasticity and tensile strength of Douglas-fir roots. *Canadian Journal of Forest Research* **21**: 48–52.

Coutts MP. 1983. Root architecture and tree stability. *Plant and Soil* **71**: 171–188.

Coutts MP. 1986. Components of tree stability in sitka spruce on peaty gley soil. *Forestry* **59**: 173–197.

Coutts MP, Nielsen CCN, Nicoll BC. 1999. The development of symmetry, rigidity and anchorage in the structural root system of conifers. *Plant and Soil* **217**: 1–15.

Cucchi V. 2004. *Sensibilité au vent des peuplements de pin maritime (Pinus pinaster Ait.). Analyse comparative de dégâts de tempête, étude expérimentale et modélisation de la résistance au déracinement*. PhD Thesis, University of Bordeaux 1, France.

Cucchi V, Meredieu C, Stokes A, *et al*. 2004. Root anchorage of inner and edge trees in stands of maritime pine (*Pinus pinaster* Ait.) growing in different podzolic soil conditions. *Trees—Structure and Function* **18**: 460–466.

Danjon F, Bert D, Godin C, Trichet P. 1999. Structural root architecture of 5-year-old *Pinus pinaster* measured by 3D digitising and analysed with AMAPmod. *Plant and Soil* **217**: 49–63.

Danjon F, Fourcaud T, Bert D. 2005. Root architecture and wind-firmness of mature *Pinus pinaster*. *New Phytologist* **168**: 387–400.

Danjon F, Khuder H, Stokes A. 2013. Deep phenotyping of coarse root architecture in *R. pseudoacacia* reveals that tree root system plasticity is confined within its architectural model. *Plos One* **8** (12) e83548. doi:10.1371/journal.pone.0083548

Della-Marta PM, Pinto JG. 2009. Statistical uncertainty of changes in winter storms over the North Atlantic and Europe in an ensemble of transient climate simulations. *Geophysical Research Letters* 36.

Dourado N, Morel S, de Moura MFSF, Valentin G, Morais J. 2008. Comparison of fracture properties of two wood species through cohesive crack simulations. *Composites Part A* **39**: 415–427.

Dupuy LX, Fourcaud T, Stokes A. 2005*a*. A numerical investigation into factors affecting the anchorage of roots in tension. *European Journal of Soil Science* **56**: 319–327.

Dupuy LX, Fourcaud T, Stokes A. 2005*b*. A numerical investigation into the influence of soil type and root architecture on tree anchorage. *Plant and Soil* **278**: 119–134.

Dupuy LX, Fourcaud T, Lac P, Stokes A. 2007. A generic 3D finite element model of tree anchorage integrating soil mechanics and real root system architecture. *American Journal of Botany* **94**: 1506–1514.

Fourcaud T, Ji J-N, Zhang Z-Q, Stokes A. 2008. Understanding the impact of root morphology on overturning mechanisms: a modelling approach. *Annals of Botany* **101**: 1267–1280.

Gardiner B, Blennow K, Carnus J-M, *et al*. 2010. *Destructive storms in european forests: past and forthcoming impacts*. Brussels: EFIAtlantic.

Gandhi K, Gilmore DW, Katovich SA, Mattson WJ, Zasada JC, Seybold SJ. 2008. Catastrophic windstorm and fuel-reduction treatments alter ground beetle (Coleoptera: Carabidae) assemblages in a North American sub-boreal forest. *Forest Ecology and Management* **256**: 1104–1123.

Gardiner B, Peltola H, Kellomaki S. 2000. Comparison of two models for predicting the critical wind speeds required to damage coniferous trees. *Ecological Modelling* **129**: 1–23.

Gardiner B, Byrne K, Hale S, *et al*. 2008. A review of mechanistic modelling of wind damage risk to forests. *Forestry* **81**: 447–463.

Genet M, Stokes A, Salin F, *et al*. 2005. The influence of cellulose content on tensile strength in tree roots. *Plant and Soil* **278**: 1–9.

Godin C, Caraglio Y. 1998. A multiscale model of plant topological structures. *Journal of Theoretical Biology* **191**: 1–46.

GPMF. 2011. *Sylviculture et stabilité. Les Cahiers de la Reconstitution, No. 1*. Cestas, France: GIS Groupe Pin Maritime du Futur.

Gray DH, Barker D. 2004. Root-soil mechanics and interactions. In: Bennett SJ, Simon A. eds. *Riparian vegetation and fluvial geomorphology*. Washington, DC: American Geophysical Union, 113–123.

Griffon S, de Coligny F. 2013. AMAPstudio: an editing and simulation software suite for plants architecture modelling. *Ecological Modelling*, in press.

Jonsson MJ, Foetzki A, Kalberer M, Lundström T, Ammann W, Stoeckli V. 2006. Root-soil rotation stiffness of Norway spruce (*Picea abies* (L.) Karst) growing on subalpine forested slopes. *Plant and Soil* **285**: 267–277.

Kamimura K, Kitagawa K, Saito S, Mizunaga H. 2012. Root anchorage of hinoki (*Chamaecyparis obtusa* (Sieb. Et Zucc.) Endl.) under the combined loading of wind and rapidly supplied water on soil: analyses based on tree-pulling experiments. *European Journal of Forest Research* **131**: 219–227.

Khuder H, Stokes A, Danjon F, Gouskou K, Lagane F. 2007. Is it possible to manipulate root anchorage in young trees? *Plant and Soil* **294**: 87–102.

Krajcinovic D. 1996. *Damage mechanics*. Amsterdam: Elsevier Science.

Kretschmann DE. 2010. Mechanical properties of wood. In: *Wood handbook: wood as an engineering material*. Madison, WI: Forest Products Laboratory, US Department of Agriculture, Chapter 5.

Linde P, Pleitner J, de Boer H, Carmone C. 2004. Modelling and simulation of fibre metal laminates. *ABAQUS Users' Conference*.

Lundström T, Jonas T, Stoeckli V, Ammann W. 2007. Anchorage of mature conifers: resistive turning moment, root–soil plate geometry and root growth orientation. *Tree Physiology* **27**: 1217–1227.

Mao Z, Saint-André L, Genet M, *et al*. 2012. Engineering ecological protection against landslides in diverse mountain forests: choosing cohesion models. *Ecological Engineering* **45**: 55–69.

McCarthy JK, Hood IA, Brockerhoff EG, *et al*. 2010. Predicting sapstain and degrade in fallen trees following storm damage in a *Pinus radiata* forest. *Forest Ecology and Management* **260**: 1456–1466.

Moore JR. 2000. Differences in maximum resistive bending moments of *Pinus radiata* trees grown on a range of soil types. *Forest Ecology and Management* **135**: 63–71.
Moore JR, Tombleson JD, Turner JA, der Colff M. 2008. Wind effects on juvenile trees: a review with special reference to toppling of radiata pine growing in New Zealand. *Forestry* **81**: 377–387.
Murakami S. 2012. *Continuum damage mechanics: a continuum mechanics approach to the analysis of damage and fracture*. Dordrecht: Springer.
Neild SA, Wood CJ. 1999. Estimating stem and root-anchorage flexibility in trees. *Tree Physiology* **19**: 141–151.
Nicoll BC, Ray D. 1996. Adaptive growth of tree root systems in response to wind action and site conditions. *Tree Physiology* **16**: 891–898.
Nicoll BC, Bardiner BA, Rayner B, Peace AJ. 2006. Anchorage of coniferous trees in relation to species, soil type, and rooting depth. *Revue Canadienne de Recherche Forestière* **36**: 1871–1883.
Nicoll BC, Gardiner BA, Peace AJ. 2008. Improvements in anchorage provided by the acclimation of forest trees to wind stress. *Forestry* **81**: 389–398.
Niklas KJ, Spatz H-C. 2010. Worldwide correlations of mechanical properties and green wood density. *American Journal of Botany* **97**: 1587–1594.
Peltola H, Kellomaki S, Vaisanen H, Ikonen V-P. 1999. A mechanistic model for assessing the risk of wind and snow damage to single trees and stands of Scots pine, Norway spruce, and birch. *Revue Canadienne de Recherche Forestière* **29**: 647–661.
Pollen N. 2007. Temporal and spatial variability in root reinforcement of streambanks: accounting for soil shear strength and moisture. *Catena* **69**: 197–205.
Pollen N, Simon A. 2005. Estimating the mechanical effects of riparian vegetation on stream bank stability using a fiber bundle model. *Water Resources Research* **41**: W07025. doi:10.1029/2004WR003801.
Pollen N, Simon A, Collison A. 2004. Advances in assessing the mechanical and hydrologic effects of riparian vegetation on streambank stability. In: Bennett SJ, Simon A. eds. *Riparian vegetation and fluvial geomorphology*. Washington, DC: American Geophysical Union, 125–139.
Rahardjo H, Harnas FR, Leong EC, Tan PY, Fong YK, Sim EK. 2009. Tree stability in an improved soil to withstand wind loading. *Urban Forestry & Urban Greening* **8**: 237–247.
Riestenberg MM. 1994. *Anchoring of thin colluvium by roots of sugar maple and white ash on hillslopes in Cincinnati. US Geological Survey Bulletin 2059-E*. Washington, DC: United States Government Printing Office.
Schwarz M, Lehmann P, Or D. 2010. Root-soil mechanical interactions during pullout and failure of root bundles. *Journal of Geophysical Research* **115**: F04035. doi:10.1029/2009JF001603.
Schwarz M, Cohen D, Or D. 2012. Spatial characterization of root reinforcement at stand scale: theory and case study. *Geomorphology* **171**: 190–200.
Schwarz M, Giadrossich F, Cohen D. 2013. Modeling root reinforcement using root-failure Weibull survival function. *Hydrology and Earth System Sciences* **10**: 3843–3868.
Stokes A, Mattheck C. 1996. Variation of wood strength in tree roots. *Journal of Experimental Botany* **47**: 693–699.
Stokes A, Fitter AH, Coutts MP. 1995. Responses of young trees to wind and shading – effects on root architecture. *Journal of Experimental Botany* **46**: 1139–1146.
Stokes A, Martin F, Sacriste S, Fourcaud T. 1997. Adaptation of tree roots to wind loading: the relationship between mechanical behaviour and wood formation. *Plant Biomechanics* 339–346.
Szoradova A, Praus L, Kolarik J. 2013. Evaluation of the root system resistance against failure of urban trees using principal component analysis. *Biosystems Engineering* **115**: 244–249.
Tamasi E, Stokes A, Lasserre B, *et al*. 2005. Influence of wind loading on root system development and architecture in oak (*Quercus robur* L.) seedlings. *Trees—Structure and Function* **19**: 374–384.
Waldron LJ. 1977. Shear resistance of root-permeated homogeneous and stratified soil. *Soil Science Society of America Journal* **41**: 843–849.
Waldron LJ, Dakessian S. 1981. Soil reinforcement by roots – calculation of increased soil shear resistance from root properties. *Soil Science* **132**: 427–435.
Wu TH, Mckinnell WP, Swanston DN. 1979. Strength of tree roots and landslides on Prince of Wales Island, Alaska. *Canadian Geotechnical Journal* **16**: 19–33.

APPENDIX

Preliminary study: comparison of two methods of root–soil interaction modelling

Materials and methods

This work was carried out in the ABAQUS environment, version 6.13 (http://www.3ds.com/products-services/simulia/portfolio/Abaqus/). The preliminary study was conducted with a 3-D model of a direct shear test on root-reinforced sandy soil. We evaluated the results given by two root–soil interaction modelling approaches, namely the embedded element approach and the frictional behaviour approach, to justify (1) the choice of beam elements to discretize the root system, and (2) the choice of the embedded element method to model root–soil interaction. The frictional behaviour method consists of applying a realistic physical law to surfaces in contact so that shear and normal stresses can be transmitted across the interface. However, this method proved unable to cope with multiple complex structures, in our case, for example, a real root system with a high branching order. The embedded element method does not take into account stress transmission across the interface and makes assumptions on translational motions of embedded root elements. Its simplified considerations make this method capable of tackling certain problems with complex geometries.

Modelling root–soil mechanical interaction. The embedded element method assumes that all the nodes of root elements are embedded in the host soil region. Each translational kinematic degree of freedom (d.o.f.) of embedded root nodes is calculated using the interpolation values of the corresponding d.o.f. of the soil nodes in the vicinity of the root node automatically searched by a specific algorithm. The region where the root system is located contains two materials, namely roots and soil. The mass and stiffness of embedded roots are added to the model during analysis runs. The method of frictional behaviour applies the Coulomb friction model to the root–soil interface to model possible root slippage in the soil medium:

$$\tau_{\mathrm{eq}} = \sqrt{\tau_1^2 + \tau_2^2}$$

$$\tau_{\mathrm{crit}} = \mu p,$$

where τ_1 and τ_2 are two stress components in two perpendicular tangential directions of the friction surface, μ is the friction coefficient and p is normal pressure on the friction surface. The Coulomb friction model states that no relative motion occurs if the equivalent frictional stress τ_{eq} is less than the critical frictional stress τ_{crit} (ABAQUS Theory Guide). In addition, the root and soil surfaces in contact are allowed to separate from each other, but applications to the 3-D anchorage model can lead to either mesh difficulties or convergence problems. In this study, the friction coefficient μ is defined to range from 0·1 to 0·9 for five simulation cases (with different values from the literature ranging from 0·1 to 0·9; data source, Gray and Barker, 2004; Dupuy *et al.*, 2005*a*).

Model of the direct shear test. The geometry of the soil domain is modelled by a rectangular box 0·5 m in length (x) and width (z) and 0·32 m in height (y). For the case of the embedded element, the root segments are embedded in the soil block. The soil area occupied by root segments actually contains both root

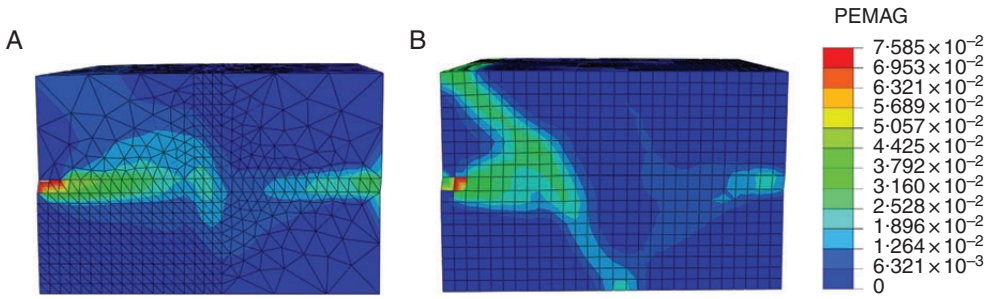

FIG. A1. Comparison of two methods of root-soil interaction modelling: frictional behaviour and embedded element. Distribution of plastic deformation magnitude in the soil medium (A) predicted by the frictional behaviour method and (B) predicted by the embedded element method.

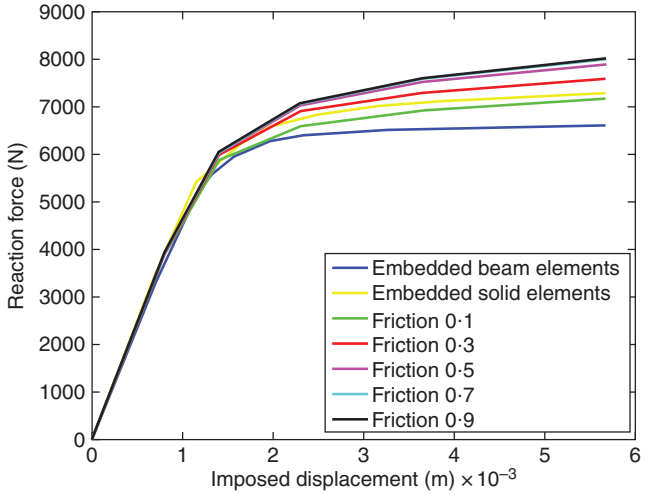

FIG. A2. Comparison of two mesh methods and two root-soil interaction models: force-displacement response curves calculated at the centre of the rigid plate predicted by the embedded beam element method, the embedded solid element method and frictional behaviour method with five friction coefficient values: 0·1, 0·3, 0·5, 0·7 and 0·9.

and soil materials. The entire soil block is meshed into eight-node linear brick elements (C3D8R in the ABAQUS element library) to avoid convergence difficulties. For the case of frictional behaviour, room for roots was provided in the soil. Four-node linear tetrahedron elements (C3D4 in the ABAQUS element library) are chosen to make the soil zone meshable in the vicinity of the root segments. A refined mesh with an average element size of 1·5 cm is defined within the zone surrounding the location of the roots and the soil shear zone. For both cases, the soil material is assumed to be homogeneous and initially linear elastic combined with plastic behaviour defined by the Mohr–Coulomb criterion (the same definition as that from the anchorage model). The soil data set in Table 1 is used in all the simulations.

The soil is reinforced by 12 identical parallel root segments. They are equidistant (4 cm apart) and vertically placed in the plane in the middle of the soil block perpendicular to the direction of the imposed horizontal displacement. The geometry of the root segments is assumed to be a thin cylinder 2 cm in diameter and 28 cm in length. For the case of the embedded element, the root segments are meshed into two-node linear Timoshenko beam elements. For the case of frictional behaviour, the root segments are meshed into C3D8R elements. The root material is assumed to be homogeneous and linear elastic with the same density and modulus of elasticity as that from SA5, namely a density of 421·4 kg m^{-3} and a modulus of elasticity of 8 GPa, as well as a Poisson ratio of 0·3.

A thin plate is defined about half the size of the lateral face (14 × 50 cm^2) of the soil rectangular box to cover the upper half of the lateral face. The plate is meshed into four-node bilinear rigid elements (R3D4 in the ABAQUS element library) and placed against the upper lateral half-face so it is pushed during the shear process. A reference point is defined at the centre of the plate to prescribe its motions (d.o.f.) and record the imposed displacement and pushing force.

Loadings are defined in two analysis steps: the gravity body force is defined in the first step with gravity acceleration $\mathbf{g} = 9{\cdot}81$ m s^{-2} in the downward direction, $-y$. A normal pressure of 1 kPa is applied on the top face of the soil block. The effect of both loadings is propagated through the second analysis step. The bottom of the soil box is fixed with all d.o.f. constrained to 0 through a two-step analysis (ENCASTRE in the ABAQUS Analysis User's Guide). Soil motions with respect to four laterals are constrained to 0 in the first step (XSYMM and YSYMM in the ABAQUS Analysis User's Guide). During the second step, which is the shear process, the same symmetry constraint is defined for the lower half of the lateral face on the opposite side of the pushed lateral face. The constraints on the other lateral planes are removed and a displacement of 2 cm is imposed at the reference point of the rigid plate so that the upper half of the soil block is driven to move horizontally in direction x.

Three root–soil configurations were used in order to make separate comparisons of the geometry effect of using the beam element and the interaction effect of the embedded element: (1) roots meshed into solid elements in frictional contact with the soil medium; (2) roots meshed into solid elements embedded in the soil medium; and (3) roots meshed into beam elements embedded in the soil medium.

Results

The two methods predict similar results in terms of the distribution of plastic strain magnitude in the soil block at the end of the shear process (Fig. 9): two narrow horizontal soil zones with elevated plastic strain magnitude (PEMAG) start at the mid-height of the soil block from both lateral sides (y, z plane) perpendicular to the direction of the imposed displacement. The plastic

zone on the side against the plate stops expanding before arriving at the plane of the 12 root segments and turns obliquely to one side towards the bottom in the middle of the block, and on the other side it turns backwards to the top of the pushing plate. For the case of frictional behaviour, another small soil zone with an elevated plastic strain magnitude can be identified at mid-height in the location of the roots. Since frictional behaviour allows the transmission of normal and shear stresses between the root segments and the soil medium, we can deduce that the root segments make an additional contribution to soil shear, especially in the Mohr–Coulomb failure plane, where they are subjected to larger axial deformations due to soil shearing. The embedded element does not predict such a plastic soil zone at the same location, probably because this interaction approach only consists of the constraint of translational d.o.f. between the root and soil nodes. However, no stress transmission is allowed, which partly limits the additional contribution of the roots to the soil shear process.

Pushing force versus imposed displacement curves are obtained at the reference point on the plate during the analysis runs (Fig. 10). First, we examined the geometry effect of the beam elements by comparing the case of the embedded solid element and the embedded beam element. The curves of the two cases presented good agreement with each other. The initial stiffness of the reinforced soil (the initial slope of the curves) is slightly lower in the case of the beam elements. In addition, the pushing force on the rigid plate after soil yielding predicted by beam elements is smaller by up to 10·2 % at the end of the shear process. Secondly, we examined the effect of the root–soil interaction by comparing the curve of the embedded solid elements to five curves obtained for the frictional behaviour of five friction coefficients, i.e. 0·1, 0·3, 0·5, 0·7 and 0·9. The curve of the embedded solid element is placed exactly between the frictional behaviour curves with friction coefficients of 0·1 and 0·3. Qualitatively, the embedded beam element predicts a curve in good agreement with the curves of frictional behaviour: the initial linear elastic part of the curves has broadly the same slope. Beyond the elastic part the slope decreases gradually, which suggests soil yielding. The largest relative difference in required pushing force between the two interaction methods estimated at the end of shear test is from −1·7 to 9·1 % for all cases of frictional behaviour. For the five cases of frictional behaviour, the global level of reaction force is positively correlated to the friction coefficient. It is reasonable to see that the required pushing force increases with a rougher root–soil interface, which suggests possible stronger stresses transmitted at the interface, making root slippage more difficult. For a friction coefficient $>0{\cdot}5$, the force–displacement curves remain almost the same, which suggests that the root–soil interface is rough enough to be insensitive. Despite the difference between the mechanisms defined by the two approaches, the results predicted by the embedded element method are fairly reasonable and probably equivalent to that of the frictional behaviour of a friction coefficient of 0·2.

Annexe B

Formulation de l'endommagement des racines

B.1 Theoretical framework for root failure properties

The damage model proposed for roots in our model is based on continuum damage mechanics. The continuum damage mechanics, based on the classical continuum mechanics, studies the damage constitutive behaviour of materials in the scale of RVE (Representative Volume Element). Considering the large amount of information required to formulate the theoretical basis, the key elements are only detailed in the form of equations. It reveals the derivation of our damage model – continuum damage mechanics studied in the framework of thermodynamics – shares the same derivation as theories of material plasticity.

— The combination of the first law and the second law of thermodynamics gives rise to the Clausius-Duhem inequality including the term of the Helmholtz free energy (or another alternative is the Gibbs potential).

— The first law and the second law of thermodynamics are given by

$$\int_V \rho \dot{e}\, \mathrm{d}V = \int_V (\sigma : \mathbf{grad}\, \mathbf{v} - \mathrm{div}\, \mathbf{q} + r)\, \mathrm{d}V, \tag{B.1}$$

$$\int_V [\rho \dot{s} + \mathrm{div}\, \frac{\mathbf{q}}{T} - \frac{r}{T}]\, \mathrm{d}V \geq 0. \tag{B.2}$$

— The Helmholtz free energy per unit mass ψ is defined as

$$\psi = e - Ts. \tag{B.3}$$

— The Clausius-Duhem inequality in local form can thus be written with the rate of the Helmholtz free energy and substitution of r by using the first law equation:

$$\sigma : \dot{\varepsilon} - \rho(\dot{\psi} + \dot{T}s) - \mathbf{q}\frac{\mathbf{grad}\,T}{T} \geq 0. \tag{B.4}$$

— The Helmholtz free energy can be divided into three independent variables, which leads to the expression of Clausius-Duhem inequality in terms of plastic, thermal and internal variable components.

— The Helmholtz free energy can be defined as a function of thermal component T, elastic component $\varepsilon^{\mathbf{el}}$ and another component $\mathbf{V_k}$ including the other internal variables (damage variables, material hardening variables, etc., depending on the specific studied process):

$$\psi = \psi(T, \varepsilon^{\mathbf{el}}, \mathbf{V_k}) = e - Ts, \tag{B.5}$$

$$\dot{\psi} = \frac{\partial \psi}{\partial \varepsilon^{\mathbf{el}}} : \dot{\varepsilon}^{\mathbf{el}} + \frac{\partial \psi}{\partial T}\dot{T} + \frac{\partial \psi}{\partial \mathbf{V_k}} : \dot{\mathbf{V}}_{\mathbf{k}}. \tag{B.6}$$

— With the term of the Helmholtz free energy split into three components, the Clausius-Duhem inequality is expressed as follows:

$$(\sigma - \rho\frac{\partial \psi}{\partial \varepsilon^{\mathbf{el}}}) : \dot{\varepsilon}^{\mathbf{el}} + \sigma : \dot{\varepsilon}^{\mathbf{pl}} - \rho(s + \frac{\partial \psi}{\partial T})\dot{T} - \rho\frac{\partial \psi}{\partial \mathbf{V_k}} : \dot{\mathbf{V}}_{\mathbf{k}} - \mathbf{q}\frac{\mathbf{grad}\,T}{T} \geq 0. \tag{B.7}$$

— Supposing elastic deformation in a uniform temperature field:

$$\dot{\varepsilon}^{\mathbf{pl}} = \mathbf{0}, \tag{B.8}$$

$$\dot{\mathbf{V}}_{\mathbf{k}} = \mathbf{0}, \tag{B.9}$$

$$\frac{\mathbf{grad}\,T}{T} = \mathbf{0}, \tag{B.10}$$

$$(\sigma - \rho\frac{\partial \psi}{\partial \varepsilon^{\mathbf{el}}}) : \dot{\varepsilon}^{\mathbf{el}} - \rho(s + \frac{\partial \psi}{\partial T})\dot{T} \geq 0. \tag{B.11}$$

— $\dot{\varepsilon}^{\mathbf{el}}$ and $\dot{T}$ are independent variables and this inequality should be satisfied for any couple of $(\dot{\varepsilon}^{\mathbf{el}}, \dot{T})$, hence we obtain the following constitutive equations:

$$\sigma = \rho \frac{\partial \psi}{\partial \varepsilon^{\mathbf{el}}}, \tag{B.12}$$

$$s = -\frac{\partial \psi}{\partial T}. \tag{B.13}$$

— With the constitutive equations above, the Clausius-Duhem inequality is finally written as

$$\sigma : \dot{\varepsilon}^{\mathbf{pl}} - \rho \frac{\partial \psi}{\partial \mathbf{V_k}} : \dot{\mathbf{V}}_{\mathbf{k}} - \mathbf{q} \frac{\mathbf{grad}\, T}{T} \geq 0. \tag{B.14}$$

— We define hereafter the dissipation based on the expression of the Clausius-Duhem inequality above.

— We define two new variables $\mathbf{A_k}$ and $\mathbf{g}$:

$$\mathbf{A_k} = -\rho \frac{\partial \psi}{\partial \mathbf{V_k}}, \tag{B.15}$$

$$\mathbf{g} = -\mathbf{grad}\, T. \tag{B.16}$$

— Then we define the dissipation per unit volume of the material ϕ as follows:

$$\phi = \sigma : \dot{\varepsilon}^{\mathbf{pl}} + \mathbf{A_k} : \dot{\mathbf{V}}_{\mathbf{k}} + \mathbf{q}\left(\frac{\mathbf{g}}{T}\right) \geq 0. \tag{B.17}$$

— We postulate the existence of a dissipation potential function F, and formulate F in terms of the components of the generalized force vector (or thermodynamic forces) and the associated generalized flux vector (or thermodynamic fluxes).

— We define hereafter the generalized force vector $\mathbf{X}$ and the associated generalized flux vector $\mathbf{J}$ as follows:

$$\mathbf{X} = \{\sigma, \mathbf{A_k}, \mathbf{g}\}, \tag{B.18}$$

$$\mathbf{J} = \{\dot{\varepsilon}^{\mathbf{pl}}, \dot{\mathbf{V}}_{\mathbf{k}}, \mathbf{q}\}. \tag{B.19}$$

— Then the dissipation ϕ is rewritten as follows:

$$\phi = \mathbf{X} \cdot \mathbf{J} \geq 0. \tag{B.20}$$

— We postulate the existence of dissipation potential functions F:

$$F = F(\mathbf{X}; \mathbf{V_k}, T). \tag{B.21}$$

— And all components of the generalized flux vector can be derived by a product of an indeterminate scalar multiplier $\dot{\Lambda}$ and the partial derivative of the dissipation potential function F with respect to the corresponding component of the generalized force vector:

$$\mathbf{X} = \dot{\Lambda}\frac{\partial F}{\partial \mathbf{X}}, \tag{B.22}$$

which is equivalent to:

$$\dot{\varepsilon}^{\mathbf{pl}} = \dot{\Lambda}\frac{\partial F}{\partial \sigma}, \tag{B.23}$$

$$\dot{\mathbf{V}}_{\mathbf{k}} = \dot{\Lambda}\frac{\partial F}{\partial \mathbf{A_k}}, \tag{B.24}$$

$$\mathbf{q} = \dot{\Lambda}\frac{\partial F}{\partial (\frac{\mathbf{g}}{T})}. \tag{B.25}$$

— By determining the evolution in time of the generalized flux vector described above, we acquire the material state at any moment under different loading conditions.

The method described above is called standard thermodynamic approach. It allows only a single scalar dissipation potential function and a single scalar multiplier for all independent variables of the generalized force vector (plastic, thermal process, and other internal variables included in $\mathbf{V_k}$). Therefore it implies the simultaneous evolution of the inelastic and the damage in the material, which is not necessarily the case. Due to this limitation, another alternative which is called quasi-standard thermodynamic approach is often adopted.

— Quasi-standard thermodynamics approach defines a dissipation potential function with the corresponding multiplier that can be split into independent components, for instance, a plasticity component and a component as a function of internal variables in $\mathbf{V_k}$.

— We define first $\mathbf{V_k}$, for instance by selecting a set of scalar damage variable d and $\alpha_{\mathbf{j}}$ including other internal variables ($\alpha_{\mathbf{j}}$ represents the rest of the internal variables in the specific studies process, ranging from strain hardening variables to damage accumulated effect, etc.):

$$\mathbf{V_k} = \mathbf{V_k}(d, \alpha_{\mathbf{j}}). \tag{B.26}$$

— Considering hereafter the isothermal processes for the sake of simplicity, then the Helmholtz free energy at constant T is written as follows:

$$\psi = \psi(\varepsilon^{\mathbf{el}}, \mathbf{V_k}) = \psi(\varepsilon^{el}, d, \alpha_{\mathbf{j}}). \tag{B.27}$$

— The newly introduced thermodynamics associated variables (conjugate generalized force components) are defined as follows:

$$Y = -\rho \frac{\partial \psi}{\partial d}, \tag{B.28}$$

$$\mathbf{A_j} = -\rho \frac{\partial \psi}{\partial \alpha_{\mathbf{j}}}. \tag{B.29}$$

— Focusing only on plastic and damage processes, we define then a dissipation potential function F that can be split into a plastic component f^{pl} and a damage component f^d:

$$F = f^{pl} + f^d. \tag{B.30}$$

— The plastic strain evolution and damage variable evolution are derived as:

$$\dot{\varepsilon}^{\mathbf{pl}} = \dot{\Lambda}^{pl} \frac{\partial f^{pl}}{\partial \sigma}, \tag{B.31}$$

$$\dot{d} = \dot{\Lambda}^{d} \frac{\partial f^{d}}{\partial Y}. \tag{B.32}$$

— The dissipation potentials f^{pl} and f^d can be respectively related to the yield criterion and the failure criterion as below, so the area enclosed by the surfaces $f^{pl} = 0$ and $f^d = 0$ are respectively the elastic region and the undamaged region.

$$f^{pl} \leq 0, \tag{B.33}$$

$$f^d \leq 0. \tag{B.34}$$

In conclusion, the theoretical framework presented above has allowed to explain the derivation of the failure criterion f^d (f defined in our manuscript) and the damage evolution law d (d defined in our manuscript). The point of this theoretical description is: (i) to show the thermodynamic derivation of the two main equations for f and d in our root damage model studied in the next section B.2; (ii) furthermore, to demonstrate that the formulation of damage

and plastic processes share the same derivation. The failure criterion f^d (or eventually the yield criterion f^{pl}) was expressed in the stress space $\{\sigma\}$, but it is common that f^d or f^{pl} is expressed in the strain space $\{\varepsilon\}$.

B.2 Elastic-failure behaviour of roots

Roots are modelled with beam elements. The elastic-failure behaviour of roots is modelled based on the damage model of FMLs (Fiber Metal Laminates) proposed by Linde et al. (2004).

B.2.1 Beam elements

Linear Timoshenko beams in space (B31) with circular sections used in this study are documented in detail in Abaqus Theory Manual and Abaqus Analysis User's Manual. Its formulation is based on the one-dimensional approximation of three-dimensional slender structures. Stresses at each material point of a beam section are determined by

$$\sigma = \mathbf{C} : \varepsilon, \tag{B.35}$$

where $\mathbf{C}$ defines constitutive relations between stresses and strains. The strain tensor ε contains one axial component ε_{11} and two shear components γ_{21}, γ_{31}. Likewise, the stress tensor σ contains one axial component σ_{11} and two shear components τ_{21}, τ_{31}.

B.2.2 Damage model

The part applied to fibres of the damage model proposed by Linde et al. (2004) is adapted for beam elements and root properties. Root materials are initially elastic, during loading the damage state of materials is evaluated by the damage initiation criterion. If the criterion is reached, the degradation of coefficients of the elasticity matrix will be determined by the damage evolution law.
This damage model is applied to a digitized root system using the finite element code ABAQUS® 6.12-1 through a user subroutine UMAT.

Initial elastic properties

Root materials are assumed to be quasi-brittle, initially linear elastic with elastic modulus E defined in the axial direction of the beam and shear modulus G given in two perpendicular directions in each cross-section. The elastic relations of stresses and strains in the beam

cross-section axis are given by

$$\begin{pmatrix} \sigma_{11}^{el} \\ \tau_{21}^{el} \\ \tau_{31}^{el} \end{pmatrix} = \begin{bmatrix} E & 0 & 0 \\ & G & 0 \\ sym & & G \end{bmatrix} \cdot \begin{pmatrix} \varepsilon_{11}^{el} \\ \gamma_{21}^{el} \\ \gamma_{31}^{el} \end{pmatrix}, \tag{B.36}$$

where σ_{11}^{el}, τ_{21}^{el} and τ_{31}^{el} respectively represent the beam's elastic axial stress and two elastic shear stresses along two perpendicular directions 2 and 3 in the cross-section. The matrix is the non-degraded eleasticity matrix $\mathbf{C}$. ε_{11}^{el}, γ_{21}^{el} and γ_{31}^{el} respectively represent the beam's elastic axial strain component and two elastic shear components along two perpendicular directions 2 and 3 in the cross-section.

Damage initiation criterion

The damage initiation criterion is defined in terms of strains and takes into account both tensile and compressive damage responses of the material. The onset of the damage state at a material point is marked by reaching the following criterion

$$f = \sqrt{\frac{\varepsilon_{11}^{t}}{\varepsilon_{11}^{c}}\varepsilon_{11}^{2} + (\varepsilon_{11}^{t} - \frac{{\varepsilon_{11}^{t}}^{2}}{\varepsilon_{11}^{c}})\varepsilon_{11}} > \varepsilon_{11}^{t}, \tag{B.37}$$

where ε_{11} is the axial strain component and

$$\varepsilon_{11}^{t} = \frac{\sigma_{11}^{t}}{E}, \tag{B.38a}$$

$$\varepsilon_{11}^{c} = \frac{\sigma_{11}^{c}}{E}. \tag{B.38b}$$

σ_{11}^{t} and σ_{11}^{c} are respectively tensile strength and compressive strength of the material. Figure B.1 illustrates the damage initiation behaviour using damage properties given in Table B.1.

σ_{11}^{t} (MPa)	σ_{11}^{c} (MPa)	E (MPa)
40	35	1000

Table B.1 Damage initiation parameters

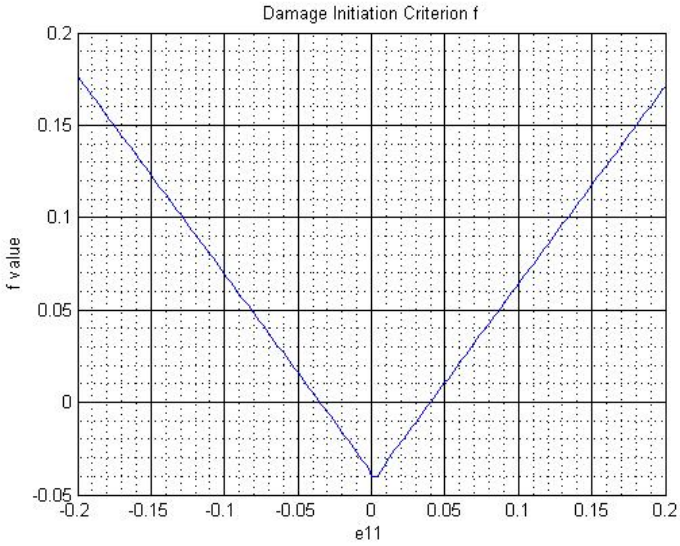

Figure B.1 Damage initiation $f - \varepsilon_{11}^t$ versus ε_{11}

Damage evolution

When the damage initiation criterion is reached, the damage variable d is defined as the damage evolution law by

$$d = 1 - \frac{\varepsilon_{11}^t}{f} \exp\left(\frac{-E\varepsilon_{11}^t (f - \varepsilon_{11}^t) L^c}{G_f}\right), \tag{B.39}$$

where L^c is, in our case, the characteristic length of the beam element. And G_f is the fracture energy. Figure B.2 illustrates the damage evolution behaviour using damage initiation and evolution properties given in Tables B.1 and B.2.

L^c (m)	G_f (J/m^2)
0.2	300

Table B.2 Damage evolution parameters

The damage variable d is intended to define the degradation of the effective elasticity matrix $\mathbf{C_d}$ for each material point

$$[\mathbf{C_d}] = \begin{bmatrix} (1-d)E & 0 & 0 \\ & (1-d)G & 0 \\ sym & & (1-d)G \end{bmatrix}, \tag{B.40}$$

where $G = 0.0755 \cdot E$, according to general mechanical properties of pine wood (USDA-2010).

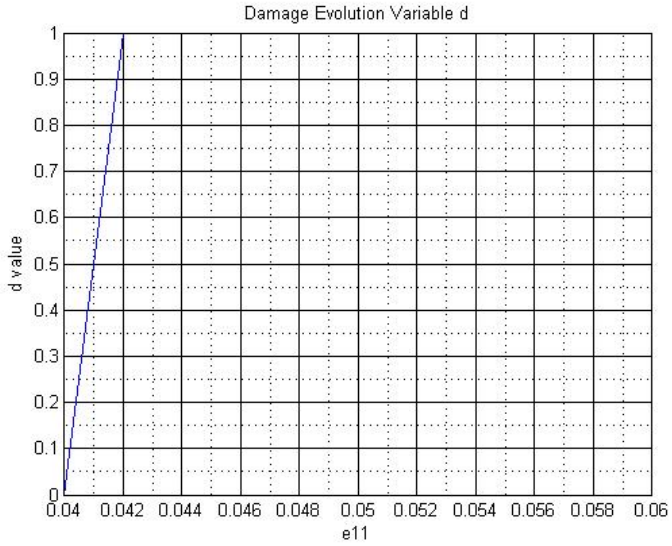

Figure B.2 Damage evolution d versus ε_{11}

Computation of stresses and the Jacobian matrix

Stresses at each material point are then calculated by

$$\sigma = \mathbf{C_d} : \varepsilon. \tag{B.41}$$

The Jacobian matrix is then calculated by

$$\frac{\partial \sigma}{\partial \varepsilon} = \mathbf{C_d} + \frac{\partial \mathbf{C_d}}{\partial \varepsilon} : \varepsilon \tag{B.42a}$$

$$= \mathbf{C_d} + (\frac{\partial \mathbf{C_d}}{\partial d} : \varepsilon)(\frac{\partial d}{\partial f}\frac{\partial f}{\partial \varepsilon}), \tag{B.42b}$$

where

$$\frac{\partial \mathbf{C_d}}{\partial d} = -\mathbf{C}, \tag{B.43a}$$

$$\frac{\partial d}{\partial f} = (\frac{1}{f} + \frac{E\varepsilon_{11}^t L_c}{G_f})\frac{\varepsilon^t}{f}\exp\Big(-\frac{E\varepsilon_{11}^t L^c (f-\varepsilon_{11}^t)}{G_f}\Big), \tag{B.43b}$$

$$\left(\frac{\partial f}{\partial \varepsilon}\right) = \Big(\Big[\frac{\varepsilon_{11}^t}{\varepsilon_{11}^c}\varepsilon_{11} + \frac{1}{2}(\varepsilon_{11}^t - \frac{{\varepsilon_{11}^t}^2}{\varepsilon_{11}^c})\Big]/f \quad 0 \quad 0\Big), \tag{B.43c}$$

where we identify the long expressions in equations B.43b and B.43c as follows:

$$P_1(\varepsilon_{11}) = (\frac{1}{f} + \frac{E\varepsilon_{11}^t L_c}{G_f})\frac{\varepsilon^t}{f}\exp\Big(-\frac{E\varepsilon_{11}^t L^c(f-\varepsilon_{11}^t)}{G_f}\Big), \tag{B.44a}$$

$$P_2(\varepsilon_{11}) = \Big[\frac{\varepsilon_{11}^t}{\varepsilon_{11}^c}\varepsilon_{11} + \frac{1}{2}(\varepsilon_{11}^t - \frac{{\varepsilon_{11}^t}^2}{\varepsilon_{11}^c})\Big]/f, \tag{B.44b}$$

where P_1 and P_2 are two scalar functions of ε_{11}. The degraded Jacobian matrix proves to be asymmetrical through straightforward calculations:

$$\Big[\frac{\partial\sigma}{\partial\varepsilon}\Big] = \begin{bmatrix} (1-d)E - P_1P_2\sigma_{11}^{el} & 0 & 0 \\ -P_1P_2\tau_{21}^{el} & (1-d)G & 0 \\ -P_1P_2\tau_{31}^{el} & 0 & (1-d)G \end{bmatrix}. \tag{B.45}$$

In some cases in which numerical divergence occurs, the damage variable d^v is regularized as follows, instead of being directly calculated by equation B.39:

$$\dot{d^v} = \frac{1}{\eta}(d - d^v), \tag{B.46}$$

where η is the viscosity parameter controlling the rate at which the regularized damage variable d^v approaches the true damage variable d. The modification of damage variable could cause a delay in damage evolution. Therefore to minimize the eventual discrepancy, the value of η is defined to be very small compared to characteristic time increment (load increment in our case of static loading).

Annexe C

Tables de Taguchi

C.1 L54

La matrice orthogonale L54 s'utilise pour l'ensemble des paramètres géométriques de 23 facteurs de contrôle (détaillés dans le Chapitre 4) à trois niveaux pour chacun, à savoir : le niveau de -20%, le niveau de référence et le niveau de +20%.

	Facteurs de contrôle																									
	1	2	3	4	5	6	7	8	9	10	11	12	13	14	15	16	17	18	19	20	21	22	23	24	25	26
Essai 1	-20%	-20%	-20%	-20%	-20%	-20%	-20%	-20%	-20%	-20%	-20%	-20%	-20%	-20%	-20%	-20%	-20%	-20%	-20%	-20%	-20%	-20%	-20%	-20%	-20%	-20%
Essai 2	-20%	-20%	-20%	-20%	-20%	-20%	-20%	-20%	ref	ref	ref	ref	ref	ref	ref	ref	ref	ref	ref	ref	ref	ref	ref	ref	ref	ref
Essai 3	-20%	-20%	-20%	-20%	-20%	-20%	-20%	-20%	+20%	+20%	+20%	+20%	+20%	+20%	+20%	+20%	+20%	+20%	+20%	+20%	+20%	+20%	+20%	+20%	+20%	+20%
Essai 4	-20%	-20%	ref	ref	ref	ref	ref	ref	-20%	-20%	-20%	-20%	-20%	-20%	ref	+20%	ref	+20%	ref	+20%	ref	+20%	ref	+20%	ref	+20%
Essai 5	-20%	-20%	ref	ref	ref	ref	ref	ref	ref	ref	ref	ref	ref	ref	+20%	-20%	+20%	-20%	+20%	-20%	+20%	-20%	+20%	-20%	-20%	-20%
Essai 6	-20%	-20%	ref	ref	ref	ref	ref	ref	+20%	+20%	+20%	+20%	+20%	+20%	-20%	-20%	+20%	-20%	+20%	-20%	+20%	-20%	+20%	-20%	+20%	-20%
Essai 7	-20%	-20%	+20%	+20%	+20%	+20%	+20%	+20%	-20%	-20%	-20%	-20%	-20%	-20%	+20%	+20%	-20%	ref	+20%	ref	-20%	ref	-20%	ref	-20%	ref
Essai 8	-20%	-20%	+20%	+20%	+20%	+20%	+20%	+20%	ref	ref	ref	ref	ref	ref	-20%	+20%	ref	+20%	-20%	+20%	-20%	+20%	-20%	+20%	-20%	+20%
Essai 9	-20%	-20%	+20%	+20%	+20%	+20%	+20%	+20%	+20%	+20%	+20%	+20%	+20%	+20%	ref	-20%	ref	-20%	ref	-20%	ref	-20%	ref	-20%	ref	-20%
Essai 10	-20%	ref	-20%	-20%	ref	ref	+20%	+20%	-20%	ref	+20%	+20%	-20%	+20%	-20%	-20%	-20%	-20%	ref	+20%	-20%	+20%	+20%	+20%	ref	+20%
Essai 11	-20%	ref	-20%	-20%	ref	ref	+20%	+20%	ref	ref	+20%	+20%	-20%	-20%	ref	ref	ref	ref	+20%	-20%	ref	-20%	+20%	-20%	+20%	-20%
Essai 12	-20%	ref	-20%	-20%	ref	ref	+20%	+20%	+20%	+20%	-20%	-20%	ref	ref	+20%	+20%	+20%	+20%	-20%	ref	-20%	ref	ref	-20%	-20%	ref
Essai 13	-20%	ref	ref	ref	ref	+20%	+20%	-20%	-20%	-20%	ref	ref	+20%	+20%	ref	+20%	ref	+20%	+20%	ref	+20%	ref	-20%	-20%	ref	-20%
Essai 14	-20%	ref	ref	ref	ref	+20%	+20%	-20%	-20%	-20%	ref	+20%	-20%	-20%	+20%	-20%	+20%	-20%	-20%	+20%	-20%	+20%	ref	ref	ref	ref
Essai 15	-20%	ref	ref	ref	ref	+20%	+20%	-20%	-20%	-20%	ref	-20%	ref	-20%	-20%	ref	-20%	ref	ref	-20%	ref	-20%	+20%	+20%	+20%	+20%
Essai 16	-20%	ref	+20%	+20%	-20%	-20%	ref	ref	-20%	-20%	ref	ref	+20%	+20%	+20%	ref	+20%	ref	-20%	-20%	-20%	-20%	ref	-20%	+20%	+20%
Essai 17	-20%	ref	+20%	+20%	-20%	-20%	ref	ref	ref	ref	+20%	+20%	-20%	-20%	-20%	+20%	-20%	+20%	ref	-20%	ref	ref	ref	+20%	-20%	-20%
Essai 18	-20%	ref	+20%	+20%	-20%	-20%	ref	ref	+20%	+20%	-20%	-20%	ref	ref	ref	-20%	ref	-20%	+20%	+20%	+20%	+20%	-20%	-20%	ref	-20%
Essai 19	-20%	+20%	-20%	ref	-20%	+20%	ref	+20%	+20%	ref	-20%	+20%	ref	+20%	-20%	-20%	ref	+20%	-20%	-20%	+20%	ref	ref	ref	+20%	+20%
Essai 20	-20%	-20%	-20%	ref	-20%	+20%	ref	+20%	ref	+20%	ref	-20%	+20%	-20%	ref	ref	+20%	-20%	ref	ref	-20%	+20%	+20%	+20%	-20%	+20%
Essai 21	-20%	+20%	ref	ref	-20%	+20%	ref	+20%	+20%	-20%	+20%	ref	-20%	ref	+20%	+20%	-20%	ref	+20%	+20%	ref	-20%	-20%	-20%	ref	-20%
Essai 22	-20%	+20%	ref	+20%	ref	-20%	+20%	-20%	-20%	ref	+20%	ref	+20%	+20%	ref	+20%	+20%	ref	ref	+20%	-20%	-20%	+20%	-20%	ref	-20%
Essai 23	-20%	+20%	ref	+20%	ref	-20%	+20%	-20%	ref	+20%	ref	-20%	+20%	-20%	+20%	-20%	-20%	+20%	+20%	-20%	ref	ref	-20%	+20%	+20%	ref
Essai 24	-20%	+20%	ref	+20%	ref	-20%	+20%	-20%	+20%	-20%	+20%	ref	-20%	ref	-20%	ref	ref	-20%	-20%	ref	+20%	+20%	ref	-20%	-20%	+20%
Essai 25	-20%	+20%	+20%	-20%	+20%	ref	-20%	ref	-20%	ref	-20%	+20%	ref	+20%	+20%	ref	-20%	-20%	+20%	ref	+20%	+20%	-20%	-20%	-20%	+20%
Essai 26	-20%	+20%	+20%	-20%	+20%	ref	-20%	ref	ref	+20%	ref	-20%	+20%	-20%	-20%	+20%	ref	ref	-20%	ref	-20%	-20%	ref	+20%	ref	-20%
Essai 27	-20%	+20%	+20%	-20%	+20%	ref	-20%	ref	+20%	-20%	+20%	ref	-20%	ref	ref	-20%	+20%	+20%	ref	-20%	-20%	-20%	ref	+20%	+20%	ref
Essai 28	ref	-20%	-20%	+20%	+20%	ref	ref	-20%	-20%	+20%	+20%	ref	ref	-20%	-20%	-20%	+20%	ref	+20%	ref	ref	+20%	+20%	ref	+20%	-20%
Essai 29	ref	-20%	-20%	+20%	+20%	ref	ref	-20%	ref	-20%	-20%	+20%	+20%	+20%	ref	ref	-20%	+20%	-20%	+20%	+20%	-20%	+20%	-20%	+20%	ref
Essai 30	ref	-20%	-20%	+20%	+20%	ref	ref	-20%	+20%	ref	ref	-20%	-20%	+20%	+20%	+20%	-20%	-20%	-20%	ref	-20%	-20%	-20%	-20%	ref	+20%
Essai 31	ref	-20%	ref	-20%	-20%	+20%	+20%	ref	-20%	+20%	+20%	ref	ref	-20%	ref	+20%	-20%	-20%	ref	-20%	+20%	ref	+20%	-20%	ref	+20%
Essai 32	ref	-20%	ref	-20%	-20%	+20%	+20%	ref	ref	-20%	-20%	+20%	-20%	+20%	ref	-20%	ref	-20%	ref	ref	-20%	+20%	-20%	+20%	+20%	-20%
Essai 33	ref	-20%	ref	-20%	-20%	+20%	+20%	ref	+20%	ref	ref	-20%	-20%	+20%	-20%	ref	+20%	+20%	+20%	+20%	ref	-20%	ref	-20%	-20%	ref
Essai 34	ref	-20%	+20%	ref	ref	-20%	-20%	+20%	-20%	+20%	+20%	ref	ref	-20%	+20%	ref	ref	+20%	ref	+20%	-20%	-20%	-20%	-20%	+20%	ref
Essai 35	ref	-20%	+20%	ref	ref	-20%	-20%	+20%	+20%	-20%	-20%	+20%	+20%	-20%	-20%	+20%	+20%	-20%	+20%	+20%	-20%	ref	ref	ref	-20%	+20%
Essai 36	ref	-20%	+20%	ref	ref	-20%	-20%	+20%	+20%	ref	ref	-20%	-20%	+20%	ref	-20%	-20%	ref	-20%	ref	+20%	+20%	+20%	+20%	+20%	-20%
Essai 37	ref	ref	-20%	ref	+20%	-20%	+20%	ref	-20%	ref	+20%	-20%	+20%	ref	-20%	-20%	ref	+20%	+20%	ref	-20%	-20%	-20%	+20%	ref	+20%
Essai 38	ref	ref	-20%	ref	+20%	-20%	+20%	ref	ref	+20%	-20%	ref	-20%	+20%	ref	ref	+20%	-20%	-20%	+20%	ref	ref	-20%	+20%	+20%	-20%
Essai 39	ref	ref	-20%	ref	+20%	-20%	+20%	ref	+20%	-20%	ref	+20%	ref	-20%	+20%	+20%	-20%	ref	ref	-20%	+20%	+20%	-20%	-20%	-20%	ref
Essai 40	ref	ref	ref	+20%	-20%	ref	-20%	+20%	-20%	ref	+20%	-20%	+20%	ref	ref	+20%	+20%	ref	-20%	-20%	-20%	ref	+20%	-20%	+20%	ref
Essai 41	ref	ref	ref	+20%	-20%	ref	-20%	+20%	ref	+20%	-20%	ref	-20%	+20%	+20%	-20%	-20%	+20%	ref	ref	+20%	ref	-20%	ref	-20%	+20%
Essai 42	ref	ref	ref	+20%	-20%	ref	-20%	+20%	+20%	-20%	ref	+20%	ref	-20%	-20%	ref	ref	-20%	+20%	+20%	-20%	ref	+20%	+20%	ref	-20%
Essai 43	ref	ref	+20%	-20%	ref	+20%	ref	-20%	-20%	ref	+20%	-20%	+20%	ref	+20%	ref	-20%	-20%	ref	+20%	+20%	ref	ref	+20%	+20%	-20%
Essai 44	ref	ref	+20%	-20%	ref	+20%	ref	-20%	ref	+20%	-20%	ref	-20%	+20%	-20%	+20%	ref	ref	+20%	-20%	-20%	+20%	+20%	-20%	-20%	ref
Essai 45	ref	ref	+20%	-20%	ref	+20%	ref	-20%	+20%	-20%	ref	+20%	ref	-20%	ref	-20%	+20%	+20%	-20%	ref	-20%	-20%	ref	-20%	ref	+20%
Essai 46	ref	+20%	-20%	+20%	ref	+20%	-20%	ref	-20%	+20%	ref	+20%	-20%	-20%	-20%	-20%	+20%	ref	ref	+20%	+20%	-20%	-20%	-20%	-20%	+20%
Essai 47	ref	+20%	-20%	+20%	ref	+20%	-20%	ref	ref	-20%	+20%	-20%	ref	+20%	ref	-20%	-20%	+20%	+20%	-20%	-20%	+20%	ref	-20%	ref	-20%
Essai 48	ref	+20%	-20%	+20%	ref	+20%	-20%	ref	+20%	ref	-20%	ref	+20%	-20%	+20%	+20%	ref	-20%	-20%	ref	ref	-20%	+20%	+20%	-20%	ref
Essai 49	ref	+20%	ref	-20%	+20%	-20%	ref	+20%	-20%	+20%	+20%	-20%	-20%	+20%	ref	+20%	-20%	-20%	+20%	+20%	-20%	-20%	ref	+20%	+20%	ref
Essai 50	ref	+20%	ref	-20%	+20%	-20%	ref	+20%	ref	-20%	+20%	-20%	ref	+20%	+20%	-20%	ref	ref	+20%	ref	-20%	ref	+20%	-20%	-20%	+20%
Essai 51	ref	+20%	ref	-20%	+20%	-20%	ref	+20%	+20%	ref	-20%	ref	+20%	-20%	-20%	ref	+20%	+20%	ref	-20%	+20%	+20%	-20%	ref	ref	-20%
Essai 52	ref	+20%	+20%	ref	-20%	ref	+20%	-20%	-20%	+20%	ref	+20%	-20%	ref	+20%	ref	ref	+20%	-20%	-20%	ref	+20%	+20%	-20%	ref	-20%
Essai 53	ref	+20%	+20%	ref	-20%	ref	+20%	-20%	ref	-20%	+20%	-20%	ref	+20%	-20%	+20%	+20%	-20%	ref	ref	+20%	-20%	-20%	+20%	ref	ref
Essai 54	ref	+20%	+20%	ref	-20%	ref	+20%	-20%	+20%	ref	-20%	ref	+20%	-20%	ref	-20%	-20%	ref	+20%	+20%	-20%	ref	ref	-20%	+20%	+20%

C.2 L27

La matrice orthogonale L27 s'utilise pour l'ensemble des paramètres matériaux de 11 facteurs de contrôle (détaillés dans le Chapitre 4) à trois niveaux pour chacun, à savoir : le niveau de -20%, le niveau de référence et le niveau de +20%.

	Facteurs de contrôle												
	1	2	3	4	5	6	7	8	9	10	11	12	13
Éssai 1	-20%	-20%	-20%	-20%	-20%	-20%	-20%	-20%	-20%	-20%	-20%	-20%	-20%
Éssai 2	-20%	-20%	-20%	-20%	ref	ref	ref	ref	ref	ref	ref	ref	ref
Éssai 3	-20%	-20%	-20%	-20%	+20%	+20%	+20%	+20%	+20%	+20%	+20%	+20%	+20%
Éssai 4	-20%	ref	ref	ref	-20%	-20%	-20%	ref	ref	ref	+20%	+20%	+20%
Éssai 5	-20%	ref	ref	ref	ref	ref	ref	+20%	+20%	+20%	-20%	-20%	-20%
Éssai 6	-20%	ref	ref	ref	+20%	+20%	+20%	-20%	-20%	-20%	ref	ref	ref
Éssai 7	-20%	+20%	+20%	+20%	-20%	-20%	-20%	+20%	+20%	+20%	ref	ref	ref
Éssai 8	-20%	+20%	+20%	+20%	ref	ref	ref	-20%	-20%	-20%	+20%	+20%	+20%
Éssai 9	-20%	+20%	+20%	+20%	+20%	+20%	+20%	ref	ref	ref	-20%	-20%	-20%
Éssai 10	ref	-20%	ref	+20%	-20%	ref	+20%	-20%	ref	+20%	-20%	ref	+20%
Éssai 11	ref	-20%	ref	+20%	ref	+20%	-20%	ref	+20%	-20%	ref	+20%	-20%
Éssai 12	ref	-20%	ref	+20%	+20%	-20%	ref	+20%	-20%	ref	+20%	-20%	ref
Éssai 13	ref	ref	+20%	-20%	-20%	ref	+20%	ref	+20%	-20%	+20%	-20%	ref
Éssai 14	ref	ref	+20%	-20%	ref	+20%	-20%	+20%	-20%	ref	-20%	ref	+20%
Éssai 15	ref	ref	+20%	-20%	+20%	-20%	ref	-20%	ref	+20%	ref	+20%	-20%
Éssai 16	ref	+20%	-20%	ref	-20%	ref	+20%	+20%	-20%	ref	ref	+20%	-20%
Éssai 17	ref	+20%	-20%	ref	ref	+20%	-20%	-20%	ref	+20%	+20%	-20%	ref
Éssai 18	ref	+20%	-20%	ref	+20%	-20%	ref	ref	+20%	-20%	-20%	ref	+20%
Éssai 19	+20%	-20%	+20%	ref	-20%	+20%	ref	-20%	+20%	ref	-20%	+20%	ref
Éssai 20	+20%	-20%	+20%	ref	ref	-20%	+20%	ref	-20%	+20%	ref	-20%	+20%
Éssai 21	+20%	-20%	+20%	ref	+20%	ref	-20%	+20%	ref	-20%	+20%	ref	-20%
Éssai 22	+20%	ref	-20%	+20%	-20%	+20%	ref	ref	-20%	+20%	+20%	ref	-20%
Éssai 23	+20%	ref	-20%	+20%	ref	-20%	+20%	+20%	ref	-20%	-20%	+20%	ref
Éssai 24	+20%	ref	-20%	+20%	+20%	ref	-20%	-20%	+20%	ref	ref	-20%	+20%
Éssai 25	+20%	+20%	ref	-20%	-20%	+20%	ref	+20%	ref	-20%	ref	-20%	+20%
Éssai 26	+20%	+20%	ref	-20%	ref	-20%	+20%	-20%	+20%	ref	+20%	ref	-20%
Éssai 27	+20%	+20%	ref	-20%	+20%	ref	-20%	ref	-20%	+20%	-20%	+20%	ref

Table des figures

Liste des tableaux